Solving the Inverse Problem for Localising the Biomagnetic Activity in the Heart

Dissertation

zur Erlangung des akademischen Grades
Doktor der Ingenieurwissenschaften
(Dr.-Ing.)
der Technischen Fakultät
der Christian-Albrechts-Universität zu Kiel

vorgelegt von

Nawar Habboush
aus Bagdad

Kiel 2024

Berichterstatter: Prof. Dr.-Ing. Gerhard Schmidt
Prof. Dr.med. Ulrich Stephani

Datum der mündlichen Prüfung: 05.08.2024

Acknowledgement

I would like to express my sincere gratitude to Prof. Dr. Gerhard Schmidt, who guided, supported and motivated me throughout this project. He has been a great mentor and an inspiration for me, not only during my PhD but since I joined CAU Kiel for my masters degree. I also thank Prof. Dr. Michael Siniatchkin for his generous support and his visionary ideas for this project to apply the Kalman filter to the human heart data. I am thankful to Prof. Dr. Ulrich Stephani for his assistance and enthusiasm in finalising my dissertation. I acknowledge the contribution of Dr. Andreas Galka for initiating the Kalman filter research in our group, and his helpful suggestions for improving and extending the Kalman filter further. I thank Dr. Laith Hamid for his comprehensive knowledge and information on the literature that was a valuable resource for me.

I appreciate the collaboration of Dr. Tilmann Sander-Thömmes for his involvement and assistance in the MCG and ECG recording in PTB Berlin. I thank Dr. Alexander Hunold for his help in the forward modelling and using SimBio. I thank Dr. Thomas Demming for his insightful feedback and validation on the heart analyses results. I would like to thank Stephan Wolff for helping me obtain MRI recordings from our volunteering individuals, I would like to thank Dr. Andreas Galka and Seedo Paul for volunteering besides me to get ECG and MCG datasets in PTB Berlin and MRI data at the UKSH in Kiel.

I thank all the members and students in the PedBi work group, especially Dr. Vera Moliadze and Dr. Navah Kadish for creating the best working environment and supporting me in various scientific and administrative matters. I thank Prof. Dr. Frauke Nees and Monika Hoffmann for their support in the IMPS in Kiel.

My heartfelt gratitude goes to my parents, who have steadfastly supported me emotionally, financially, and in every decision I have made, even amidst the trials of wars and hardships.

I acknowledge the financial support of the German Research Foundation (DFG) through the projects PAK902, and SFB1261.

Kurzzusammenfassung

Diese Dissertation zielt darauf ab, eine umfassende Lösung sowohl für Vorwärts- als auch für inverse Probleme bei der Modellierung des menschlichen Herzens zu entwickeln, wobei der Schwerpunkt auf der genauen Analyse von MKG- und EKG-Datensätzen liegt. Die Forschungsmethodik umfasst einen sorgfältigen Prozess der Datenaufzeichnung, MRT-Verarbeitung und Konstruktion eines multiregionalen Modells, das verschiedene Gewebe aufgrund ihrer relevanten Eigenschaften segmentiert und letztendlich eine Lösung für das Vorwärtsproblem bietet. Der vorgeschlagene Ansatz nutzt den Kalman-Filter und Zustandsraummodelle, gefolgt vom GARCH-Modell, um das Inverse Problem zu lösen, was zu einer verbesserten Genauigkeit der Datenanalyse und Quellenlokalisation führt.

Diese Dissertation markiert den ersten Versuch, die Kalman-Filter-Methodik anzuwenden, um MKG-Daten zu analysieren, basierend auf umfangreicher Erfahrung, die im Gehirnforschungsbereich, insbesondere für EEG- und MEG-Datensätze, gesammelt wurde. Der vorgeschlagene Ansatz wurde an simulierten und realen MKG- und EKG-Datensätzen von Individuen getestet und validiert und zeigt seine Wirksamkeit bei der Analyse von Herzaktivitätsdaten und sein immenses Potenzial für klinische Anwendungen.

Die Bedeutung dieser Forschung liegt in ihren potenziellen Auswirkungen auf die Diagnose und Behandlung verschiedener Herzkrankheiten. Die entwickelte Methodik kann Quellen der Herzaktivität präzise lokalisieren, was bei der Diagnose und Interventionsplanung, wie z.B. Ablation oder Schrittmacherimplantation, hilfreich sein kann. Die nicht-invasive Methode zur Aktivitätslokalisation unter Verwendung von MKG- und EKG-Datensätzen im Vergleich zur invasiven Methode mittels Katheter eröffnet neue Möglichkeiten für die Diagnose und Behandlung von Herzkrankheiten.

Während einfachere Methoden für inverse Probleme, die keine hohe Rechenleistung erfordern, verwendet werden können, um die Quellaktivität sowohl von MKG-SQUID- als auch EKG-Elektroden-Datensätzen zu finden, zielt diese Dissertation auch darauf ab, Datenanalyse für Sensoren mit einem geringeren Signal-Rausch-Verhältnis wie den in Kiel entwickelten magnetoelektrischen Sensoren bereitzustellen. Die Verwendung solcher Sensoren ist kostengünstiger in Bezug auf die anfänglichen Gerätekosten und laufenden Kosten.

Diese interdisziplinäre Forschung präsentiert eine neue Methodik zur Analyse von MKG- und EKG-Datensätzen, die das Potenzial hat, das Feld der medizinischen Wissenschaften zu revolutionieren, insbesondere die Diagnose von Herzkrankheiten. Das immense Potenzial dieser Forschung unterstreicht die bedeutenden Beiträge, die interdisziplinäre Forschung mit Ingenieurwissenschaften zur Förderung der medizinischen Wissenschaften leisten kann.

Abstract

This thesis aims to develop a comprehensive solution for both forward and inverse problems in modelling the human heart, with a specific focus on accurately analysing MCG and ECG datasets. The research methodology involves a meticulous process of data recording, MRI processing, and constructing a multi-regional model that segments different tissues based on their relevant characteristics, ultimately providing a solution for the forward problem. The proposed approach employs the use of Kalman filter and state-space models, followed by the GARCH model to solve the inverse problem, resulting in improved accuracy of data analysis and source localization.

This thesis marks the first attempt to apply the Kalman filtering methodology to analyse MCG data, drawing from extensive experience gained in brain research, particularly for EEG and MEG datasets. The proposed approach has been tested and validated using both simulated and real MCG and ECG datasets from individuals, demonstrating its efficacy in analysing heart activity data and its immense potential for clinical applications.

The significance of this research lies in its potential implications for the diagnosis and treatment of various heart conditions. The developed methodology can precisely localize sources of heart activity, aiding in diagnosis and intervention planning, such as ablation or pacemaker implantation. The non-invasive method of activity localization using MCG and ECG datasets, as compared to the invasive method of using a catheter, opens up new avenues for the diagnosis and treatment of heart conditions.

While simpler inverse problem methods that do not require high computational power can be used to find the source activity of both MCG SQUID and ECG electrodes datasets, this thesis also aims to provide data analysis for sensors with a lower signal to noise ratio like the magnetoelectric sensor being developed in Kiel. The usage of such sensors is cheaper in terms of initial device costs and running costs.

This interdisciplinary research presents a novel methodology for analysing MCG and ECG datasets that has the potential to revolutionize the field of medical science, specifically the diagnosis of heart conditions. The immense potential of this research highlights the significant contributions that interdisciplinary research with engineering can make towards advancing medical science.

Contents

List of Figures

List of Tables

Glossary

ABIC	Akaike Bayesian Information Criterion
AIC	Akaike Information Criterion
AR2	Autoregressive Model of Order Two
AV	Atrioventricular
BEM	Boundary Element Model
BFGS	Broyden-Fletcher-Goldfarb-Shanno
BMSR-2	Berlin Magnetically Shielded Room 2
CG-FEM	Continuous Galerkin Finite Element Method
CRC	Collaborative Research Centre
CT	Computed Tomography
DSM	Distributed Source Method
ECD	Equivalent Current Dipole
ECG	Electroencephalography
EEG	Electroencephalography
FEM	Finite Element Method
GARCH	Generalized Autoregressive Conditional Heteroskedasticity
GUI	Graphical User Interface
KF	Kalman Filter
LFM	Leadfield Matrix
LORETA	Low Resolution Electromagnetic Tomography
MCG	Magnetocardiography
ME	Magnetoelectric
ML	Maximum Likelihood
MNE	Minimum Norm Estimation
MRI	Magnetic Resonance Imaging
PTB	Physikalisch - Technische Bundesanstalt
SA	Sinoatrial
SCD	Sudden Cardiac Death
SQUID	Superconducting Quantum Interference Device
ss	State-space
ssGARCH	state-space generalized autoregressive conditional heteroskedasticity

ssGARCH-STKF	state-space generalized autoregressive conditional heteroskedasticity Spatiotemporal Kalman Filter
STKF	Spatiotemporal Kalman Filter
SVD	Singular Value Decomposition

Notation

x	Scalars quantities are written as non-bold letters
$\vec{\boldsymbol{x}}$	Vectors are written as lower-case, bold letters with a vector sign. Includes multichannel vectors
$\underline{\boldsymbol{X}}$	Matrices are written as upper-case, bold letters with underline

List of Mathematical Operations

$\mathcal{L}^{(II)}(\theta)$	Type-II log-likelihood
$\otimes$	Kronecker product
$^\top$	Transpose of a vector or a matrix

List of Latin Symbols

$\vec{\boldsymbol{j}}_{t\|t-1}$	State prediction at time point t
$\vec{\vec{\boldsymbol{j}}}_{v,t-1}$	Local current density vector at voxel v and time point $t-1$ for the STKF
$\vec{\vec{\boldsymbol{j}}}_{v,t}$	Local current density vector at voxel v and time point t for the STKF
$\vec{\vec{\boldsymbol{j}}}_{v,t-1\|t-1}$	Local state estimation at voxel v and time point $t-1$ for the STKF
$\vec{\vec{\boldsymbol{j}}}_{v,t\|t-1}$	Local state prediction at voxel v and time point t for the STKF
$\vec{\vec{\boldsymbol{j}}}_{v,t\|t}$	Local state estimation at voxel v and time point t for the STKF
N_{LOR}	The number of hyperparameters to be optimised using Akaike information criterion methods
N_j	Number of current dipoles
N_{st}	Dimension of the local state vector of the STKF
N_v	Number of grid points in the source space
N_y	Number of measurement channels
T_s	Number of time points in the segment between the T-point and the next P-point of the PQRST heartbeat complex
$\underline{\boldsymbol{A}}$	State transition matrix
$\underline{\boldsymbol{A}}_L$	Local state transition matrix of the STKF
$\underline{\boldsymbol{B}}$	Input matrix
$\underline{\boldsymbol{B}}_L$	Local input matrix of the STKF
$\underline{\boldsymbol{G}}_t$	Kalman gain matrix
$\underline{\boldsymbol{G}}_{v,t}$	Local Kalman gain matrix at voxel v and time point t for the STKF
$\underline{\boldsymbol{I}}_N$	$N \times N$-dimensional identity matrix

$\underline{\boldsymbol{K}}$	Lead field matrix
$\underline{\boldsymbol{L}}$	Laplacian matrix
$\underline{\boldsymbol{Y}}$	Multiple channels MCG matrix with $N_y \times N_t$
$\mathcal{L}$	Log-likelihood
$\overline{y}_i$	The i_{th} scalar component of $\vec{\overline{\boldsymbol{y}}}$
$\underline{\tilde{\boldsymbol{A}}}$	Laplacianised state transition matrix
$\underline{\tilde{\boldsymbol{B}}}$	Laplacianised input matrix
$\underline{\tilde{\boldsymbol{K}}}$	The lead field matrix multiplied by the inverse of the Laplacian matrix
$\vec{\mathbf{1}}_N$	Vector of ones with the length of N
$\vec{\boldsymbol{j}}$	Current density vector
$\vec{\boldsymbol{j}}_{t\|t}$	State estimation at time point t
$\vec{\boldsymbol{m}}$	Average vector of MCG over silent time period
$\vec{\boldsymbol{r}}_{\vec{\boldsymbol{j}}_t}$	State prediction error
$\overline{\vec{\tilde{\boldsymbol{j}}}}_{v,t-1}$	The prediction of the local current density vector at voxel v and time point t for the STKF
$\overline{\vec{\tilde{\boldsymbol{j}}}}_{v,t}$	The prediction of the local current density vector at voxel v and time point $t+1$ for the STKF
$\vec{\tilde{\boldsymbol{j}}}$	Laplacianized current density vector
a_1	First autoregressive parameter of the voxels self-dynamics
a_2	Second autoregressive parameter of the voxels self-dynamics
b	First autoregressive parameter of the neighbours' contribution to the voxels dynamics
d	The distance between neighbouring points in the heart source grid
n	The number of the real neighbouring source grid points
p	The order of autoregressive model
s	Starting time point of silent period at T-point of the PQRST heartbeat complex
s_i	The i_{th} singular value
t	Current time instant
$t+1$	Next time instant
$t-1$	Previous time instant
v	Source point in the heart source space
$\vec{\boldsymbol{r}}_{\tilde{j}v,t}$	Local state prediction error at voxel v and time point t for the STKF
$\vec{\boldsymbol{r}}_{\vec{\boldsymbol{y}}t}$	Measurement prediction error or innovations

List of Greek Symbols

$\underline{\boldsymbol{\Sigma}}_{\vec{\boldsymbol{r}}_{y,t}}$	Innovation covariance matrix
$\underline{\boldsymbol{\Sigma}}_{\vec{\boldsymbol{j}}_{t\|t-1}}$	State prediction error covariance matrix at time point t
$\underline{\boldsymbol{\Omega}}$	The matrix of neighbourhood among voxels
$\underline{\boldsymbol{\Sigma}}_{\vec{\boldsymbol{\epsilon}}}$	Measurement noise covariance matrix

λ	Regularization parameter
ρ	Magnitude of the oscillation generated by the AR(2) parameters
σ_{ϵ}^{2}	Measurement noise variance
$\vec{\boldsymbol{\epsilon}}$	Measurement noise vector
$\vec{\boldsymbol{\eta}}$	Dynamical noise vector
$\vec{\tilde{\boldsymbol{\eta}}}$	Laplacianised dynamical noise vector
$\underline{\underline{\boldsymbol{\Sigma}}}_{\tilde{\jmath}_{v,t-1\|t-1}}$	Local state estimation error covariance matrix at voxel v and time point $t-1$ for the STKF
$\underline{\underline{\boldsymbol{\Sigma}}}_{\tilde{\jmath}_{v,t\|t-1}}$	Local state prediction error covariance matrix at voxel v and time point t for the STKF
$\underline{\underline{\boldsymbol{\Sigma}}}_{\tilde{\jmath}_{v,t\|t}}$	Local state estimation error covariance matrix at voxel v and time point t for the STKF
$\underline{\underline{\boldsymbol{\Sigma}}}_{\vec{\boldsymbol{\jmath}}_{t-1\|t-1}}$	State estimation error covariance matrix at time point $t-1$
$\underline{\underline{\boldsymbol{\Sigma}}}_{\vec{\boldsymbol{\jmath}}_{t\|t}}$	State estimation error covariance matrix at time point t
$\underline{\underline{\boldsymbol{\Sigma}}}_{\vec{\boldsymbol{\eta}}}$	Dynamical noise covariance matrix
$\underline{\underline{\boldsymbol{\Sigma}}}_{\vec{\tilde{\boldsymbol{\eta}}}}$	Laplacianised dynamical noise covariance matrix
$\underline{\underline{\boldsymbol{\Sigma}}}_{\vec{\tilde{\boldsymbol{\eta}}}_L}$	Local dynamical noise covariance matrix of the STKF

Chapter 1

Introduction

1.1 Motivation and Potential Applications

Arrhythmia, a condition that disrupts the normal rhythm of the heart, is a leading cause of sudden cardiac death (SCD), claiming the lives of over 300,000 individuals in the USA and 70,000 in the UK annually. The grim reality is that the survival rate is a mere 2%, underscoring the urgent need for effective treatment options.

Despite its profound impact on society and the significant burden it places on health systems, arrhythmia remains a difficult condition to treat, with limited therapeutic possibilities. Moreover, our understanding of the underlying causes and cellular mechanics of arrhythmia is still incomplete, hindering progress in the development of effective treatments.

Even autopsy, the gold standard for identifying the cause of death, fails to provide answers in 40% of recorded cases. These statistics highlight the urgent need for further research and innovation to improve our understanding of arrhythmia and its complexities.

The causes of arrhythmia are diverse and sometimes unknown. The primary cause may be a delay, blockage, or re-entry in the nerve cell pathways that generate and transmit the electrical signal controlling heartbeats. Another cause could be changes to the heart's anatomy due to a mutation or damage to the heart tissues caused by a decrease in blood flow, scarring, or fibrosis. Strong emotions such as anxiety, sudden surprise, or anything that increases blood pressure could also trigger arrhythmia [MMH12].

One method of treatment for arrhythmia is catheter ablation, which is used in certain cases to burn or freeze the malfunctioning tissues and turn them into non-conducting scars. The localisation of the electrical pathways in the heart is important for this procedure. Currently, clinics use invasive catheters that pass through the heart vessels to localise heart activity, but this method has several side effects. We aim to localise the heart's electrical activity non-invasively by detecting activity using Magnetocardiography (MCG) or Electrocardiography (ECG) [IMZ12].

MCG and ECG are non-invasive methods of measuring cardiac activity. They record the magnetic or electric fields generated by the heart's muscle contractions around the torso. MCG is a contactless technique that uses Superconducting Quantum Interference Devices

(SQUIDs), while ECG employs electrodes. Both methods sample at a high rate, usually around 1000 Hz. The heart's electromagnetic waves originate from two trigger points, causing a series of chemical reactions that result in the polarisation and depolarisation of ion channels. Ultimately, this leads to muscle contractions, and the heart pumps blood to the lungs and body for oxygen exchange.

This electrical activity of the cardiac cycle generates an electromagnetic wave that can be detected by MCG or ECG. ECG is an inexpensive and flexible method to use around the body, while MCG is relatively expensive. The SQUID sensors used in MCG require super cooling with helium, a shielded room, and are inflexible in terms of distribution around the body. However, there are cheaper alternatives to SQUID sensors for MCG known as magnetoelectric (ME) sensors, which were developed in Kiel within the Collaborative Research Centre (CRC) 1261, that has funded this thesis work. The new ME sensors are cheaper to operate because they do not require super cooling and are relatively flexible in distribution around the body, but are still under development and have low sensitivity. Additionally, MCG has an advantage over ECG in that the magnetic field is not attenuated through the body tissue.

To estimate the location of heart activity using MCG or ECG, we need to solve the inverse problem. The first step involves solving the forward problem and establishing a relationship between the source points representing the heart and the sensor points representing the MCG or ECG sensor array. Magnetic Resonance Imaging (MRI) is used to create 3-dimensional images of the torso, which are segmented into layers representing different organs. Each voxel in the layer has a conductivity value relative to the layer. A voxel is a three-dimensional equivalent of a pixel that represents a value on a regular grid in 3D space. This term is commonly used in computer graphics, medical imaging, and other areas that involve representing and processing 3D data.

We use this model to calculate the Leadfield Matrix (LFM), which represents the relationship between the sensors and source points. LFM is calculated by simulating unit vectors in every source voxel and determining the transmission of this dipole through the torso tissues to the sensors using Maxwell's equations and Biot–Savart law.

We can use the LFM to solve the inverse problem and estimate the locations, strength, and orientation of the electrical cardiac activity solely from the non-invasive MCG and ECG recordings. However, since the number of sensors is fewer than the number of source points, we cannot solve the inverse problem by simply multiplying by the inverse of the LFM. There are several methods to solve the inverse problem, which can be categorized into three types: dipole fit, beamformers, and distributed sources. The distributed sources methods can be further classified into two types: static and dynamic, based on whether they consider the temporal dynamics of the data.

1.2 Spatiotemporal Kalman Filter Applications in the Medical Field

Our research group has invested considerable time and effort in implementing and refining the STKF, primarily for the analysis of Electroencephalography (EEG) data related to the brain. The initial implementation was published in 2004 [Gal+04], where the temporal dynamics of the EEG were reconstructed in each voxel of the grey matter in the brain using an autoregressive model with spatial smoothness. The clinical EEG analysis showed that the STKF, with its ability to choose a suitable dynamical model, offered significant improvement over the static inverse problem methods.

In an effort to further improve the model, an extended study was conducted using the state-space Generalized Autoregressive Conditional Heteroskedasticity (ssGARCH) model with the STKF. This model is more advanced than the autoregressive model and widely recognized in the field of econometrics [GYO04]. The ssGARCH model was used in 2006 to model the non-stationarity in EEG [Won+06].

The primary objective of this research is to establish a robust pipeline for effectively solving the forward and inverse problems associated with the heart, using the Spatiotemporal Kalman Filter (STKF) approach. The approach of leveraging the knowledge and development of the STKF application from the brain domain to the heart domain forms a crucial aspect of this study.

1.3 Spatiotemporal Kalman Filter for the Heart Research

We utilized the Spatiotemporal Kalman Filter (STKF) with state-space (SS) autoregressive and Generalized Autoregressive Conditional Heteroskedasticity (GARCH) models to estimate the locations, strength, and orientation of the electrical cardiac activity from the non-invasive MCG and ECG recordings. In order to evaluate the effectiveness of our method, we compared it with Low Resolution Electromagnetic Tomography (LORETA), which is a standardized method that considers spatial smoothness like the STKF. However, the STKF goes further by incorporating temporal smoothness as well. By comparing the results of these two methods, we were able to assess the improvement of the STKF and the state-space modelling by incorporating temporal smoothness, as described in [Gre+08].

The spatiotemporal Kalman filter (STKF) is a powerful tool for solving inverse problems in a variety of applications, including the brain and the heart functions. It has multiple advantages and strengths, including its ability to incorporate both spatial and temporal information, handle missing data for a sensor location or missing time point, and use a mathematical model such as the state-space (ss) and generalized autoregressive conditional heteroscedasticity (GARCH) that accurately represents the system being analysed.

The STKF also accounts for uncertainty by calculating covariance matrices that represent the uncertainty in the predictions and observations. This allows the filter to give more weight to more reliable data and less weight to less reliable data, leading to accurate estimates of the system state.

One significant drawback of the STKF is that it requires a considerable amount of computational power, especially when estimating the model parameters. As a result, it may not be suitable for real-time applications. However, rapid advancements in computing technology, including the emerging field of quantum computing, offer promising opportunities to overcome this limitation. Additionally, signal processing techniques such as Laplacian and approximation assumptions can also contribute to enhancing the performance of the STKF. These advancements and techniques hold great potential for expanding the applicability of the STKF in the future.

Despite its computational requirements, we expect the STKF to outperform other inverse problem solvers in accuracy and reliability. Through this thesis, we will compare the STKF with other inverse problem solvers that have theoretical similarities to see and quantify the improvement of the STKF. Overall, the STKF's strengths and potential for improvement make it a valuable tool for solving complex inverse problems in various systems, including the brain and the heart.

As stated earlier, the main objective of this thesis is to perform source estimation for the CRC 1261, which is developing a novel type of magnetic field sensor. Despite the fact that the ME sensor has limited sensitivity for the inverse problem, we established a pipeline that takes into account various factors to achieve accurate source estimation with low-sensitive sensors. We acquired MCG and ECG data at the Berlin Magnetically Shielded Room 2 (BMSR-2) located at the Physikalisch - Technische Bundesanstalt (PTB) in Berlin. To improve the accuracy of source localisation, we obtained individual MRI scans instead of using a generic model to segment the torso into multiple layers based on the conductivities of the organs and tissues. We utilized the segmented torso model to construct a realistic Finite Element Method (FEM), which is a more complex but more detailed model than the Boundary Element Method (BEM). In FEM, each voxel can have a distinct conductivity based on the type of tissue or organ it represents.

1.4 Contents of the Thesis

Chapter 2 provides a theoretical background on the medical and technical concepts employed in this thesis. It begins with an overview of the heart's anatomy and the cardiac cycle, which generate the electromagnetic wave. Then, it introduces the MCG and ECG sensor modalities and MRI imaging, followed by a presentation of the Maxwell equations and their quasi-static approximation for describing the transmission of electromagnetic waves from the heart to the sensors. The chapter then derives the equations for solving the forward problem and describes the BEM and FEM models. Finally, it presents our implementation of the LORETA and STKF with the autoregressive state-space and ssGARCH models.

Chapter 3 describes the pipeline for solving the forward and inverse problems of the heart. The chapter begins by discussing the environment and setup for our data acquisition of MCG, ECG, and MRI. Then, it explains how the anatomical model was generated based on the MRI through segmentation and meshing. Next, the chapter discusses the forward modelling and calculation of the LFM. Finally, I present my implementation of the inverse problems and show some techniques.

Chapter 4 presents two studies. The first study focuses on generating two MCG datasets and analysing them with different inverse problem methods to compare the effect of noise on the accuracy of source estimation. The second study is concerned with generating SQUID MCG datasets from different directions, orientations, and numbers of sensors to determine the best SQUID MCG setup.

Chapter 5 reports studies and their results of source localisation from individual datasets using the STKF with autoregressive and ssGARCH models.

Chapter 6 offers a discussion and suggestions for future works and further development.

1.5 The Contribution of this Thesis

This work makes significant contributions to the fields of heart research by developing and applying the Spatio-temporal Kalman filter and ssGARCH models. The novel application of these models to MCG and ECG datasets improves the accuracy of source imaging and enhances our understanding of the underlying physiological processes.

The author has also made important contributions to the research community through the publication of several articles in peer-reviewed journals, with the author as the first author. These publications demonstrate the author's expertise in the field and include:

1. Nawar Habboush*, Laith Hamid*, Natia Japaridze, Gert Wiegand, Ulrich Heute, Ulrich Stephani, Andreas Galka, and Michael Siniatchkin. *The choice of the source space and the Laplacian matrix in LORETA and the spatio-temporal Kalman filter EEG inverse methods.* In *Proceedings of the IEEE Engineering in Medicine and Biology Conference (EMBC)*, pages 2745-2749, 2015. [Online]. Available: `https://doi.org/10.1109/EMBC.2015.7318960` (* equal contributorship)

2. Nawar Habboush, Laith Hamid, Michael Siniatchkin, Ulrich Stephani, and Andreas Galka. *Pipeline for Forward Modeling and Source Imaging of Magnetocardiographic Recordings via Spatiotemporal Kalman Filtering.* In *Proceedings of the IEEE Engineering in Medicine and Biology Conference (EMBC)*, pages 199-202, 2018. [Online]. Available: `https://doi.org/10.1109/EMBC.2018.8512188`

3. Laith Hamid*, Nawar Habboush*, Philipp Stern, Natia Japaridze, Ümit Aydin, Carsten H.Wolters, Jens Christian Claussen, Ulrich Heute, Ulrich Stephani, Andreas Galka, and Michael Siniatchkin. *Source imaging of deep-brain activity using the regional spatiotemporal Kalman filter.* In *Computer Methods and Programs in*

Biomedicine, vol. 200, 2020. [Online]. Available: `https://doi.org/10.1016/j.cmpb.2020.105830` (* equal contributorship)

In addition, the author has co-authored several studies and publications, further showcasing his expertise and contributions to the field:

1. SE Peter, D Mederer, N Habboush, E Lyzhko, M Siniatchkin, V Moliadze. *EP 135. Boosting cognitive control with transcranial alternating current stimulation.* In *Clinical Neurophysiology*, vol. 127, pages e297-e298, 2016. Available: `https://doi.org/10.1016/j.clinph.2016.05.175`
2. SE Peter, D Mederer, N Habboush, E Lyzhko, M Siniatchkin, V Moliadze. *The effect of transcranial alternating current stimulation (tACS) on inhibitory control and error monitoring in healthy adults.* In *Brain Stimulation: Basic, Translational, and Clinical Research in Neuromodulation*, vol. 10, page 514, 2017. Available: `https://doi.org/10.1016/j.brs.2017.01.502`
3. C Messow, K Waschull, T Stenner, E Lyzhko, N Habboush, L Hamid, V Moliadze, M Siniatchkin. *P 53 Impact of acoustic stimulation on motor response inhibition and error monitoring.* In *Clinical Neurophysiology*, vol. 128, page e355, 2017. Available: `https://doi.org/10.1016/j.clinph.2017.06.131`
4. Anna Jodko-Władzińska, Nawar Habboush, Rüdiger Brühl, Thomas Middelmann, Andreas Galka, Lutz Trahms, Tilmann H Sander. *Anatomy-adapted sensor holder for personalized OPM magnetoencephalography and magnetocardiography.* In *Today's Noise Tomorrow's Signal (TNTS'2019), 2019, 13-02-2019 - 15-02-2019, Berlin, Germany*, page 51-52, 2019.

As a doctoral student at the University of Kiel, the author not only gained valuable academic knowledge but also honed his mentoring and supervisory skills by guiding eleven students through four distinct master's projects in the international program of Digital Communications, which offers Advanced Topics Labs. These projects were:

- Medical Signal Processing:Electroencephalography (EEG) Simulation and Analysis, Winter semester 2015-2016
- ECG & MCG Data Interpolation Techniques, Winter semester 2016-2017
- Solution of the Inverse Problem using Beamforming, Winter semester 2017-2018
- Implementation Inverse Problem Using non-linear Kalman Filter, Winter semester 2018-2019

Chapter 2

Medical and Theoretical Background

In this chapter, I delve into the theoretical foundations of my thesis. I begin by outlining the anatomy of the heart and exploring various heart-related diseases and malfunctions. Then I explain the electrophysiology of the heart and how that can generate the ECG that we can measure. Next, I survey the state-of-the-art technologies employed for heart diagnosis and provide a comprehensive overview of the devices currently used for acquiring heart data by using electric sensors like ECG or magnetic sensors like MCG and OPM.

Subsequently, I delve into the algorithmic and mathematical models that we have adopted to address the challenging problem of heart inverse modelling. I start by explaining Maxwell equations, which can mathematically explain how the electrophysiology of the heart are propagated and can be eventually be detected by sensors, I also derive a Quasi-Static approximation of the Maxwell equations for the heart to be able to ignore the travelling time of the electromagnetic wave because the travelling distance between the heart and the sensors with comparison to the wavelength is short.

Subsequently, I delve into the forward problem, elucidating how the propagated electrical field can be computed on the sensors and the process of constructing the Leadfield Matrix (LFM). This is followed by an explanation of the Biot-Savart Law, which is employed to calculate the magnetic field derived from the electrical field. Lastly, I expound on the boundary and finite element methods, detailing their application in the segmentation of MRI.

Progressing further, I provide a comprehensive explanation of the inverse method solutions that have been utilized. This begins with an exploration of more conventional methods such as MNE and LORETA. Subsequently, the discussion advances to the Kalman filter and its sophisticated variants, including the Spatiotemporal Kalman filter. The discourse culminates with an examination of its advancements through the application of a novel Laplacian and the GARCH models.

2.1 Anatomy of the Heart

The heart is a vital organ in the human body responsible for pumping blood and distributing oxygen to organs and cells. The heart is a hollow organ that consists mainly of the muscular wall called myocardium, which divides it into four chambers. These chambers are filled with blood: two atria that receive blood from the lungs and the body, and two ventricles that push blood to the lungs and the body. The heart is approximately the size of an individual's clenched fist and is located in the middle of the chest, slightly to the left.

The heart receives deoxygenated blood from the body through the superior and inferior vena cava, which flows into the right atrium. The atria then contract and push the blood through the tricuspid valve into the right ventricle. In the second half of the heart's cycle, the right ventricle pumps deoxygenated blood to the lungs through the pulmonary valve. The lungs exchange gases with the environment through respiration, releasing carbon dioxide from the blood generated by the metabolism process and exchanging it with oxygen molecules. The heart then receives oxygenated blood into the left atrium through the pulmonary vein. When the left atrium contracts, the blood flows to the left ventricle through the mitral valve, and finally, the left ventricle, which has the strongest muscles in the heart, pushes the oxygenated blood to the rest of the body.

Figure (2.1) shows the anatomy of the human heart, indicating the chambers, valves, and the directions of the blood flow in the blood vessels.

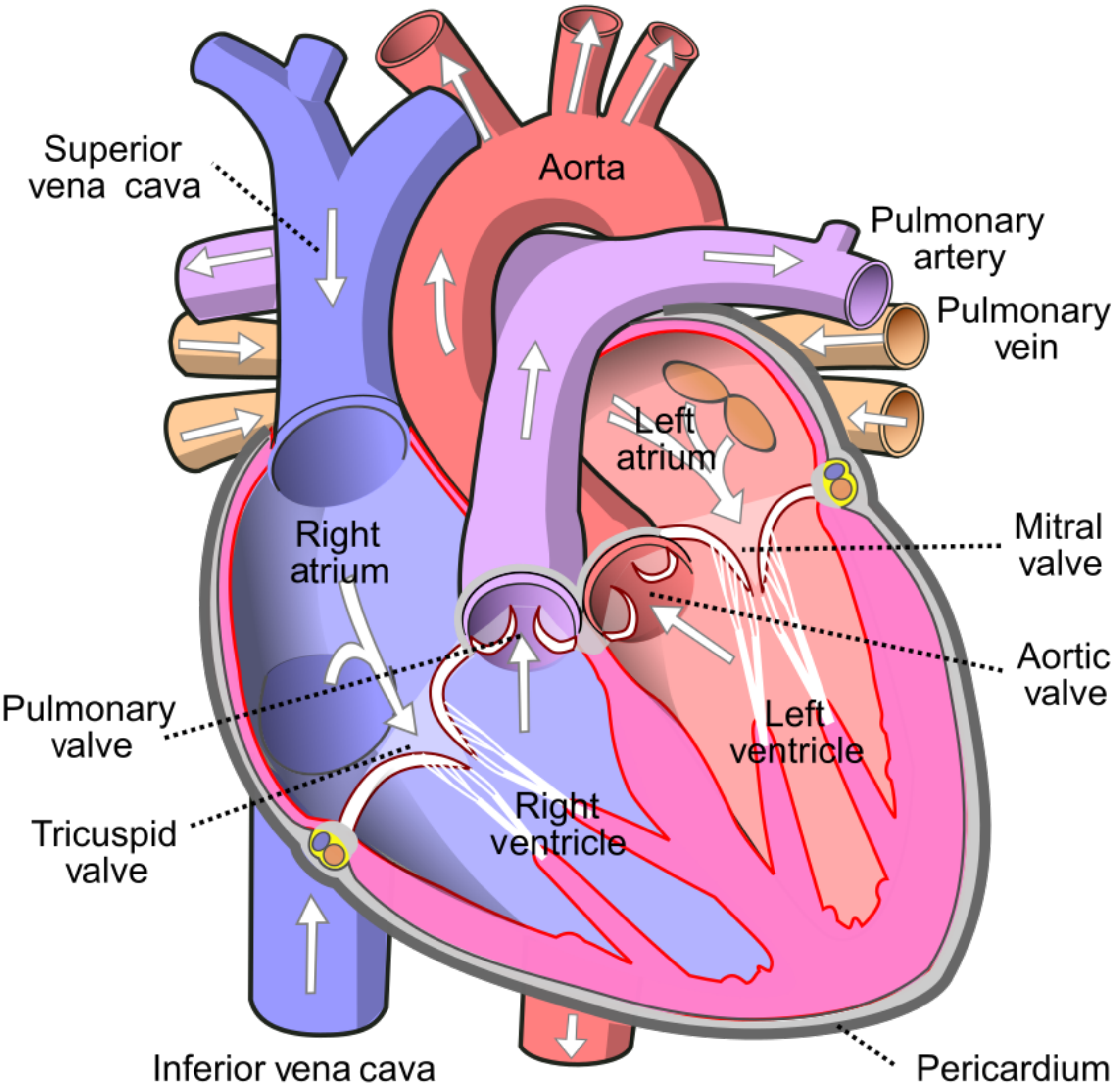

Figure 2.1: Anatomy of the human heart, showing the chambers, valves, and directions of blood flow in the blood vessels [Wik20].

2.2 Electrophysiology of the Heart

The heartbeat is a result of a complex interplay of electrical and chemical processes within the heart. The action potential in the heart is a rapid change in the voltage across the membrane of the heart cells. The voltage changes occur due to changes in the concentration of sodium (Na^+) and potassium (K^+) ions inside and outside the membrane through the ion channels, which generate a polarization and depolarization. The flow of sodium and potassium ions happens through the ion channels. Figure (2.2) shows the chemical changes inside and outside the heart cells with respect to time. The heart muscles, also called myocardium, respond to the action potential by contracting and relaxing, which eventually moves the blood inside or outside of the heart.

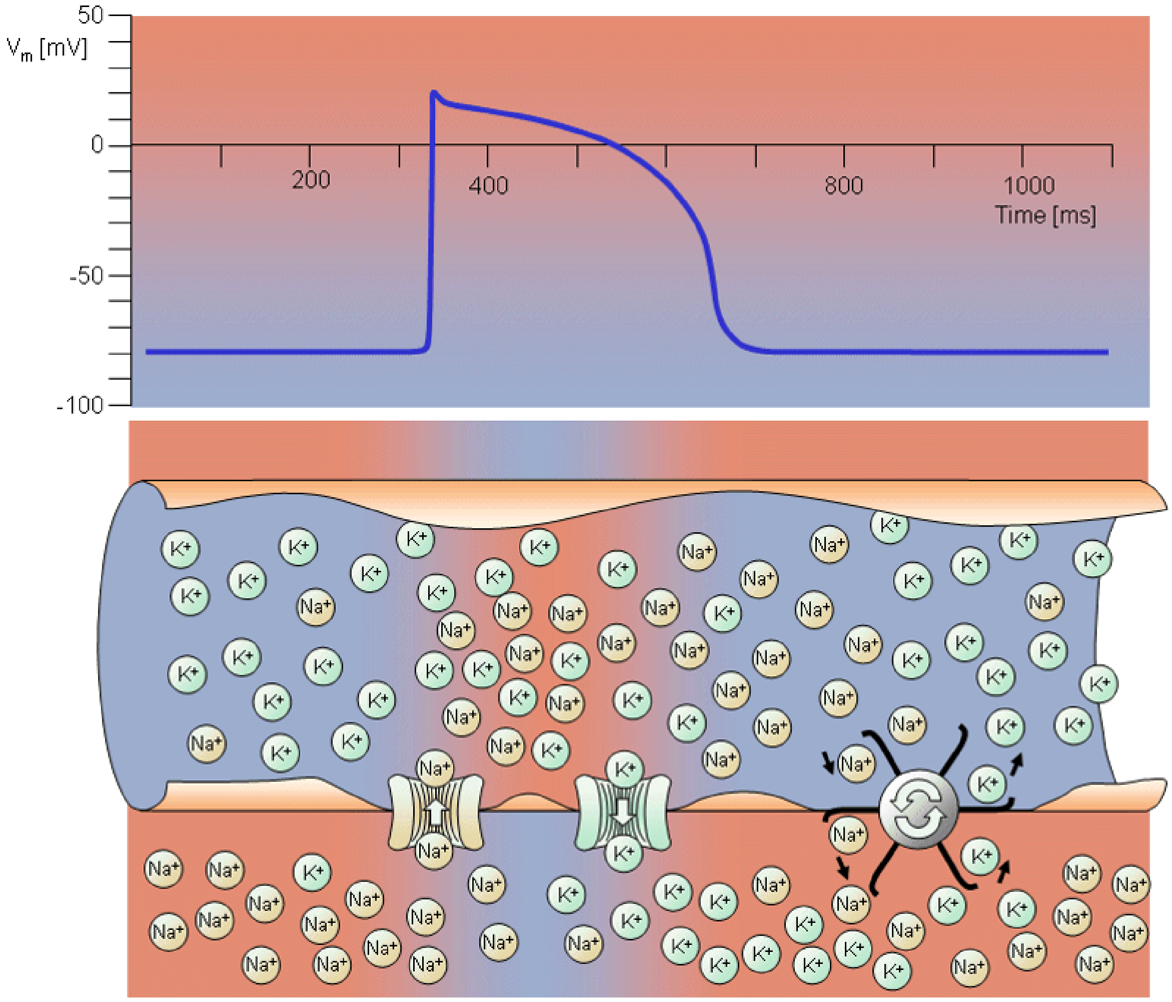

Figure 2.2: The ion exchange in the heart. The upper part shows the changes of voltage across the electrical excitable membrane through a period of 1000 ms. The lower part shows the concentration of sodium (Na^+) and potassium (K^+) between inside and outside the heart cells, also known as myocytes [MP95].

The cardiac conduction cycle can be divided into four stages, each lasting roughly a second.

The first stage starts at the sinoatrial (SA) node, located on the upper part of the right atrium's wall, as shown in figure (2.3). Its tissue has muscle and nervous features. The SA node is a self-excited node that generates action potentials at a rate of 70 pulses per minute. As the activation potential is generated at the SA node, it propagates to both atria but does not transfer to the ventricles.

In the second stage, the activation propagates from the SA node to the atrioventricular (AV) node, which is located at the right-lower side of the wall that separates the atria. It receives the impulse from the SA node and delays it by about 100 ms to give the blood time to flow from the atria to the ventricles. The natural rate of the AV node is 50 pulses per minute, but in the healthy heart, it is triggered by the higher impulse rate coming from the SA node. Therefore, the AV node functions under normal circumstances as a delay and control between the activation pathways in one direction from the SA node to the AV node.

In the third stage, the impulses travel downward from the AV node to a bundle of fibers called the bundle of His. Then the bundle of His splits into the right and left bundles. Each of those right and left bundles extends along the central wall between the two ventricles. The propagation velocity starts very slow in the His bundle, but it increases when the His bundles enter the ventricles.

In the fourth stage, the bundles of His start to split up and diverge into the Purkinje fibers. The activation propagates through the Purkinje fibers to the cells, then from cell to cell as a wavefront across the ventricles from the middle to the outer sides of the ventricles. This activation causes the ventricles to contract and push the blood to the lungs and the rest of the body [MP95].

The sequence of chemical processes and contractions in the heart generates current densities, resulting in magnetic and electrical fields that propagate in various directions. These waveforms sum up to produce the PQRST-complex, which can be detected through MCG and ECG sensors. Figure (2.4) illustrates the generation of ECG PQRST-complex, which involves the production of various waveforms in different regions of the heart with specific time delays.

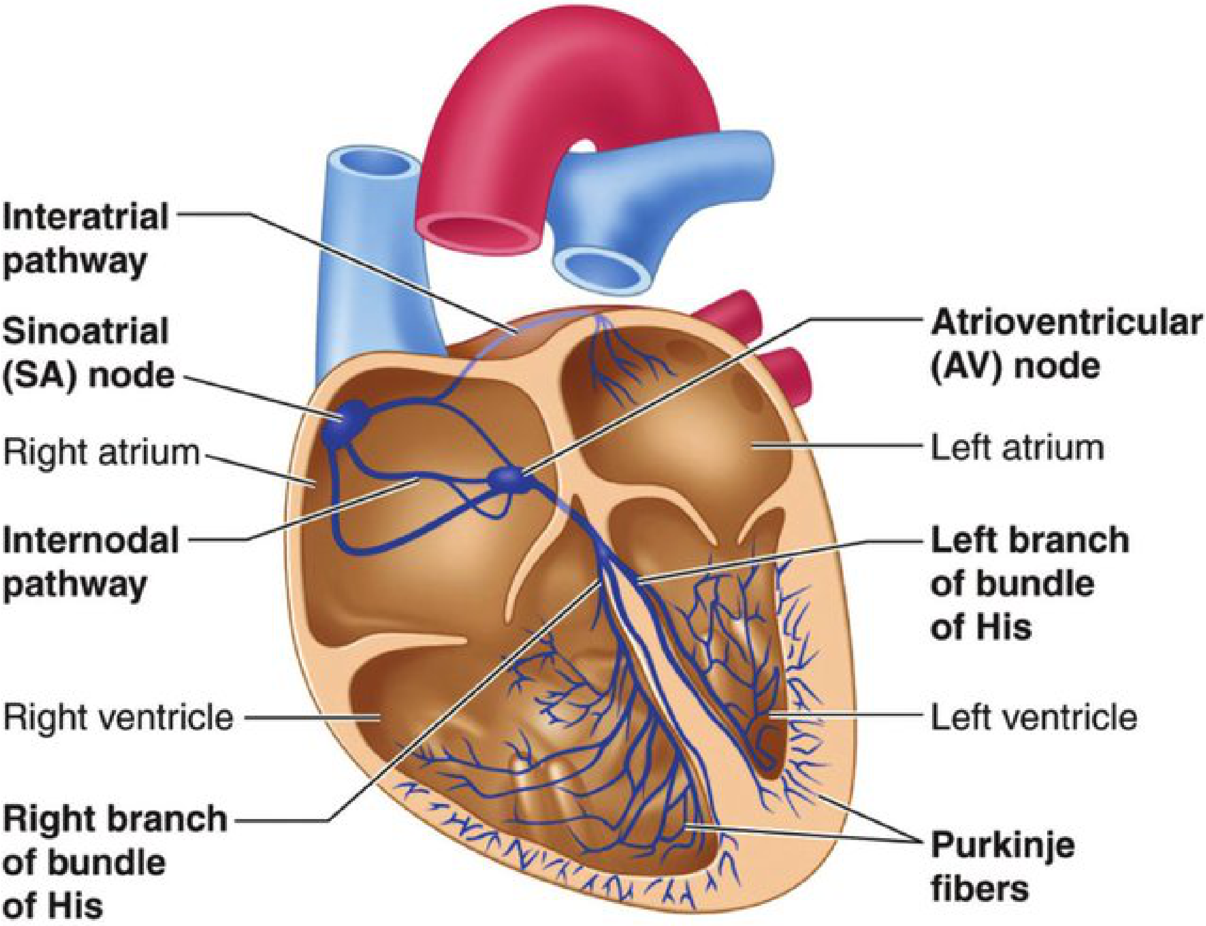

Figure 2.3: The electrical nodes and pathways in the heart are initiated by an activation potential that begins at the Sinoatrial (SA) node on the upper side. This potential then propagates to the atria walls and the Atrioventricular (AV) node. As a result, the atria are activated and blood is pushed from the atria to the ventricles. Subsequently, the activation moves further downwards to the bundles of His located alongside the central wall between the ventricles. Finally, the activation propagates from the middle wall branches to the Purkinje fibers, activating the entire ventricular walls. This activation results in the pumping of blood to the lungs and the rest of the body. [Gan+16].

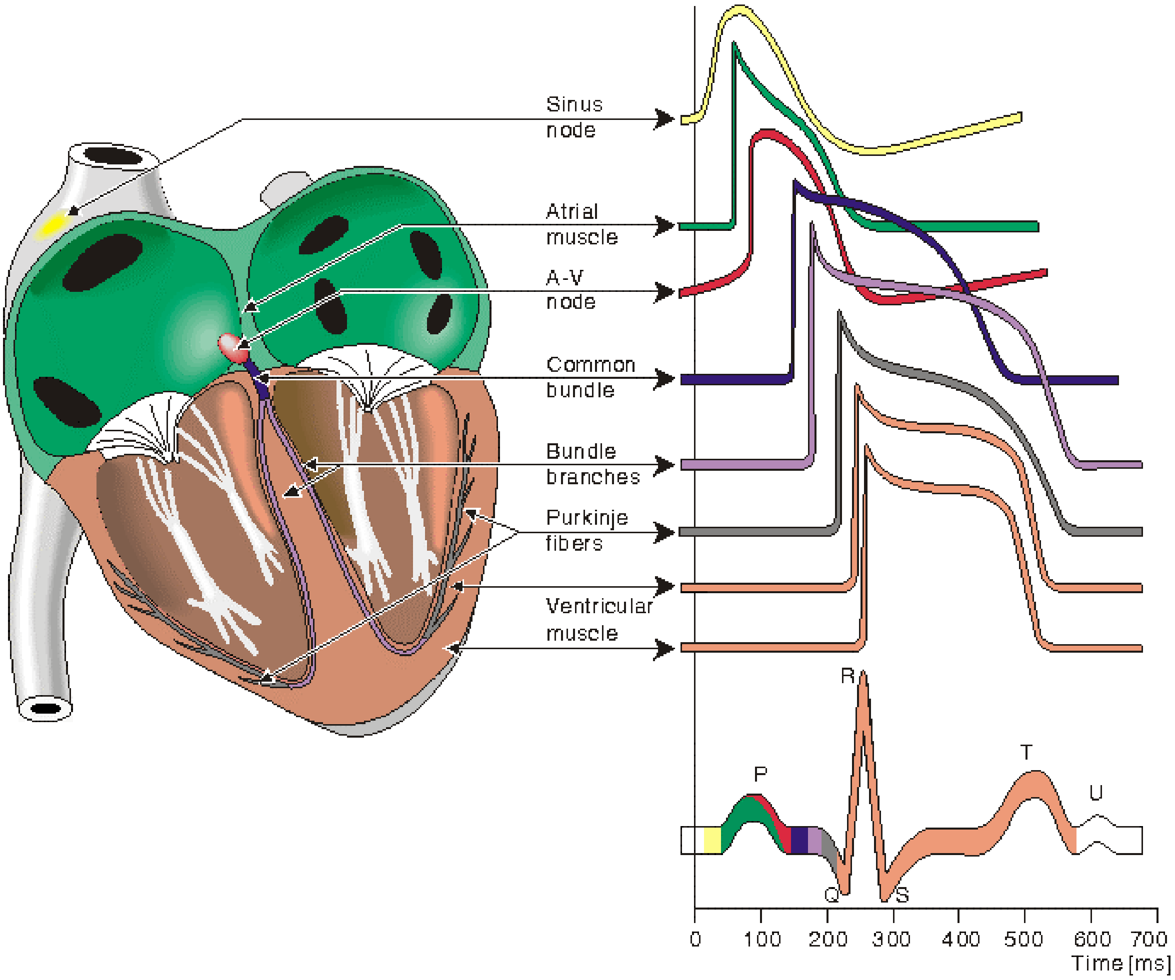

Figure 2.4: Generation of variant waveforms with time delay at different regions in the heart and how these waveforms sum up to construct the ECG PQRST-complex. [MP95]

2.3 Sensors Modalities

2.3.1 Electrocardiography (ECG)

Electrocardiography (ECG) is a vital medical procedure that measures the electrical activity of the heart. It is a non-invasive and painless test that is typically used to diagnose and monitor heart conditions, such as heart attacks, arrhythmias, and heart disease.

During an ECG, small electrodes are placed on the skin around the heart, which detect the electrical impulses that travel through the heart and transmit them to a machine. The machine records the activity as a series of lines on a graph, called a tracing.

The tracing represents the heart's electrical activity as it moves through the different stages of the cardiac cycle, which includes the contraction and relaxation of the heart muscle. By analysing the ECG tracing, healthcare providers can determine the heart's rate and rhythm, as well as the strength and timing of the electrical signals in the heart. This information can help them diagnose a range of heart conditions, including problems with the heart's structure, such as damaged heart muscle or abnormal blood flow, and problems with the heart's electrical system, such as abnormal heart rhythms or conduction problems.

ECG technology consists of three main components: electrodes, an amplifier, and a recorder. The electrodes are placed on the skin and pick up the electrical signals from the heart. The amplifier amplifies the signals, making them strong enough to be recorded. The recorder, which can be a paper chart or a digital display, records the amplified signals as a tracing.

ECG is an essential tool in the diagnosis and treatment of heart disease and other cardiac conditions. It is usually performed in a healthcare setting, such as a hospital or doctor's office, but portable ECG machines are also available for use at home or in other settings.

2.3.2 Magnetocardiography (MCG)

Magnetocardiography (MCG) is a non-invasive medical technique that employs highly sensitive magnetometers to measure and record the magnetic fields generated by the electrical activity of the heart. This technique allows for the evaluation of the heart's electrical activity without the need for electrodes or invasive devices such as catheters. MCG is typically used to diagnose and assess the severity of heart disorders, including arrhythmias (irregular heart rhythms) and coronary artery disease. Additionally, it can be used to monitor the effectiveness of treatment for these conditions.

The procedure for MCG involves the patient lying down on a table, the magnetometers, which are placed around the patient's chest, measure the magnetic fields produced by the electrical activity of the heart and record them as an MCG tracing.

Magnetocardiography (MCG) is a valuable tool for the diagnosis and management of heart disorders, providing valuable information that is not available through other methods. However, there are a few potential limitations to its use as a medical imaging technique. Firstly, MCG requires specialised equipment and trained personnel to perform, which can limit its availability in all medical centres. Additionally, the cost of the equipment can be high. While MCG has higher sensitivity than ECG, it may not be able to detect all abnormalities in the electrical activity of the heart due to the different orientations of the magnetic and electric fields. Interference from other electronic devices, such as MRI machines, can also be an issue for MCG, necessitating the use of well-shielded rooms. Despite these limitations, MCG remains a valuable tool in the diagnosis and management of heart disorders.

There are several types of magnetometers, including fluxgate magnetometers and SQUID (superconducting quantum interference device) magnetometers. Each type works differently, but all magnetometers rely on the principle that the strength of a magnetic field is proportional to the force it exerts on a moving charged particle.

Fluxgate magnetometers use a coil of wire wrapped around a core of magnetic material. When a magnetic field is applied to the coil, it causes the magnetic material in the core to become magnetized. This, in turn, causes the magnetic field in the coil to change, which can be measured by the magnetometer.

SQUID magnetometers are highly sensitive magnetometers that use superconducting materials to detect very small changes in a magnetic field. They work by using a superconducting loop to create a current that is sensitive to changes in the magnetic field. When the magnetic field changes, it causes a change in the current, which can be detected by the magnetometer. Overall, magnetometers work by detecting the strength and direction of a magnetic field and using this information to measure the strength of the field. We used the SQUID magnetometer in our measurements.

2.3.3 Optically Pumped Magnetometers (OPM)

Optically Pumped Magnetometers (OPMs) are a type of magnetometer that uses the magnetic properties of atoms to measure magnetic fields. OPMs work by optically pumping atoms into a specific energy state using a laser, and then measuring the magnetic field based on the orientation of the excited atoms.

In an OPM, a sample of atoms is placed in a magnetic field and then optically pumped using a laser beam. The laser beam excites the electrons in the atoms, causing them to become aligned with the magnetic field. The orientation of the excited atoms is then measured using another laser beam, which is used to probe the alignment of the atoms.

OPMs are highly sensitive and can be used to measure very small magnetic fields, making them useful for a variety of applications, including geomagnetic field measurements, mineral exploration, and medical imaging. They are also relatively simple to operate and do not require the use of cryogenics, making them a convenient and practical choice for many applications.

2.4 Magnetic Resonance Imaging (MRI)

Magnetic resonance imaging (MRI) is a medical imaging technique that uses a strong magnetic field and radio waves to produce detailed images of the inside of the body. MRI is a non-invasive procedure that is painless and does not expose the patient to ionizing radiation.

During an MRI scan, the patient is placed in a large cylindrical machine called an MRI scanner. The scanner contains a powerful magnet that generates a strong magnetic field. Radio waves are then used to excite the protons (hydrogen atoms) in the patient's body, causing them to emit a radio frequency signal that is detected by the MRI scanner.

The strength and location of the magnetic field, as well as the radio frequency signals emitted by the protons, are used to create detailed images of the inside of the body. These images can be used to diagnose a wide range of medical conditions, including injuries, tumors, and cardiovascular diseases. MRI is a powerful and widely used medical imaging technique that allows doctors to see detailed images of the inside of the body without the use of ionizing radiation.

2.5 Quasi-Static Approximation of Maxwell Equation

In order to calculate the magnetic field ($\boldsymbol{B}$) generated by the action potential in the heart, we need to know two types of information: the electrical currents generated by the heart and the conductivity of the torso tissues. The conductivity of the torso tissues is calculated from the MRI through segmentation, as explained in chapter (1). To calculate $\boldsymbol{B}$, we used Maxwell's equations and the continuity equation.

The first of Maxwell's equations is Gauss's Law for electricity, which states that the total electric flux through a closed surface is equal to the charge enclosed within that surface, divided by the permittivity of free space, denoted as ϵ_0. For simplicity, and because the permittivity of the torso tissues is not known, it is often assumed to be the same as that of free space. This allows for the calculation of electric fields within the body using this equation.

$$\nabla \cdot \boldsymbol{E} = \frac{\rho}{\epsilon_0}, \tag{2.1}$$

where $\boldsymbol{E}$ is the electrical field, ρ is the electric charge density and ϵ_0 is the permittivity in free space.

The second of Maxwell's equations is Gauss's Law for magnetism, which states that the magnetic field has no divergence. This means that the total magnetic flux through any closed surface is zero, and there are no isolated magnetic charges. Instead, the magnetic field lines always form closed loops.

$$\nabla \cdot \boldsymbol{B} = 0. \tag{2.2}$$

The third equation of electromagnetism is Faraday's Law, which states that a changing magnetic field over time will induce an electric field that swirls around it. This phenomenon is known as electromagnetic induction and is the basis for the operation of many electrical devices, such as generators and transformers.

$$\nabla \times \boldsymbol{E} = -\frac{\partial \boldsymbol{B}}{\partial t}. \tag{2.3}$$

The fourth equation of electromagnetism is Ampere's Law, which states that a magnetic field is generated by a changing electric field or by an electric current density. This law describes the relationship between electric currents and the magnetic fields they produce, and is used to calculate the magnetic field generated by a given current distribution.

$$\nabla \times \boldsymbol{B} = \mu_0(\vec{\boldsymbol{j}} + \epsilon_0 \frac{\partial \boldsymbol{E}}{\partial t}), \tag{2.4}$$

where μ_0 is the permeability in free space and $\vec{\boldsymbol{j}}$ is the electric current density.

The relationship between $\boldsymbol{E}$ and $\boldsymbol{B}$ is time-dependent, as equations (2.3) and (2.4) demonstrate. However, since the distance between the heart and sensors is small, we need to determine whether the variance over time is relevant or whether we can assume that the relationship between $\boldsymbol{E}$ and $\boldsymbol{B}$ is static for small distances.

If we use Ohm's law $\vec{\boldsymbol{j}} = \sigma \boldsymbol{E}$ in equation (2.4), we get:

$$\nabla \times \boldsymbol{B} = \mu_0(\sigma \boldsymbol{E} + \epsilon_0 \frac{\partial \boldsymbol{E}}{\partial t}), \tag{2.5}$$

where σ is the conductivity.

To analyse the electric field in frequency domain, we transform the equation (2.5) using the notation $\boldsymbol{E} = \boldsymbol{E}_0 e^{-jwt}$ and $\partial \boldsymbol{E}/\partial t = -j\omega \boldsymbol{E}$. This results in the following expression:

$$\nabla \times \boldsymbol{B} = \mu_0(\sigma - j\epsilon_0\omega)\boldsymbol{E}, \tag{2.6}$$

where ω is the angular frequency and equal to $2\pi f$, f is the frequency and $j = \sqrt{-1}$.

To validate the quasi-static assumption, it is necessary for the first term in equation (2.5) to be significantly greater than the second term ($\sigma \gg \epsilon_0 2\pi f$). In this study, conductivity values ranging from 0.04 S/m to 0.6 S/m were used for different tissue types, with the choice of values and references explained in section (3.2.1). It is worth noting that the frequencies of the important components in the MCG and ECG are below 50 Hz, with the P-wave between 0.67 and 5 Hz, the T-wave between 1 and 7 Hz, and the QRS-complex between 10 and 50 Hz [BF+12; VHA11a; VHA11b]. To simplify the analysis, it is assumed that the permittivity of the torso is equivalent to that of free space (8.854×10^{-12}) due to the low relative permittivity of the human torso at 50 Hz. Therefore, $|\epsilon_0 2\pi f| = 8.854 \times 10^{-12} 2\pi \times 50$, which is considerably smaller than the value of σ ($0.04 < |\sigma| < 0.6$).

This indicates that the time-dependent term is negligible and can be disregarded for simplicity.

The third equation of Maxwell (2.3) is also time-dependent. However, we can neglect the time component here and substitute equation (2.4) in (2.3). To do so, we add an additional curl to the left side:

$$\begin{aligned}\nabla \times \nabla \times \boldsymbol{E} &= -\frac{\partial}{\partial t}(\nabla \times \boldsymbol{B}) \\ &= -\mu_0 \frac{\partial}{\partial t}(\sigma \boldsymbol{E} - j\epsilon_0 \omega \boldsymbol{E}) \\ &= \mu_0 \omega(\epsilon_0 \omega + j\omega\sigma)\boldsymbol{E}.\end{aligned} \tag{2.7}$$

Since the characteristic wavelength of this equation is longer than the distance between the heart and sensors, we can neglect the effect of $\partial \boldsymbol{B}/\partial t$ on this equation.

2.6 Forward Problem

The forward problem in MCG and ECG involves calculating the electrical signals outside the torso based on the current density inside the heart. This is achieved by multiplying the current densities with the lead-field matrix (LFM). The LFM represents the relationship between each MCG or ECG sensor and the source points in the heart. It has dimensions $N_s \times N_j$, where N_s is the number of sensors and N_j is the number of source points. Each source point is represented by three current dipoles in the Cartesian coordinate system. The LFM also includes information about the locations of all sensors and source points.

Building the LFM requires information about the structure of the torso and the conductivities of its tissues. Two commonly used methods for modelling are the Boundary Element Method (BEM) and the Finite Element Method (FEM). Both methods rely on MRI scans to segment the torso organs and assign relevant conductivities to them.

Overall, the forward problem is a crucial step in MCG and ECG analysis, allowing for the calculation of electrical signals outside the body based on internal cardiac activity and open up the way for solving the inverse problem.

2.7 Biot–Savart Law

The forward problem of MCG is connected to the forward problem of ECG through the Biot-Savart law. The Biot–Savart law is a fundamental physical law that describes the magnetic field produced by an electric current. It is named after Jean-Baptiste Biot and Félix Savart, who first derived the law in the early 19th century. [Gri99]

In mathematical terms, the Biot–Savart law can be expressed as follows:

$$\mathbf{B}(\mathbf{r}) = \frac{\mu_0}{4\pi} \int \frac{\mathbf{J}(\mathbf{r}') \times \mathbf{r}''}{r''^2} \mathrm{d}\mathbf{r}' \tag{2.8}$$

here, $\mathbf{B}(\mathbf{r})$ is the magnetic field at a point $\mathbf{r}$, μ_0 is the permeability of free space, $\mathbf{J}(\mathbf{r}')$ is the current density at a point $\mathbf{r}'$, and r'' is the distance between the points $\mathbf{r}$ and $\mathbf{r}'$. The integral is taken over all points $\mathbf{r}'$ where the current is flowing.

The Biot–Savart law is useful for calculating the magnetic field produced by a variety of different configurations of electric current, including straight wires, loops, and more complex arrangements. It is often used in the field of electromagnetism to analyse the behaviour of electric circuits and devices, such as motors and generators. We use Biot-Savart law to calculate the forward problem of the MCG directly from the forward problem of the ECG.

2.8 Boundary and Finite Element Models

In the forward problem, we need to construct a model of the torso that accurately represents the different tissues and their electrical conductivities. There are two main methods for doing this: the boundary element model (BEM) and the finite element method (FEM).

The BEM describes the geometries of the torso tissues using surface meshes, which define the boundaries between different organs or compartments. The inside of each surface mesh is assumed to be homogeneous and have the same conductivity. The BEM is computationally efficient and suitable for models that have a limited number of tissue types. However, it may not be able to capture the detailed anatomical features of the torso, such as the thin layers of different tissues that surround the heart.

The FEM, on the other hand, uses volumetric meshes to represent the geometries of the torso tissues using volume elements. This allows for a more detailed representation of the different tissue layers and their electrical properties. In FEM models, inhomogeneous and anisotropic conductivity can be modelled, making it more flexible than the BEM. However, FEM models have a higher segmentation and computational complexity, and require more computational resources.

Both BEM and FEM models require high-quality torso imaging methods, such as three-dimensional MRI or CT scans. In this thesis, we used MRI because it is a non-invasive method that does not involve X-rays. While CT scans provide higher quality images, they are associated with radiation exposure.

2.9 Inverse Problem Methods

Many scientific fields have systems that can be extended to include additional factors that influence estimation. In time series applications, the primary dynamic is usually time, as is the case in our MCG application and in many other applications. In our application, the system extension can benefit from including the spatial component since our pipeline aims to localise heart activity. Typically, there is an unobserved state that corresponds to the observed data. However, since the state dimensions are often higher than the original data, an inverse problem algorithm is needed to handle the ill-posed dimensions transformation between the original and state dimensions.

There are two main methods for solving the inverse problem in the heart: the equivalent current dipole (ECD) method and the distributed source method (DSM). The ECD method estimates the source activity in the heart by assuming that the activity is generated by a single point source, the ECD. This method simplifies the solution of the inverse problem but can result in loss of information about the source activity. The DSM method estimates the source activity by dividing the heart into multiple small sources that can be located anywhere in the heart. The DSM method can provide more detailed information about the source activity, but it has higher computational complexity.

There are various DSM inverse problem methods that use least-square or Tikhonov regulation methods like LORETA, as described in part (2.9.2). These methods calculate an instant solution at every time point, ignoring the data time dynamics. Temporal smoothness can be added to instantaneous methods, as in the publications [BG97] and [Sch+02]. This method has been generalized to form a general spatial and temporal model, as described in [Yam+04]. However, from a dynamical systems viewpoint, this temporal smoothing method is stochastic in an unobserved state-space and is thus not optimal [GYO04].

In addition, there are other methods used for the solution of the inverse problem, such as the Bayesian approach, the minimum norm method, and the MUSIC algorithm. These methods aim to improve the accuracy of the source estimation by incorporating additional information about the heart and the measurement process. The choice of the method depends on the specific application and the available resources.

The inverse problem for the heart is a process of estimating the original heart activity from MCG and/or ECG measurements outside the torso. This estimation is based on the LFM, which is calculated from solving the forward problem discussed in section (2.6). The LFM represents the mapping between the source points and the sensors.

We consider the spatiotemporal system to have unobservable states denoted by $j(v,t)$, where v represents the space and t represents the time. Digitalization of the system means that the space is divided into N_v grid points, and we select a segment of MCG data with N_t time points for analysis. The matrix $\underline{\boldsymbol{J}}$ has dimensions of $N_j \times N_t$, where $N_j = 3 \times N_v$, because each grid point has three activity components in the three Cartesian directions. The activity across the source space grid at a particular time point t can be represented as:

$$\vec{\boldsymbol{j}}_t = (j_{1,t}, ..., j_{N_j,t})^\top \tag{2.9}$$

On the other hand, the data matrix, denoted by $\underline{\boldsymbol{Y}}$, has dimensions of $N_y \times N_t$, where N_y is the number of observable sensor points. Unlike the source points, observation points only have one value because each sensor usually has one orientation depending on the sensor's design and physics, such as SQUIDs and electrodes. The observed values for all sensors at one time point t can be represented as:

$$\vec{\boldsymbol{y}}_t = (y_{1,t}, ..., y_{N_y,t})^\top \tag{2.10}$$

Since the number of the MCG sensors is much smaller than the number of unobservable source space ($N_y \ll N_v$), we assume a linear relationship between the sensor and source spaces and predict approximately using:

$$\vec{\boldsymbol{y}}_t = \underline{\boldsymbol{K}}\vec{\boldsymbol{j}}_t + \vec{\boldsymbol{\epsilon}}_t, \tag{2.11}$$

where $\vec{\boldsymbol{y}}$ is the measurement vector with dimensions of $N_y \times 1$ and N_y is the number of sensors that can be electrodes, SQUIDs, OPMs, or a combination of them. $\underline{\boldsymbol{K}}$ is the leadfield matrix with dimensions of $N_y \times N_j$. As the heart is a three-dimensional volume and the current density can be omnidirectional, there are three values for each source point of the $\vec{\boldsymbol{j}}$ vector corresponding to the Cartesian coordinate system, x, y, and z, therefore $N_j = 3 \times N_v$. $\vec{\boldsymbol{\epsilon_t}}$ represents the measurement error vector. The mathematical formulation presented in this section is based on [Gal+04], [Hab14], [Ham18], and [Ste08].

In this thesis we used the Minimun Norm Estimation (MNE), Low-Resolution Electromagnetic Tomography (LORETA), Kalman Filter and its developed version of Spatiotemporal Kalman Filter (STKF) and the State-Space Generalized Autoregressive Conditional Heteroskedasticity with the Spatiotemporal Kalman Filter (ssGARCH-STKF). All the algorithms we are using are DSMs.

2.9.1 Minimum Norm Estimation (MNE)

Minimum norm estimation (MNE) is a method used in neuroimaging to estimate the neural sources of electromagnetic signals such as those recorded by magnetoencephalography (MEG) or electroencephalography (EEG). In the same way, we can use it for the heart imaging using the ECG and MCG. The method attempts to find a solution that estimates the heart sources of the signals while minimizing the overall power or norm of the sources, and this is what the name "minimum norm" suggests.

The main idea behind MNE is to find a source distribution that best explains the observed data while also trying to keep the estimated sources as small as possible. This is achieved by formulating the inverse problem as an optimization problem where the goal is to minimize the norm of the sources while ensuring that the solution explains the data.

The MNE method is based on the linear inverse problem, where the goal is to estimate the sources from the measurements. The linear inverse problem can be mathematically formulated as in equation (2.11).

The MNE solution is obtained by minimizing the following objective function:

$$\mathrm{MNE}\left(\vec{\boldsymbol{j}}\right) = \lambda \left\|\vec{\boldsymbol{j}}_t\right\|^2 + \left(\vec{\boldsymbol{y}}_t - \underline{\boldsymbol{K}}\vec{\boldsymbol{j}}_t\right)^\top \underline{\boldsymbol{\Sigma}}_{\vec{\epsilon}}^{-1} \left(\vec{\boldsymbol{y}}_t - \underline{\boldsymbol{K}}\vec{\boldsymbol{j}}_t\right) \tag{2.12}$$

where λ is the regularisation parameter, $\left\|\vec{\boldsymbol{j}}_t\right\|^2$ is the norm of $\vec{\boldsymbol{j}}_t$ (L2 norm is commonly used), $\underline{\boldsymbol{\Sigma}}_{\vec{\epsilon}}^{-1}$ is the inverse of the noise covariance matrix, and $\left(\vec{\boldsymbol{y}}_t - \underline{\boldsymbol{K}}\vec{\boldsymbol{j}}_t\right)$ is the residual error.

The first term in the objective function, $\lambda \left\|\vec{\boldsymbol{j}}_t\right\|^2$, is a regularization term that tries to keep the estimated sources small. The second term, $\left(\vec{\boldsymbol{y}}_t - \underline{\boldsymbol{K}}\vec{\boldsymbol{j}}_t\right)^\top \underline{\boldsymbol{\Sigma}}_{\vec{\epsilon}}^{-1} \left(\vec{\boldsymbol{y}}_t - \underline{\boldsymbol{K}}\vec{\boldsymbol{j}}_t\right)$, is a data-fitting term that tries to ensure that the solution is consistent with the data. The MNE solution is obtained by finding the $\vec{\boldsymbol{j}}_t$ that minimizes the objective function.

It is important to note that MNE is a linear method and assumes that the underlying sources are linear and Gaussian. In practice, the MNE solution may not be accurate if the assumptions are not met. Non-linear methods and other regularization techniques can be used to improve the accuracy of the solution in such cases. [HI94] [HKS10]

2.9.2 Low-resolution Electromagnetic Tomography (LORETA)

In the field of source localization, the method proposed by Pascual-Marqui et al. [PMML94; PM95; PM99] has gained wide acceptance. In this method, spatial smoothing is applied to the source points at each time point. Specifically, a smoothness constraint is imposed on the six nearest neighbouring points that lie on a sphere with a radius equal to or less than the grid spacing resolution, with fewer neighbours for border grid points. This corresponds to using a regularly distributed source space. The cost function of LORETA searches for a solution that minimizes the current density $\vec{\boldsymbol{j}}$ and is given by:

$$F(j) = \left\|\vec{\boldsymbol{y}} - \underline{\boldsymbol{K}}\vec{\boldsymbol{j}}\right\|^2 + \lambda^2 \left\|\underline{\boldsymbol{L}}\vec{\boldsymbol{j}}\right\|^2, \tag{2.13}$$

where λ is the regularization parameter, which balances the data term $\left\|\vec{\boldsymbol{y}} - \underline{\boldsymbol{K}}\vec{\boldsymbol{j}}\right\|$ and the constraint term $\left\|\tilde{\vec{\boldsymbol{j}}}\right\|^2$. The term $\left\|\vec{\boldsymbol{y}} - \underline{\boldsymbol{K}}\vec{\boldsymbol{j}}\right\|$ represents the fit to the measured data, while the term $\left\|\tilde{\vec{\boldsymbol{j}}}\right\|^2$ is the smoothness constraint.

We used Akaike Bayesian Information Criterion (ABIC) to estimate the hyperparameter λ, as in [Yam+04; Gal+04]. ABIC uses the type II log-likelihood.

The Laplacian current density, $\tilde{\vec{\boldsymbol{j}}}$, is calculated using:

$$\tilde{\vec{\boldsymbol{j}}}_t = \underline{\boldsymbol{L}}\vec{\boldsymbol{j}}_t \tag{2.14}$$

where $\underline{\boldsymbol{L}}$ is the Laplacian matrix, with dimensions $N_j \times N_j$ and N_j is the number of states and N_v is the number of voxel points as $N_j = 3N_v$. The Laplacian matrix, which is used to impose the smoothness constraint, can be calculated as:

$$\underline{\boldsymbol{L}} = (\underline{\boldsymbol{I}}_{N_v} - \frac{1}{6}\underline{\boldsymbol{\Omega}}) \otimes \underline{\boldsymbol{I}}_3 \tag{2.15}$$

where $\otimes$ is the Kronecker product operator, $\underline{\boldsymbol{\Omega}}$ is the two-dimensional matrix of $N_v \times N_v$, representing the neighbouring relationship among all source points. Specifically, $\underline{\boldsymbol{\Omega}}v\acute{v} = 1$ if the source points of v and $\acute{v}$ are neighbours, otherwise $\underline{\boldsymbol{\Omega}}v\acute{v} = 0$. Every source point has six neighbours, which are its direct neighbours in the positive and negative directions of the three axes (x, y, and z) [GYO04].

$$\Omega_{\acute{v}v} = \begin{cases} 1 & \text{if } \acute{v} \text{ is a neighbour of } v \\ 0 & \text{otherwise} \end{cases} \tag{2.16}$$

The matrices $\underline{\boldsymbol{I}}_{N_v}$ and $\underline{\boldsymbol{I}}_3$ are identity matrices with dimensions N_v and 3, respectively. An identity matrix is a square matrix with ones along the diagonal from the upper left to the lower right, and zeros in all other positions. It is denoted by the symbol $\underline{\boldsymbol{I}}_n$, as its dimensions are $n \times n$. The identity matrix is a special case of a diagonal matrix, and it has the property that when multiplied by any matrix of appropriate size, it leaves the matrix unchanged.

This is a general definition of the Laplacian matrix; a more detailed definition with the introduction of a new Laplacian definition is in subsection (2.9.6).

The LORETA inverse solution is typically implemented as follows:

$$\vec{\boldsymbol{j}} = (\underline{\boldsymbol{K}}^\top \underline{\boldsymbol{K}} + \lambda^2 \underline{\boldsymbol{L}}^\top \underline{\boldsymbol{L}})^{-1} \underline{\boldsymbol{K}}^\top \vec{\boldsymbol{y}} \tag{2.17}$$

However, this equation involves the calculation of the inverse of high-dimensional matrices, which can be computationally expensive. Therefore, a more efficient implementation has been derived in [Yam+04] and [Gal+04]. The current density $\vec{\boldsymbol{j}}$ in the simplified implementation can be calculated using the following equation:

$$\vec{\boldsymbol{j}} = \underline{\boldsymbol{L}}^{-1} \underline{\boldsymbol{V}} diag(\frac{s_i}{s_i^2 + \lambda^2}) \underline{\boldsymbol{U}}^\top \vec{\boldsymbol{y}} \tag{2.18}$$

Here, $\underline{\boldsymbol{L}}$, $\underline{\boldsymbol{V}}$, and $\underline{\boldsymbol{U}}$ are obtained from the Singular Value Decomposition (SVD) of the $\underline{\boldsymbol{K}}$ matrix, and λ is the regularization parameter. The $\underline{\boldsymbol{K}}$ matrix is transformed into $\underline{\tilde{\boldsymbol{K}}}$ as follows:

$$\underline{\tilde{\boldsymbol{K}}} = \underline{\boldsymbol{K}\boldsymbol{L}}^{-1}, \tag{2.19}$$

Then, the SVD is applied on the $\underline{\boldsymbol{\tilde{K}}}$ matrix, which decomposes it into three matrices: $\underline{\boldsymbol{S}}$, $\underline{\boldsymbol{V}}$, and $\underline{\boldsymbol{U}}$. This process reduces a dataset containing a large number of values to a dataset containing significantly fewer values, enabling faster calculations. The decomposition of $\underline{\boldsymbol{\tilde{K}}}$ can be described as follows:

$$\underline{\boldsymbol{\tilde{K}}} = \underline{\boldsymbol{USV}}^{\top} \tag{2.20}$$

To optimize the LORETA inverse solution, the ABIC optimization method is often used. This method aims to find the Maximum Likelihood (ML) by minimizing the ABIC value, which is calculated as:

$$\mathrm{ABIC} = -2\mathcal{L}^{(II)}\left(\sigma_{\vec{\epsilon}}, \lambda\right) + 2N_{LOR} \tag{2.21}$$

Here, $\mathcal{L}^{(II)}\left(\sigma_{\vec{\epsilon}}, \lambda\right)$ is the type-II log-likelihood, N_{LOR} is the number of hyperparameters to be optimised, it is added to punish the optimisation method. The higher the number of the hyperparameters, the higher is the punishment. $\sigma_{\vec{\epsilon}}^2$ is the measurement noise variance, which can be estimated as:

$$\sigma_{\vec{\epsilon}}^2 = \frac{1}{N_y} \sum_{i=1}^{N_y} \frac{\lambda^2}{\lambda^2 + s_i^2} \overline{y}_i^2 \tag{2.22}$$

Here, s_i is the i^{th} singular value of the $\underline{\boldsymbol{S}}$ matrix and $\overline{y}_i$ is the i^{th} scalar component of:

$$\vec{\overline{\boldsymbol{y}}} = \underline{\boldsymbol{U}}^{\top} \vec{\boldsymbol{y}} \tag{2.23}$$

The ABIC is typically calculated for a time segment of the data. Assuming T is the total number of time points, the regularization parameter λ can be obtained from the following cost function for a time segment:

$$\mathrm{ABIC}\left(\sigma_{\vec{\epsilon}}, \lambda\right) = TN_y \log \sigma_{\vec{\epsilon}}^2 + T \sum_{i=1}^{N_y} \log \frac{\lambda^2 + s_i^2}{\lambda^2} + \frac{1}{\sigma_{\vec{\epsilon}}^2} \sum_{t=1}^{\top} \sum_{i=1}^{N_y} \frac{\lambda^2}{\lambda^2 + s_i^2} \overline{y}_{i,t}^2 + 2N_{LOR} \tag{2.24}$$

2.9.3 Kalman Filter

The LORETA method uses only neighbouring information to estimate the source, without considering the time dynamics in the data. In contrast, MCG and ECG data recordings have a very high temporal resolution of around 1000 samples per second, where the signal strength of each sample is related to the samples at earlier or later time points. To address this, the dynamical inverse solution and the State-Space Kalman filter have been introduced in [Gal+04].

The KF can be implemented using the following equations:

$$\vec{\boldsymbol{j}}_t = \underline{\boldsymbol{A}}\vec{\boldsymbol{j}}_{t-1} + \vec{\boldsymbol{\eta}}_t \tag{2.25}$$

$$\vec{\boldsymbol{y}}_t = \underline{\boldsymbol{K}}\vec{\boldsymbol{j}}_t + \vec{\boldsymbol{\epsilon}}_t, \tag{2.26}$$

In equation (2.25), $\vec{\boldsymbol{j}}_t$ is the current density vector with dimensions $N_j \times 1$, and it is a sum of two terms. The first term is the current density of the previous time point $\vec{\boldsymbol{j}}_{t-1}$ multiplied by the transition matrix $\underline{\boldsymbol{A}}$. This term describes the temporal development of the time series. The second term is the dynamical noise vector $\vec{\boldsymbol{\eta}}_t$ that represents the modelled noise.

In equation (2.26), $\vec{\boldsymbol{y}}_t$ is the measurement vector, and $\underline{\boldsymbol{K}}$ is the lead-field matrix that maps the source points to the measurement points. It has dimensions of $N_y \times N_j$. $\vec{\boldsymbol{\epsilon}}_t$ is the measurement noise vector.

The lead-field matrix $\underline{\boldsymbol{K}}$ is obtained by solving the forward problem, and $\underline{\boldsymbol{A}}$ is the parameter matrix that can be estimated using traditional estimation methods.

The dynamical noise $\vec{\boldsymbol{\eta}}_t$ is stochastic white Gaussian with variance σ_η^2, which we assume to be the same across all voxels.

To predict the current density, the Kalman filter uses the dynamical model, as shown in equation (2.27):

$$\vec{\boldsymbol{j}}_{t|t-1} = \underline{\boldsymbol{A}}\vec{\boldsymbol{j}}_{t-1|t-1} \tag{2.27}$$

The covariance matrix of the predicted state estimate has the dimensions of $N_j \times N_j$ and can be calculated using equation (2.28):

$$\underline{\boldsymbol{\Sigma}}_{\vec{\boldsymbol{j}}_{t|t-1}} = \underline{\boldsymbol{A}\boldsymbol{\Sigma}_{\vec{\boldsymbol{j}}_{t-1|t-1}}\boldsymbol{A}^\top} + \underline{\boldsymbol{\Sigma}}_{\vec{\boldsymbol{\eta}}} \tag{2.28}$$

To predict the measurement vector, we use the predicted current densities in the following equation:

$$\vec{\boldsymbol{y}}_{t|t-1} = \underline{\boldsymbol{K}}\vec{\boldsymbol{j}}_{t|t-1} \tag{2.29}$$

Since we already know the real measurement data when we want to solve the inverse problem, we subtract the predicted measurement vector from the real measurement vector using the equation:

$$\vec{\boldsymbol{r}}_{\vec{\boldsymbol{y}}_t} = \vec{\boldsymbol{y}}_t - \vec{\boldsymbol{y}}_{t|t-1} \tag{2.30}$$

The measurement error covariance matrix is calculated from the predicted current density covariance matrix and the measurement covariance matrix. This matrix has dimensions of $N_y \times N_y$ and is given by:

$$\underline{\boldsymbol{\Sigma}}_{\vec{\boldsymbol{r}}_{\vec{y}_t}} = \underline{\boldsymbol{K}\boldsymbol{\Sigma}}_{\vec{\boldsymbol{\jmath}}_{t|t-1}}\underline{\boldsymbol{K}}^{\top} + \underline{\boldsymbol{\Sigma}}_{\vec{\boldsymbol{\epsilon}}} \tag{2.31}$$

To stabilize the model between measurement and prediction, we determine the Kalman gain matrix, which has dimensions of $N_j \times N_y$. This matrix is obtained using the following equation:

$$\underline{\boldsymbol{G}}_t = \underline{\boldsymbol{\Sigma}}_{\vec{\boldsymbol{\jmath}}_{t|t-1}}\underline{\boldsymbol{K}}^{\top}\underline{\boldsymbol{\Sigma}}^{-1}_{\vec{\boldsymbol{r}}_{\vec{\boldsymbol{y}}_t}} \tag{2.32}$$

Next, we predict the current density state error from the predicted measurement error using the Kalman gain matrix as follows:

$$\vec{\boldsymbol{r}}_{\vec{\boldsymbol{\jmath}}_t} = \underline{\boldsymbol{G}}_t \vec{\boldsymbol{r}}_{\vec{\boldsymbol{y}}_t} \tag{2.33}$$

Similarly, we estimate the filtered state $\vec{\boldsymbol{\jmath}}_{t|t}$ using the following equation:

$$\vec{\boldsymbol{\jmath}}_{t|t} = \vec{\boldsymbol{\jmath}}_{t|t-1} + \vec{\boldsymbol{r}}_{\vec{\boldsymbol{\jmath}}_t} \tag{2.34}$$

Likewise, we estimate the covariance matrix of the filtered state estimate, which has the dimensions of $(N_j \times N_j)$ as follows:

$$\underline{\boldsymbol{\Sigma}}_{\vec{\boldsymbol{\jmath}}_{t|t}} = \left(\underline{\boldsymbol{I}} - \underline{\boldsymbol{G}_t\boldsymbol{K}}\right)\underline{\boldsymbol{\Sigma}}_{\vec{\boldsymbol{\jmath}}_{t|t-1}} \tag{2.35}$$

Detailed models use a high number of voxels to describe the source space, which will lead to a big global current density vector. This makes it impractical to solve the inverse problem due to the high computational power required to estimate numerous unknown parameters. To address this issue, we adapt the Kalman filter to the Spatiotemporal Kalman filter as proposed in [Gal+04].

2.9.4 Spatiotemporal Kalman Filter (STKF)

The Kalman filter inverse problem can become computationally demanding due to high dimensionality. To overcome this limitation, we adopt a modified version of the Kalman filter known as the Spatiotemporal Kalman filter (STKF). This method was originally introduced in [Gal+04] and its mathematical equations are based on [Gal+04], [Hab14], [Ham18], and [Ste08]. The STKF model considers only direct six neighbours and uses the second-order discrete Laplacian operator to decouple the state-space at each source point, thereby keeping only the six neighbours.

To obtain a low-dimensional state-space model at each source point, we regulate the current density by calculating the average of its neighbouring voxels. We represent this modified state-space model as:

$$\tilde{\vec{\boldsymbol{j}}}_t = \underline{\boldsymbol{L}}\vec{\boldsymbol{j}}_t \tag{2.36}$$

$$\vec{\boldsymbol{y}}_t = \underline{\tilde{\boldsymbol{K}}}\tilde{\vec{\boldsymbol{j}}}_t + \vec{\boldsymbol{\epsilon}}_t \tag{2.37}$$

where $\tilde{\vec{\boldsymbol{j}}}$ is a vector with a length of N_j. These variables describe the spatial Laplacian smoothness and the direct influence of the six neighbouring source points on the current density at each voxel and time point.

The second model equation is the measurement equation (2.37). $\underline{\tilde{\boldsymbol{K}}}$ is the new laplacianised lead-field matrix, with dimensions of $N_y \times N_j$, and can be calculated by multiplying the lead-field matrix by the inverse Laplacian matrix, as follows:

$$\underline{\tilde{\boldsymbol{K}}} = \underline{\boldsymbol{K}}\underline{\boldsymbol{L}}^{-1} \tag{2.38}$$

The measurement noise vector, $\vec{\boldsymbol{\epsilon}}_t$, has a dimension of N_y and is assumed to be white Gaussian noise with a zero mean. We set σ^2_{ϵ} as the measurement noise variance and $\underline{\boldsymbol{\Sigma}}_{\vec{\boldsymbol{\epsilon}}}$ as the measurement noise covariance matrix, which can be calculated as:

$$\underline{\boldsymbol{\Sigma}}_{\vec{\boldsymbol{\epsilon}}} = \sigma^2_{\vec{\boldsymbol{\epsilon}}}\underline{\boldsymbol{I}}_{N_y} \tag{2.39}$$

where $\underline{\boldsymbol{I}}_{N_y}$ is an identity matrix with dimensions of N_y. By defining a covariance matrix with only diagonal values, we assume that the sensors' noise is completely uncorrelated. We do this for simplicity, but in fact, the MCG data channels are correlated.

The dynamical model of the state-space can be described as follows for the prediction phase:

$$\tilde{\vec{\boldsymbol{j}}}_{v,t} = \underline{\boldsymbol{A}}_L\tilde{\vec{\boldsymbol{j}}}_{v,t-1} + \underline{\boldsymbol{B}}_L\tilde{\vec{\boldsymbol{u}}}_{v,t} + \tilde{\vec{\boldsymbol{\eta}}}_{v,t} \tag{2.40}$$

where the voxels $\acute{v}$ are the nearest neighbours and part of the voxels v. $\tilde{\vec{\boldsymbol{j}}}_{v,t}$ depends on both v and t where v represents the space and t represents time. v and t do not depend on each other, therefore they are written in the v, t format.

The local transition matrix, denoted by $\underline{\boldsymbol{A}}_L$, characterizes the interdependence between the current and previous time points. It has dimensions of 3×3 since each voxel contains three value components for the Cartesian coordinate system. In contrast, the local input matrix $\underline{\boldsymbol{B}}_L$ captures the influence of neighbouring voxels.

For the first-order autoregressive model, the state dimension N_{st} is equal to three, the matrices $\underline{\boldsymbol{A}}_L$ and $\underline{\boldsymbol{B}}_L$ can be expressed as follows:

$$\underline{\boldsymbol{A}}_L = a_1 \underline{\boldsymbol{I}}_3, \quad \underline{\boldsymbol{B}}_L = b\underline{\boldsymbol{I}}_3, \tag{2.41}$$

where a_1 represents the first-order autoregressive model parameter and b is the neighbouring contribution parameter.

The local input vector, denoted by $\tilde{\vec{\boldsymbol{u}}}_{v,t}$, represents the average of the current densities of the six neighbouring voxels at the previous time point. It can be computed as follows:

$$\tilde{\vec{\boldsymbol{u}}}_{v,t} = \frac{1}{6} \sum_{\acute{v} \in N(v)} \tilde{\vec{\boldsymbol{j}}}_{\acute{v},t-1} \tag{2.42}$$

The local dynamical noise covariance is also 3×3 dimensional and can be obtained by multiplying the laplacianised dynamical noise variance with the identity matrix:

$$\underline{\boldsymbol{\Sigma}}_{\tilde{\vec{\boldsymbol{\eta}}}_L} = \sigma^2_{\tilde{\vec{\boldsymbol{\eta}}}} \underline{\boldsymbol{I}}_3 \tag{2.43}$$

The autoregressive model of order 2 (AR2) increases the state dimension to $N_{st} = 6$, and the corresponding dynamical model becomes:

$$\begin{bmatrix} \tilde{\vec{\boldsymbol{j}}}_{v,t} \\ \bar{\tilde{\vec{\boldsymbol{j}}}}_{v,t} \end{bmatrix} = \underline{\boldsymbol{A}}_L \begin{bmatrix} \tilde{\vec{\boldsymbol{j}}}_{v,t-1} \\ \bar{\tilde{\vec{\boldsymbol{j}}}}_{v,t-1} \end{bmatrix} + \underline{\boldsymbol{B}}_L \begin{bmatrix} \tilde{\vec{\boldsymbol{u}}}_{v,t} \\ \vec{\boldsymbol{0}}_3 \end{bmatrix} + \begin{bmatrix} \tilde{\vec{\boldsymbol{\eta}}}_t \\ \vec{\boldsymbol{0}}_3 \end{bmatrix}, \tag{2.44}$$

where $\vec{\boldsymbol{0}}_3$ is a vector of zeros with a length of 3.

The local state transition matrix for the AR2 model, denoted as $\underline{\boldsymbol{A}}_L$, has dimensions of 6×6. It is constructed as follows:

$$\underline{\boldsymbol{A}}_L = \begin{bmatrix} a_1 \underline{\boldsymbol{I}}_3 & a_2 \underline{\boldsymbol{I}}_3 \\ \underline{\boldsymbol{I}}_3 & \underline{\boldsymbol{0}}_3 \end{bmatrix}, \tag{2.45}$$

here, $\underline{\boldsymbol{I}}_3$ is the identity matrix of size 3×3, and $\underline{\boldsymbol{0}}_3$ is a matrix of zeros with dimensions of 3×3.

In the same manner, the local input matrix $\underline{\boldsymbol{B}}_L$ also has dimensions of 6×6 and can be constructed as follows:

$$\underline{\boldsymbol{B}}_L = \begin{bmatrix} b\underline{\boldsymbol{I}}_3 & \underline{\boldsymbol{0}}_3 \\ \underline{\boldsymbol{0}}_3 & \underline{\boldsymbol{0}}_3 \end{bmatrix} \tag{2.46}$$

The local dynamical noise covariance matrix $\underline{\boldsymbol{\Sigma}}_{\tilde{\vec{\boldsymbol{\eta}}}_L}$ can be constructed as:

$$\underline{\boldsymbol{\Sigma}}_{\tilde{\vec{\boldsymbol{\eta}}}_L} = \begin{bmatrix} \sigma^2_{\tilde{\vec{\eta}}} \underline{\boldsymbol{I}}_3 & \underline{\boldsymbol{0}}_3 \\ \underline{\boldsymbol{0}}_3 & \underline{\boldsymbol{0}}_3 \end{bmatrix} \tag{2.47}$$

The local state prediction error covariance matrix is a $N_{st} \times N_{st}$ matrix and can be obtained using the following equation:

$$\underline{\boldsymbol{\Sigma}}_{\tilde{\vec{j}}\,v,t|t-1} = \underline{\boldsymbol{A}}_L \underline{\boldsymbol{\Sigma}}_{\tilde{\vec{j}}\,v,t-1|t-1} \underline{\boldsymbol{A}}_L^\top + \underline{\boldsymbol{\Sigma}}_{\tilde{\vec{\boldsymbol{\eta}}}_L} \tag{2.48}$$

Next, we use the state prediction vector to obtain the measurement prediction vector:

$$\vec{\boldsymbol{y}}_{t|t-1} = \underline{\tilde{\boldsymbol{K}}} \tilde{\vec{\boldsymbol{j}}}_{t|t-1}, \tag{2.49}$$

where the global state prediction $\tilde{\vec{\boldsymbol{j}}}_{t|t-1}$ is obtained from the combination of the local states $\tilde{\vec{\boldsymbol{j}}}_{v,t|t-1}$ of all voxels.

Then, we calculate the measurement prediction error vector, which is the difference between the real and predicted measurement vectors. It is a $N_y \times 1$ vector and can be computed as follows:

$$\vec{\boldsymbol{r}}_{y,t} = \vec{\boldsymbol{y}}_t - \vec{\boldsymbol{y}}_{t|t-1} \tag{2.50}$$

The covariance matrix for the measurement prediction error vector has dimensions of $N_y \times N_y$ and is calculated as follows:

$$\underline{\boldsymbol{\Sigma}}_{\vec{\boldsymbol{r}}_{y,t|t-1}} = \sum_{v=1}^{N_v} \underline{\tilde{\boldsymbol{K}}}_v \underline{\boldsymbol{\Sigma}}_{\tilde{\vec{j}}\,v,t|t-1} \underline{\tilde{\boldsymbol{K}}}_v^\top + \underline{\boldsymbol{\Sigma}}_{\vec{\boldsymbol{\epsilon}}} \tag{2.51}$$

Next, we calculate the local Kalman gain matrix $\underline{\boldsymbol{G}}_{v,t}$, which has dimensions of $N_{st} \times N_y$ and is given by:

$$\underline{\boldsymbol{G}}_{v,t} = \underline{\boldsymbol{\Sigma}}_{\tilde{\vec{j}}\,v,t|t-1} \underline{\tilde{\boldsymbol{K}}}_v^\top \underline{\boldsymbol{\Sigma}}_{\vec{\boldsymbol{r}}_{y,t}}, \tag{2.52}$$

where $\underline{\tilde{\boldsymbol{K}}}_v$ is the local leadfield matrix. It is obtained from the leadfield matrix $\underline{\boldsymbol{K}}$, where only the column that corresponds to the grid point v keeps its values, and every other value is replaced by zeros. Equation (2.53) shows the structure of $\underline{\tilde{\boldsymbol{K}}}_v$.

$$\underline{\tilde{\boldsymbol{K}}}_v = \begin{bmatrix} & 0 & \cdots & 0 \\ [\underline{\boldsymbol{K}}]_v & \vdots & \ddots & \vdots \\ & 0 & \cdots & 0 \end{bmatrix} \tag{2.53}$$

The local state prediction error is obtained as the product of the Kalman gain matrix $\underline{\boldsymbol{G}}_{v,t}$ and the measurement prediction error vector $\vec{\boldsymbol{r}}_{y,t}$:

$$\vec{\boldsymbol{r}}_{\tilde{j}_{v,t}} = \underline{\boldsymbol{G}}_{v,t}\vec{\boldsymbol{r}}_{y,t} \tag{2.54}$$

The local state prediction is then corrected using the local state prediction error to obtain the local estimated state $\tilde{\vec{\boldsymbol{j}}}_{v,t|t}$, which has dimensions of $N_{st} \times 1$:

$$\tilde{\vec{\boldsymbol{j}}}_{v,t|t} = \tilde{\vec{\boldsymbol{j}}}_{v,t|t-1} + \vec{\boldsymbol{r}}_{\tilde{j}_{v,t}} \tag{2.55}$$

The local state estimation error covariance matrix, which has dimensions of $N_{st} \times N_{st}$, is calculated as:

$$\underline{\boldsymbol{\Sigma}}_{\tilde{j}_{v,t|t}} = \left(\underline{\boldsymbol{I}}_{N_{st}} - \underline{\boldsymbol{G}}_{v,t}\underline{\tilde{\boldsymbol{K}}}_{v}\right)\underline{\boldsymbol{\Sigma}}_{\tilde{j}_{v,t|t-1}} \tag{2.56}$$

Finally, the local state estimation vector and the local error covariance matrix are converted back from the weakly-coupled state-space into the original state-space using the following equations (2.57) and (2.58)

$$\vec{\boldsymbol{j}}_{t} = \underline{\boldsymbol{L}}^{-1}\tilde{\vec{\boldsymbol{j}}}_{t} \tag{2.57}$$

$$\underline{\boldsymbol{\Sigma}}_{j_{t|t}} = \underline{\boldsymbol{L}}^{-1}\underline{\boldsymbol{\Sigma}}_{\tilde{j}_{t|t}}\underline{\boldsymbol{L}}^{-1^{\top}} \tag{2.58}$$

While the Kalman filter is the appropriate inverse problem instrument for estimating the unobservable state, it comes with challenges due to the propagation of large covariance matrices and the significant number of undetermined parameters that need to be estimated. This is why there are not many applications using the Kalman filter. However, we can significantly reduce the number of parameters by assuming that our model is homogeneous and that the parameters are constant with time. We can then use maximum likelihood to estimate the remaining parameters.

2.9.5 State-space Parameter Estimation Using Maximum Likelihood (ML)

To utilize the STKF, it is necessary to estimate the next state and error covariance matrices for both the dynamical and measurement errors. To achieve this, the parameter matrices of the state-space need to be optimized first. For the STKF, the Akaike information criterion (AIC) is utilized. By minimizing the AIC value, the best possible fit is found through using the maximum likelihood (ML) method[Gal+04].

The AIC method is an optimization technique that evaluates a model's fit for single or multiple datasets. From experience, the AIC values are typically negative for our application although it does not need to be, with lower values indicating a better fit of the parameters to the dataset. AIC is specialized to penalize having more parameters by adding a term that increases the AIC value for using more parameters in the model. AIC can be seen as a quantification of the distance between an estimated model and a perfect model that cannot be exactly estimated. By optimizing different sets of parameters, we try to find a model that is as close as possible to the true model. Mathematically, the AIC method can be described as follows:

$$\mathrm{AIC}\left(\vec{\boldsymbol{\theta}}_{KF}\right) = -2\mathcal{L}\left(\vec{\boldsymbol{\theta}}_{KF}\right) + 2N_{KF}, \tag{2.59}$$

Here, $\vec{\boldsymbol{\theta}}_{KF}$ is a vector containing the set of parameters for the state-space model to be optimized. $\mathcal{L}\left(\vec{\boldsymbol{\theta}}_{KF}\right)$ is the log-likelihood for the data measurements calculated using the parameter set $\vec{\boldsymbol{\theta}}_{KF}$. N_{KF} is the dimension of the parameter vector $\vec{\boldsymbol{\theta}}_{KF}$.

We use the following parameter vector for the first-order autoregressive model:

$$\vec{\boldsymbol{\theta}}_{STKF,AR(1)} = \left[a_1, b, \sigma_{\vec{\boldsymbol{\eta}}}^2, \sigma_{\vec{\boldsymbol{\epsilon}}}^2\right]^\top \tag{2.60}$$

And for the second-order autoregressive model:

$$\vec{\boldsymbol{\theta}}_{STKF,AR(2)} = \left[a_1, a_2, b, \sigma_{\vec{\boldsymbol{\eta}}}^2, \sigma_{\vec{\boldsymbol{\epsilon}}}^2\right]^\top \tag{2.61}$$

To evaluate the AIC, we use the STKF with the following equation:

$$\mathrm{AIC}\left(\vec{\boldsymbol{\theta}}_{KF}\right) = -2\sum_{t=1}^{T}(\log\left|\underline{\boldsymbol{\Sigma}}_{\vec{r}_{y,t}}\right| + \vec{\boldsymbol{r}}_{y,t}{}^\top \underline{\boldsymbol{\Sigma}}_{\vec{r}_{y,t}}{}^{-1}\vec{\boldsymbol{r}}_{y,t}) + TN_y\log(2\pi) + 2N_{KF}, \tag{2.62}$$

Here, T is the number of time points in the data measurement segment used. The optimisation process for the STKF can be time consuming. We usually call the STKF around 50 times to optimise a time series of 32 channel and 400 - 500 time points. This data set takes around two days of computation on a single core of a computer with an Intel(R) Xeon(R) E5-2640 v3 CPU processor running at a maximum speed of 2.60GHz. Our model is not complicated and has low resolution, but using a more descriptive model that has better source space resolution, more sensors, and longer time series can significantly increase the calculation complexity. In comparison, the results calculated with the LORETA method take around one minute on the same system setup.

We used three optimisation algorithms to minimise the AIC. The first method is the Broyden-Fletcher-Goldfarb-Shanno (BFGS) method, which relies on the quasi-Newton approach. We used the MATLAB's Optimization Toolbox implementation for this method.

The second method is the Nelder-Mead simplex algorithm, we used it in the MATLAB's standard function (fminsearch). We used the BFGS method alone or an iteration of the BFGS and the Nelder-Mead simplex methods for optimisation [Gal+04] [Ste08] [Gal+08].

Additionally, we used a simplistic stochastic optimisation method. The parameter values in this method are changed by a certain amount of Gaussian noise with a certain standard deviation. In every iteration, we only accept the parameter values if they make the AIC value lower than the previous parameters to ensure improvement throughout the optimisation process [Gal+08].

2.9.6 New Laplacian Definition

The classical Laplacian definition for LORETA and STKF considers only six neighbours for every source voxel point. The first implementation of the classical definition on LORETA in [PMML94] was not used to avoid the inversion of highly dimensional matrices. Instead, we used the implementation in [PM99], which derives equations to estimate the current density $\vec{\boldsymbol{j}}$.

By assuming that the measurements are noise-free and therefore $\vec{\boldsymbol{y}}_t = \underline{\boldsymbol{K}}\vec{\boldsymbol{j}}_t$, the cost function of the solution can be represented as in equation (2.63).

$\vec{\boldsymbol{y}}_t = \underline{\boldsymbol{K}}\vec{\boldsymbol{j}}_t$ can be written as $\underline{\boldsymbol{Y}} = \underline{\boldsymbol{KJ}}$, where $\underline{\boldsymbol{Y}}$ is the three-vectors matrix of $\vec{\boldsymbol{y}}_t$, and each vector has the x, y, and z Cartesian components. In the same way, $\underline{\boldsymbol{J}}$ is the matrix version of $\vec{\boldsymbol{j}}_t$.

$$\min_{\underline{\boldsymbol{J}}} \|\underline{\boldsymbol{BWJ}}\|^2 , \tag{2.63}$$

where $\underline{\boldsymbol{W}} = \Omega \otimes \underline{\boldsymbol{I}}$ and has the dimensions of $3N_j \times 3N_j$, $\otimes$ is Kronecker product, and $\underline{\boldsymbol{I}}$ is an identity matrix of 3×3. $\Omega_{ii} = \sqrt{\sum_{\alpha=1}^{N_y} k_{\alpha i}^\top k_{\alpha i}}$, where $\underline{\boldsymbol{K}}$ is the leadfield matrix with $k_{\alpha i}$ is the i-th row. $\underline{\boldsymbol{B}}$ is the discrete Laplacian operator that has the dimensions of $3N_j \times 3N_j$. Now, let $\underline{\boldsymbol{Z}} = \underline{\boldsymbol{WJ}} = (z_1^\top, z_2^\top, ..., z_{N_j}^\top)$, where z_i is 3 vectors and represents the weighted current density. Let us assume $\underline{\boldsymbol{L}} = \underline{\boldsymbol{BZ}} = (l_1^\top, l_2^\top, ..., l_{N_j}^\top)$, where L is the Laplacian matrix. [PM95]

In the study of the heart, a regular and homogeneous distribution of source grid points is required. In this setup, neighbouring grid points have a distance of d from each other. The classical definition of the Laplacian matrix, introduced in [PMML94], has been used in some of our calculations. The Laplacian matrix can be calculated as shown in equation (2.64):

$$l_i = \frac{6}{d^2}\left(\frac{\sum_n z_n}{6} - z_i\right), \text{ under restriction of } \|r_i - r_n\| = d \tag{2.64}$$

Here, r_i and r_n represent the locations of the grid points in the heart and its neighbouring points, respectively. n represents the number of neighbouring voxels. However, for boundary grid points, this definition is not adequate, since they have fewer neighbours.

Dividing the sum of neighbouring grid point activities by 6, as in equation (2.64), overestimates the current density at the boundary points. To address this, a new definition can be introduced as shown in equation (2.65):

$$l_i = \frac{6}{d^2}\left(\frac{\sum\limits_n z_n}{\sum\limits_n 1} - z_i\right), \text{ under restriction of } \|r_i - r_n\| = d \tag{2.65}$$

The definitions in (2.64) and (2.65) have no difference for the non-borders grid points. However, the Laplacian operator $\underline{\boldsymbol{B}}$ in equation (2.65) is singular for some grid points. To solve this, we combine the definitions in equations (2.64) and (2.65) to create a new definition that is non-singular and does not force the activities to be zero at the boundaries. The new definition is expressed as shown in equation (2.66):

$$l_i = \frac{6}{d^2}\left(\frac{\left(6 + \sum\limits_n 1\right)}{12\sum\limits_n 1}\sum_n z_n - z_i\right), \text{ under restriction of } \|r_i - r_n\| = d \tag{2.66}$$

Overall, this new definition provides a non-singular Laplacian operator and accurately represents the current density at the boundary points. [PM95]

2.9.7 State-space Generalized Autoregressive Conditional Heteroskedasticity Spatiotemporal Kalman Filter (ssGARCH-STKF)

The ssGARCH-STKF algorithm represents a more sophisticated variant of the Kalman filter. While we have used the AR1 and AR2 models with the Kalman filter in part (2.9.3), the ssGARCH model has become a valuable tool for estimating unobserved data states in econometrics and other fields. For example, one of its early applications was to estimate the means and variances of inflation in the UK during the turbulent financial times of the 1970s. The ssGARCH model has since been applied in fields such as oceanography, quantum scattering, and microstructure analysis. We are applying the ssGARCH-STKF algorithm for the first time to MCG data [Eng82].

Although the Spatiotemporal Kalman filter is a manageable solution regarding the number of parameters and the ability to optimize them with time and computational power, the assumptions in many situations are unsuitable for the physics of the data or the system. In particular, the noise covariance matrix approximations that drive the dynamics in the spatiotemporal dynamical model are problematic. To address this issue, we use ssGARCH for the covariance model in combination with the Kalman filter. This new solution generalizes the Kalman filter, and the covariance matrices are a key component. This is a crucial modification to our implementation of the Kalman filter in part (2.9.3) [GYO04].

To use the Kalman filter, we need to estimate the parameters a_1, a_2, b, σ_{ϵ}^2, and σ_{η}^2 using likelihood maximization as explained in (2.9.4). This is technically feasible because we assume that the parameter values are fixed despite the changing time and local position due to the stationarity and homogeneity assumptions. If we consider a more realistic scenario by letting go of those assumptions, then we will have a huge number of parameters at each time point and each grid. Estimating such a large number of parameters is significantly more challenging due to the huge amount of calculation power required for the parameter estimation.

Alternatively, we use a dynamical noise variance σ_{η}^2 in the local state, making it dependent on the location and time. The new dynamical noise variance can be defined as:

$$\xi_{v,t} = \left(j_{v,t}, j_{v,t-1}, \sigma_{\eta v,t}^2\right) \tag{2.67}$$

We know from experience that the choice of the dynamical noise variance σ_{η}^2 is critical for the Kalman filter, while the other parameters of $a1$, a_2, b, σ_{ϵ}^2 are less censorious. The $\sigma_{\eta v,t}^2$ dynamics can be modelled back by a stochastic autoregressive model.

The main intention of using the ssGARCH model is to use the prediction error that we get from the previous time point as an estimate of the stochastic driving dynamics of the time-dependent covariance. We have the observation prediction error in the sensor space, but we do not have the dynamical prediction error in the source local space directly. Therefore, we propagate the information carried in the observation prediction errors back to the state-space by using the Kalman gain, which means using the relevant value of the observation prediction error of the previous time point multiplied by the Kalman gain $\underline{\boldsymbol{G}}_{v,t-1}\vec{\boldsymbol{r}}_{\vec{\boldsymbol{y}}_{t-1}}$ instead of the dynamical prediction error [GYO04].

This is the basic idea of forming the GARCH in the state-space model. The GARCH dynamics can be based on different variants possibilities; we choose the dynamics to be based on logarithms as given below:

$$\sigma_{\eta v,t}^2 = \sigma_c^2 + \beta\sigma_{\eta v,t-1}^2 + \gamma \sum_{i=1}^{N_v} \left[\underline{\boldsymbol{G}}_{v,t-1}\vec{\boldsymbol{r}}_{\vec{\boldsymbol{y}}_{t-1}}\right]_i^2 , \tag{2.68}$$

the last term in the equation (2.68) is the simplest possibility to modify the state dynamics to a scalar covariance dynamics. The equation (2.68) is inserted in the Kalman filter after the equation (2.52). This will generate a new value for $\sigma_{\eta v,t}^2$ every time point and for every source point of v.

Chapter 3

Pipeline for Solving the Forward and Inverse Problems of the Heart

Research on the forward and inverse problems of the heart is still in its early stages compared to the brain research. In analysing EEG and MEG recordings, the Spatiotemporal Kalman filter (STKF) has been used for some time, and there are several software options available, some of which are commercial, that can read brain data, perform segmentation, meshing, sensor alignment, and solve the forward problem. However, for the heart, there are limited options for performing these same tasks. Therefore, it was essential to develop a pipeline for working with heart data.

The pipeline involves writing scripts for performing various tasks or transforming data and using a general-purpose software to perform specific tasks. As shown in figure (3.1), to use the pipeline, we require three types of data. The first type comes from electrical or magnetic sensors, either MCG, ECG, or both combined. The second type is the location of the sensors, which is obtained by triangulating a three-pod device. The third type is MRI data, which we use to build the torso geometry to solve the forward problem and calculate the lead-field matrix. The pipeline outputs the location and strength of the source activity, which we interpolate over the MRI images, making it easy for specialists to diagnose normal or abnormal heart activity.

In this chapter, we will discuss the pipeline in the sequence of data processing. We will begin with data acquisition in section (3.1) and move on to the processes for building a torso-heart model from MRI data in section (3.2). In section (3.3), we will demonstrate how we combine data from the torso-heart model, sensor locations, and MCG data to solve the forward problem. We will then discuss the calculation of the lead-field matrix in section (3.4).

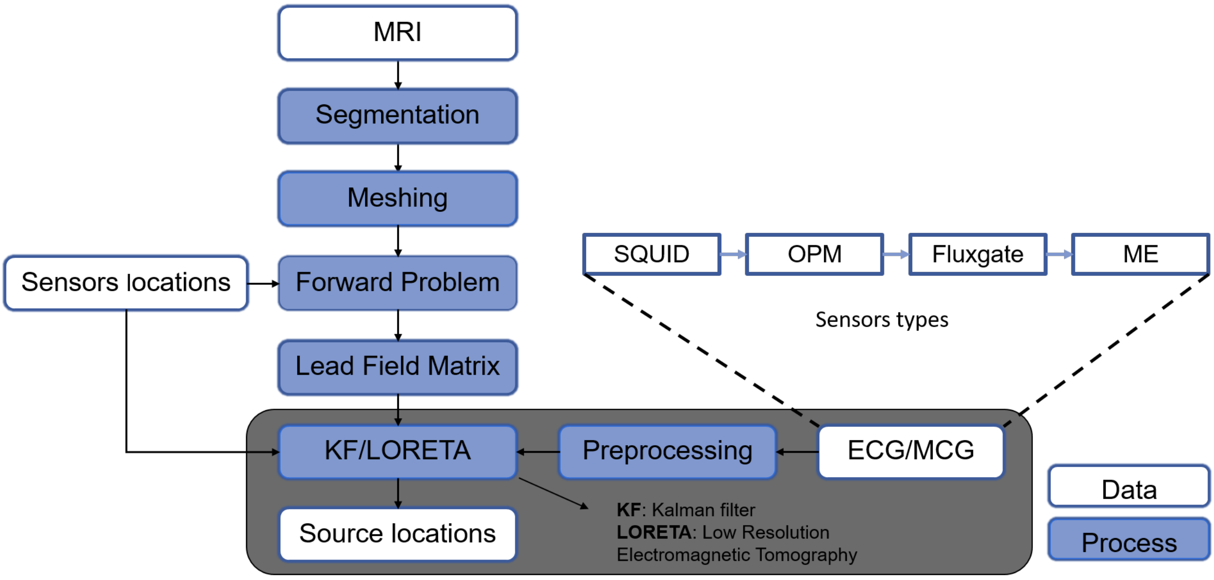

Figure 3.1: Illustration of the stages of the forward problem and how it interacts with the inverse problems and data. The white blocks represent data; input data consists of MRI, measurement data, and sensor locations. The output is localized current densities. Blue blocks represent the processes applied to the data. The shaded area represents the inverse problem.

3.1 Data Acquisition

The data acquisition process was divided into two parts. The first part was carried out at the Physikalisch - Technische Bundesanstalt in Berlin (PTB Berlin), where we obtained the MCG and ECG recordings along with the sensor locations. These recordings were crucial for solving the forward and inverse problems of the heart. The second part of the data acquisition was conducted at the Universitätsklinikum Schleswig-Holstein (UKSH) in Kiel to obtain the MRI images. The MRI images were used to build the torso geometry, which was an essential step in solving the forward problem and calculating the lead-field matrix.

3.1.1 Simultaneously Recorded MCG-ECG Dataset at the PTB Berlin

In this study, we collected simultaneous MCG-ECG datasets from three sessions. The first session involved recording data from Superconducting Quantum Interference Device (SQUID) and electrodes, as shown in figure (3.5 a.) The second session involved recording data from Optically Pumped Magnetometers (OPM) and electrodes. For the third session, we used the same OPM sensors but repositioned them to achieve a double number of sensors, which allowed us to superimpose the data for further analysis. Figure (3.5 b) shows an example of sessions two and three. We repeated these three sessions with three volunteer subjects in the Berlin Magnetically Shielded Room-2 (BMSR-2), a seven-layered shielded room. The shielded room is covered with an extra layer of active shielding, as shown in figure (3.2).

Figure 3.2: The MCG measurement room in PTB Berlin facility. a. The gate of the shielded room. b. The space outside the shielded room and the active shielding surrounding it. c. The active shielding layer from outside.

.

The SQUID system has a total of 304 channels, distributed across 19 modules, with each module containing four levels and 16 SQUIDs oriented in different directions. There are six SQUIDs that detect the magnetic field in the normal direction (upward and downward), while the remaining 10 SQUIDs detect the field in the other perpendicular directions, as shown in figure (3.3). The SQUID system is cooled with liquid helium to the temperature of almost absolute zero (-273°C).

We obtained MCG-SQUID data in the range of 60 picotesla peak-to-peak, as shown in figure (3.4). As an example, we show MCG signals for 2 seconds from 52 SQUIDs in the bottom layer oriented in the z-direction, with each module having three SQUIDs per module, except for five SQUIDs that were not functioning.

The ECG system comprised 32 electrodes distributed across the torso, capturing signals from all directions. Of these electrodes, 25 were primarily focused on the front and left side of the torso, where the heart is located, while 7 were positioned on the back. The distribution of the electrodes is depicted in figures (3.5 c) and (3.5 d.)

Simultaneous recordings were obtained from the SQUID and electrode systems figure (3.5 a) as well as from the OPM and electrode systems figure (3.5 b.). Overall, this

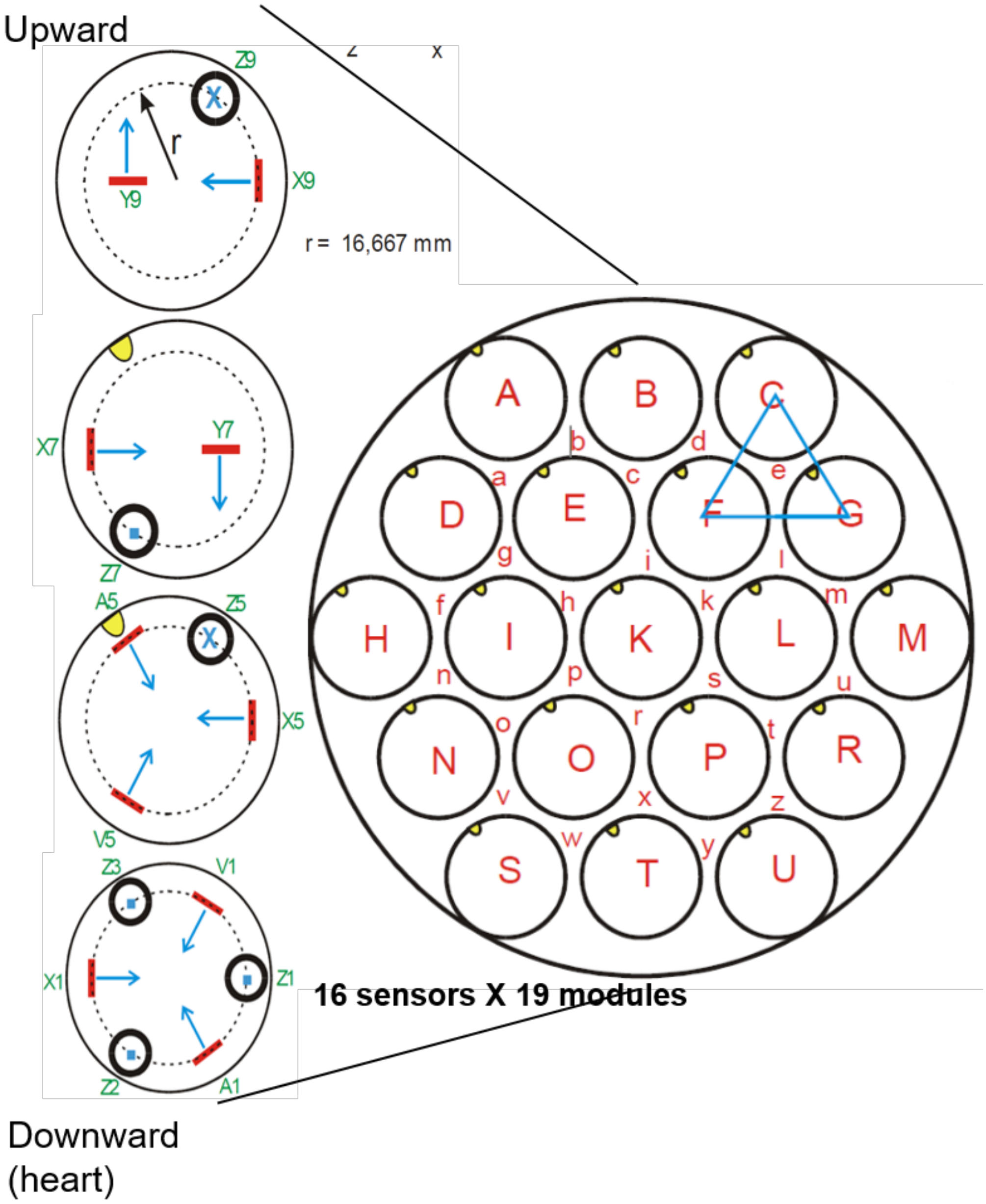

Figure 3.3: The diagram shows a schematic representation of an MCG SQUID tube, consisting of 19 modular units as represented by the large circle on the right. The tube comprises of four distinct layers of sensors, with the distribution of these sensors among the layers detailed on the left. Specifically, the 16 sensors are distributed among four levels within each of the 19 modules. The labels for the tube modules are written in upper-case and denoted in red, while the labels for the sensors are in green. Additionally, the direction of the arrows is indicated in blue, with the use of circled dots and circled Xs. The circled dots indicate a direction towards the viewer, while the circled Xs indicate a direction away from the viewer.

.

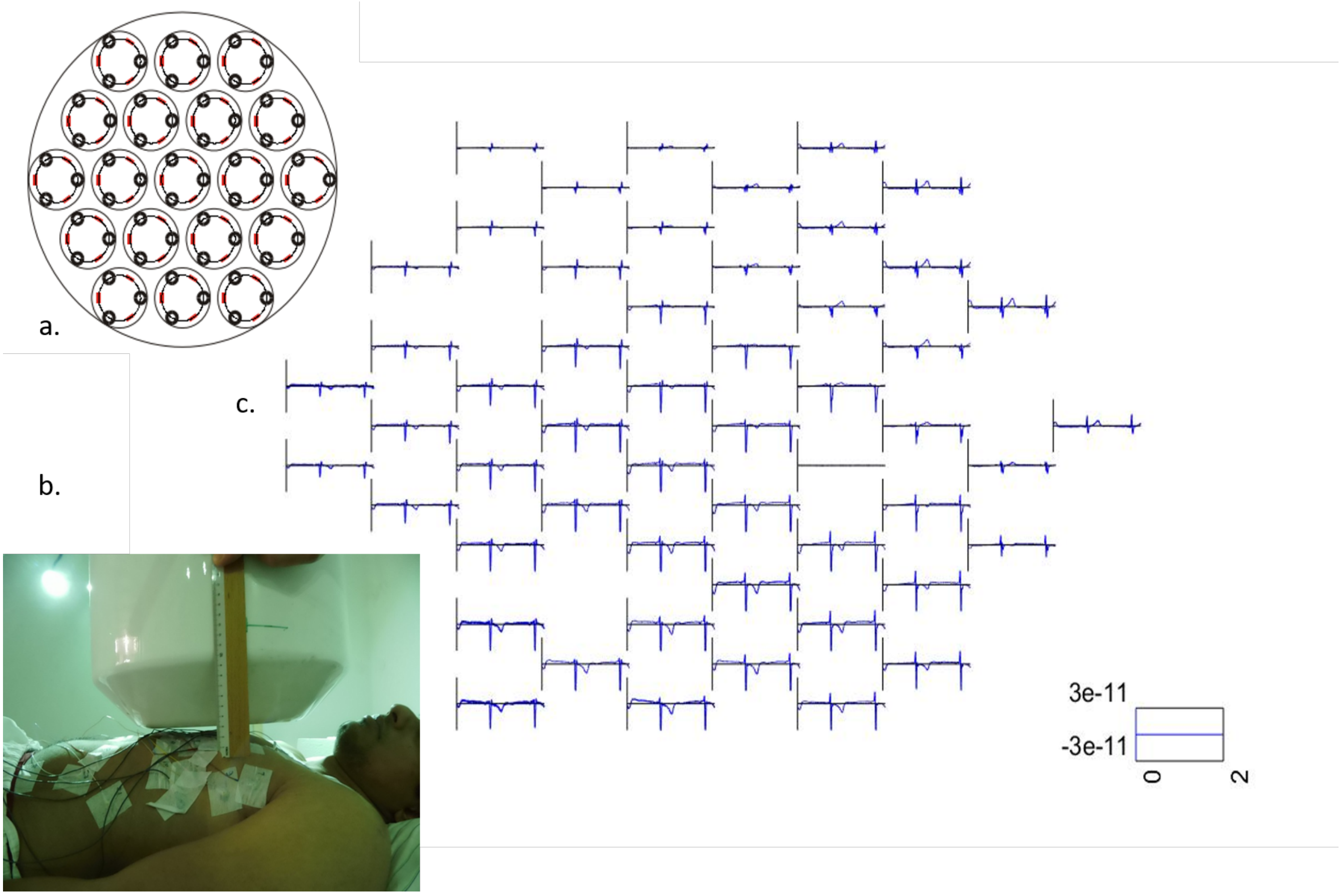

Figure 3.4: The obtained MCG measurements were mapped to the specific sensor locations in the lowermost layer of the MCG tube. a. The lowermost layer of the SQUID array. b. The SQUID tube, located within a shielded room at the Physikalisch-Technische Bundesanstalt (PTB) in Berlin. c. The measured MCG in the z-direction for the lowermost layer of the SQUID tube, where the values are in Tesla.

configuration enabled comprehensive monitoring of cardiac activity, with the MCG sensors and ECG electrodes providing a broad spatial coverage of the torso.

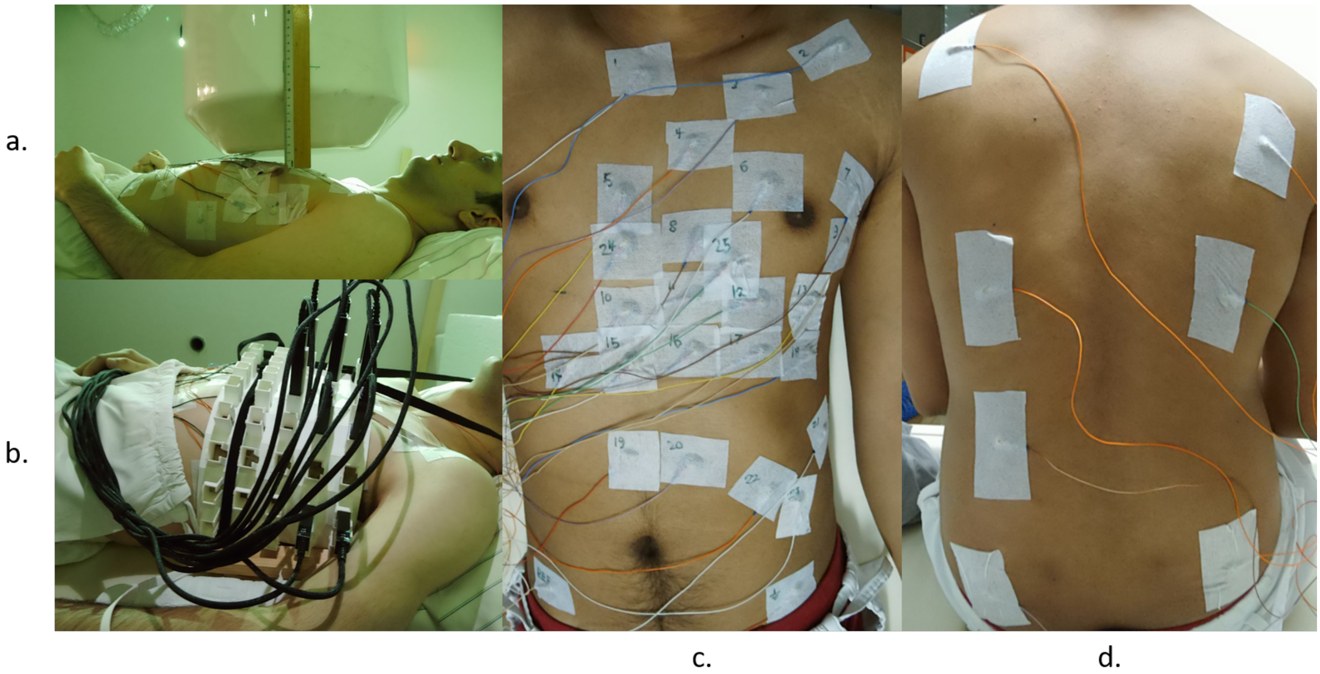

Figure 3.5: The arrangement of MCG, ECG and OPM sensors on volunteer participants. a. Simultaneous recordings obtained from the SQUID and electrode systems. b. Simultaneous recordings obtained from the OPM and electrode systems. c. An illustration of the distribution of electrodes as viewed from the front. d. The arrangement of electrodes on the posterior side.

The OPM system used in this study consisted of 10 sensors, each equipped with 2 channels of detection - one sensitive to the measured direction and the other perpendicular to it. The OPM devices were designed to work at room temperature and warm up to around 40 °C.

The OPMs were placed on a holder that was designed virtually with computer software and printed using a 3D printer, as shown in figure (3.6 a.-c.) The holder's channels were sized to precisely fit the OPMs, allowing for accurate measurement of the OPMs' locations. In the second session, the OPMs were placed in the holder as shown in figure (3.6 d.), while in the third session, their locations were shifted by one position to the right.

Figure (3.7) presents an example of the OPM recordings obtained in this study, with the corresponding sensor positions indicated and the z and y directions of each sensor. The amplitude of the signals recorded by the OPMs was in the range of 60 picotesla peak-to-peak.

In comparison to the MCG system, the OPM system offers more spatial spread and greater flexibility in terms of sensor placement. Additionally, it can work at room temperature, making it operationally cheaper without the need to cool it with helium.

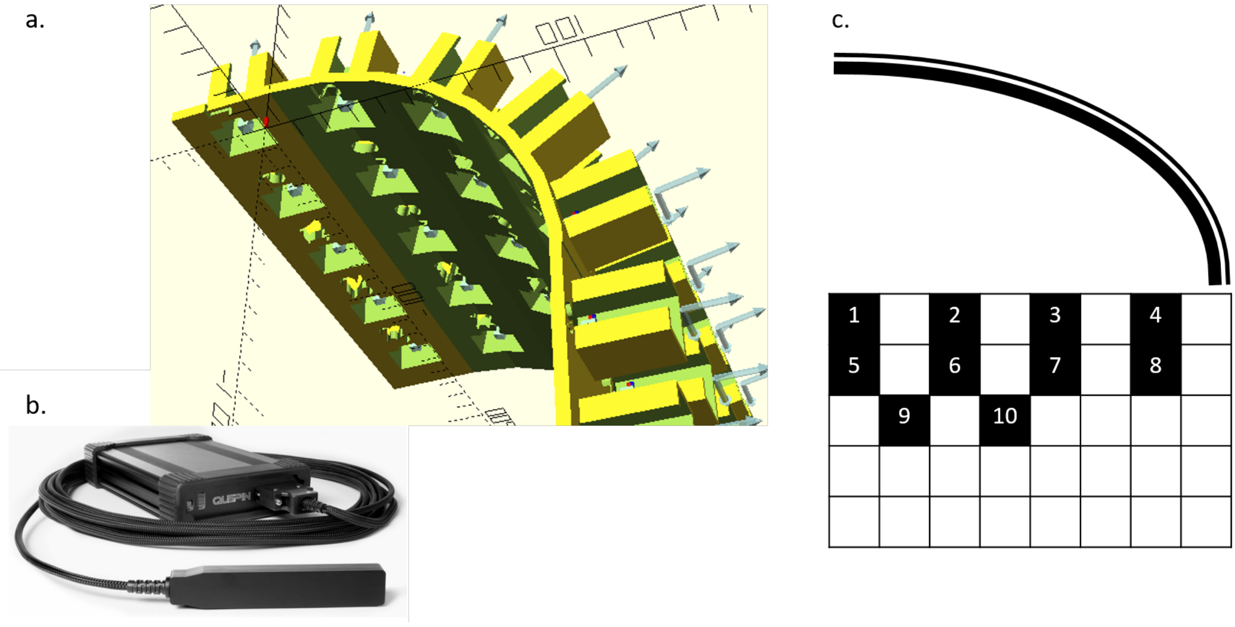

Figure 3.6: The design and components of the OPM system
a. The OPM holder was designed using computer-aided design software.
b. The OPM devices
c. The positioning of the OPM sensors in relation to the OPM holder.

The localisation of the sensors on the torso was achieved using a 3-pod ultrasonic device from zebris Medical GmbH. This device works by placing an electronic stick on the electrode locations, and upon pressing a button, the stick communicates with the 3-pods through ultrasonic waves to estimate the location of the stick tip. The estimated location should correspond to the position of the sensor at the moment of the button press. This method allows for precise and accurate localisation of the sensors on the torso.

3.1.2 MCG Recordings at the University Hospital of Charité

In this section, we discuss MCG recordings made by Dr. Henning Ahrens during a previous funding period of our project. We utilized this dataset for our inverse problem calculation and also used the sensor layout to generate simulated datasets. The recording was made using a 64-channel MCG system called CS-MAG, manufactured by the company Biomagnetik Park [Bio]. The system uses gradiometer SQUIDs with a circular plane array, which is cooled by fluid helium in a cylindrical dewar. The system is located in a shielded room at the University Hospital of Charité. The SQUID system and the array distribution are shown in figure (3.8).

It is important to note that this recording only captured MCG signals and did not include MRI recordings or a torso model for the same individual. Therefore, in the original study [Ahr15], a standard model was used. However, we used an individual torso model that we segmented from an MRI dataset instead. This MRI dataset was obtained by Prof. Koch et al. in 2011 [Koc+11], and we fitted the sensor array on the segmented

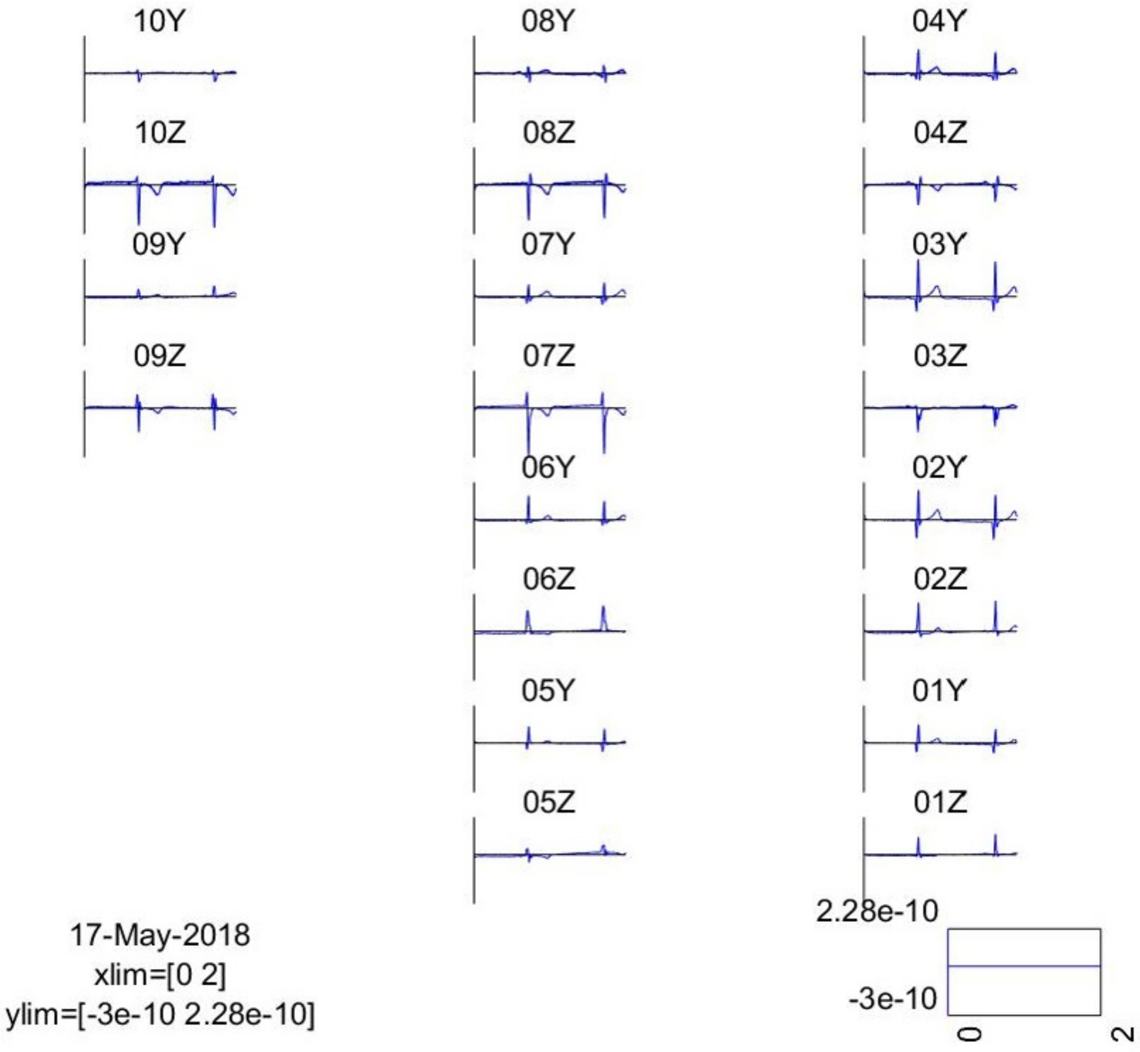

Figure 3.7: A representative sample of one session of OPM recordings is presented, with the corresponding sensor positions indicated. The OPM instrumentation utilized comprises of 10 devices, each equipped with two channels, one for measurement in the z-direction and the other for measurement in the y-direction.

.

torso model. For simulated data, this assumption is reasonable since we use the same sensor array and torso model to solve both forward and inverse problems. However, for recorded data, it is better to use the MCG and torso model for the same individual to achieve better localisation.

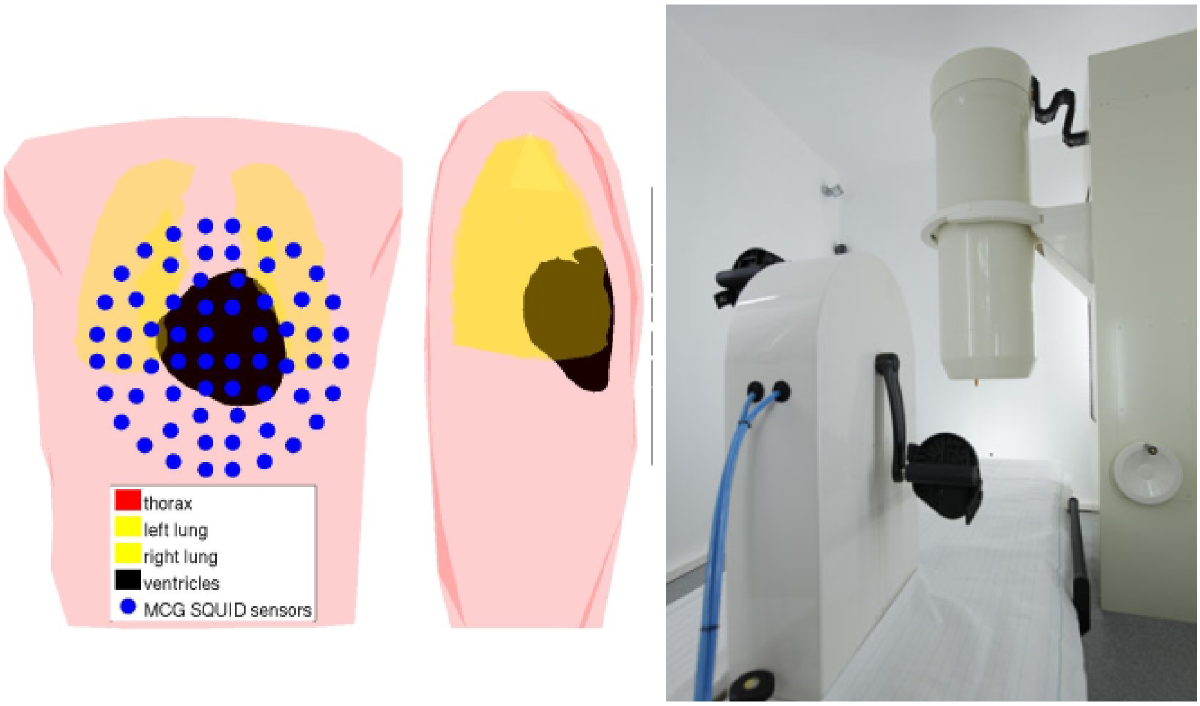

Figure 3.8: The CS-MAG system at the University Hospital of Charité using a torso model. The left side illustrates a segmented torso model of a healthy young male, obtained from the ECGSIM software [Ecg]. The model has been segmented into three regions: the heart, lungs, and the remaining torso. Additionally, the figure depicts the SQUID sensor array from the CS-MAG system placed on the torso model. On the right side, the CS-MAG system from Biomagnetik Park GmbH [Bio] at the University Hospital of Charité is shown. [Ahr15]

3.1.3 MRI Recordings at UKSH Kiel

The MRI recordings were conducted at the clinic for Radiology and Neurology in the Universitätsklinikum Schleswig-Holstein (UKSH) in Kiel using a Siemens 1.5 Tesla machine. The voxel resolution of the scans was 1.5 mm x 1.5 mm x 4.5 mm, and the scanning mode was three-dimensional. The MRI was performed on three male volunteers with no history of heart disease, and each scan lasted approximately 30 minutes. However, despite our efforts to reduce the scan time, the resulting MRI quality was not sufficient to create a high-quality multiple regions layers model.

The MRI images are coded in grayscale, with each unit element called a voxel instead of a pixel for two-dimensional images. Each voxel has a value of 8-bits, representing a number between 0 and 255 in decimal. Each number corresponds to a color on a grayscale, where 0 represents black and 255 represents white.

The scanning time was long primarily due to three reasons. First, the scanner was triggered by the ECG system to scan in phase between the T- and P-wave of the next heartbeat, as this is the most static phase in the heartbeat. This means that there is less time available for capturing data, and the device pauses for the period outside the T- to P-wave.

The second reason is that the scanner detected the breathing activity of the volunteers to choose a period of time after exhaling when the lungs are more static. This further limits the active time of recording, as it is now actively recording only when there is an exhale and in phase with the T-wave to P-wave at the same time.

The third reason is that the MRI is three-dimensional, unlike the two-dimensional MRI that is routinely used in hospitals and sufficient for medical inspection. We need a three-dimensional MRI for segmentation, but this also means that we need to capture a larger amount of data and eventually also increase the recoding time.

Figure (3.9) shows MRI slides for the first volunteer. Figure (3.10) shows MRI slides for the second volunteer and figure (3.11) shows MRI slides for the third volunteer. The distance between each layer of the MRI in the figures (3.9), (3.10) and (3.11) was rescaled to 10.5 mm to enable show here.

Figures (3.9), (3.10), and (3.11) show the axial view of the MRI scans for the first, second, and third volunteer, respectively. The distance between each layer of the MRI in the figures was rescaled to 10.5 mm for clarity, as the original resolution distance was 1.5 mm.

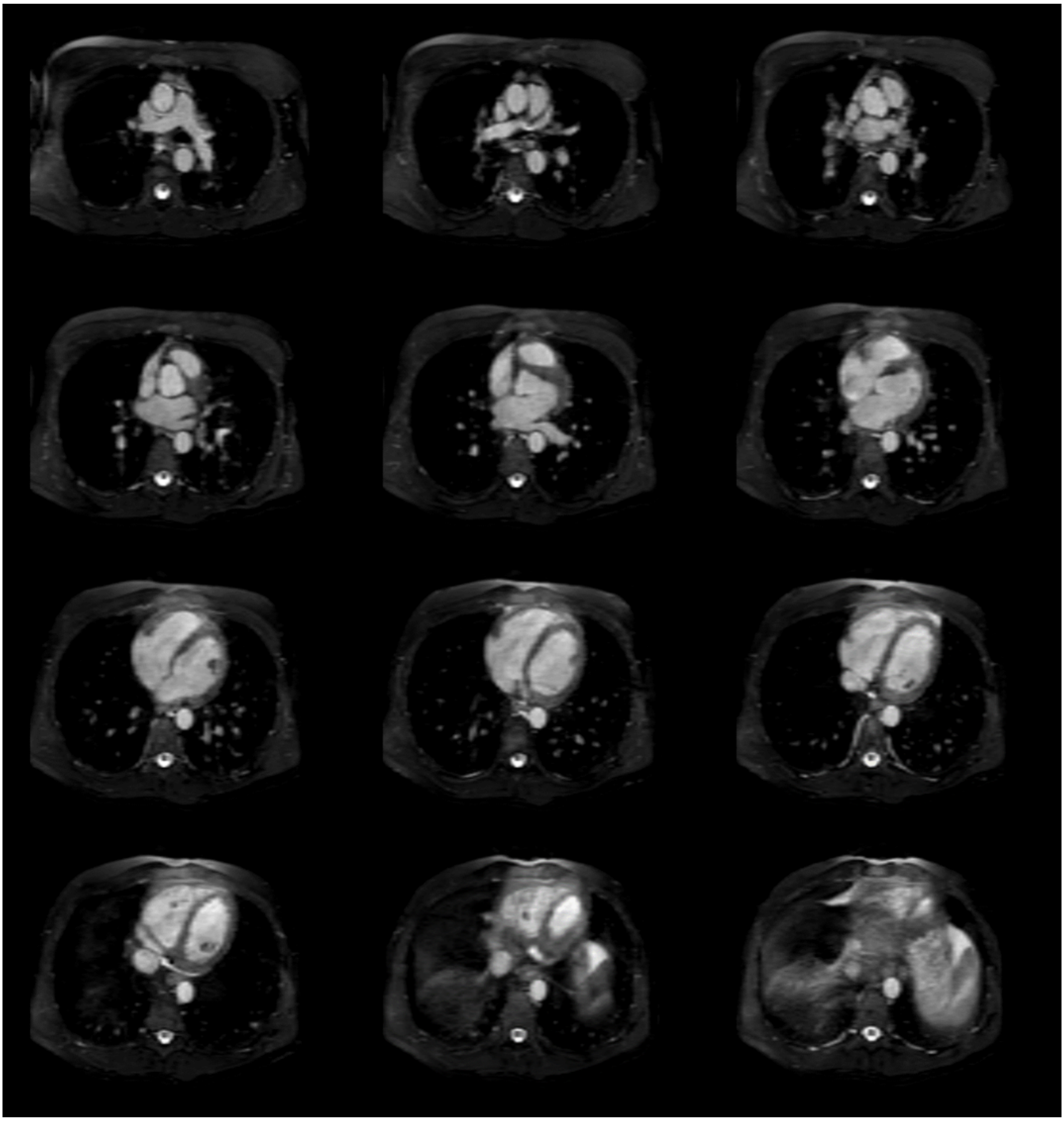

Figure 3.9: The axial view for the MRI of the first volunteer. Each picture represents one axial layer of the MRI, the distance between the axial layers is 10.5 mm and the original resolution distance is 1.5 mm

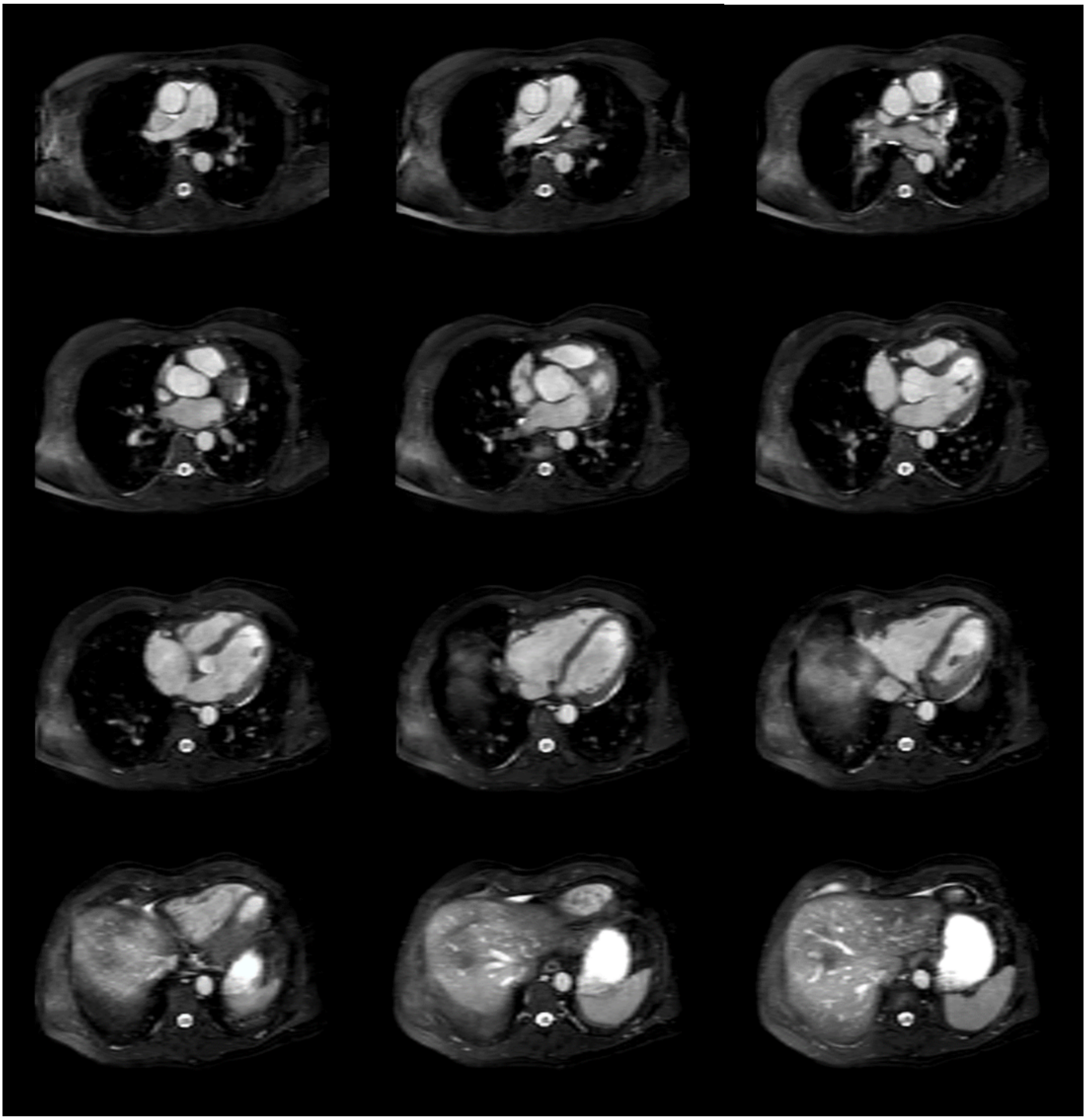

Figure 3.10: The axial view for the MRI of the second volunteer. Each picture represents one axial layer of the MRI, the distance between the axial layers is 10.5 mm and the original resolution distance is 1.5 mm

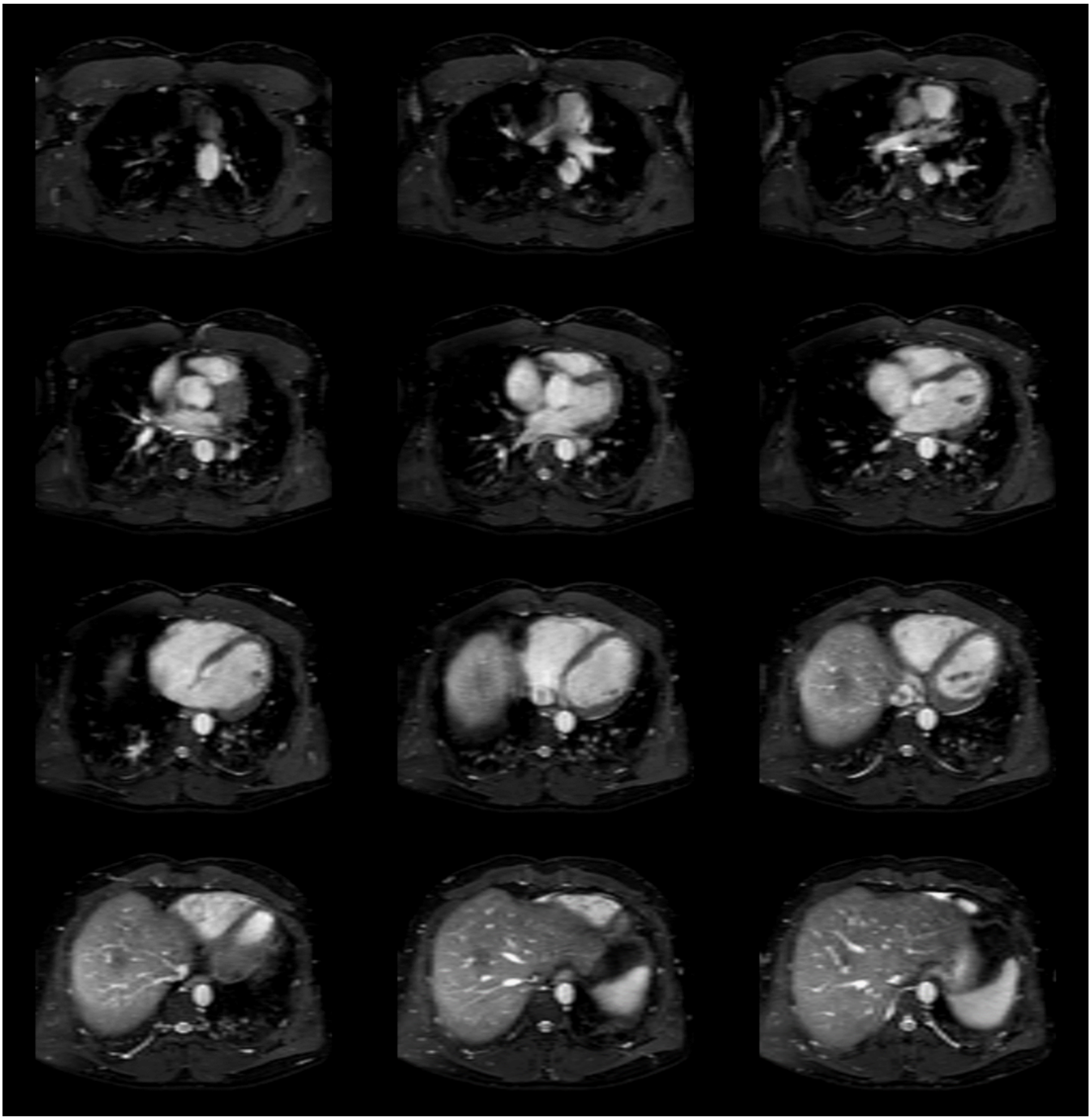

Figure 3.11: The axial view for the MRI of the third volunteer. Each picture represents one axial layer of the MRI, the distance between the axial layers is 10.5 mm and the original resolution distance is 1.5 mm

3.2 Anatomical Models Using MRI

The main objective of acquiring MRI images is to identify the torso organs and classify them according to their tissue's electrical characteristics to create realistic torso-heart models. By creating a realistic model, we can solve the forward problem with higher accuracy, and eventually, the inverse problem's source locations will be better estimated.

In this study, we constructed two torso-heart models. The first model was built using high-resolution MRI series 701 from [Koc+11], which shows the heart at diastole, as depicted in figure (3.13). The second model was constructed using MRI data obtained from UKSH Kiel, as described in section (3.1.3), and is shown in figure (3.14). The segmentation and meshing procedures used for both models were almost identical.

3.2.1 MRI Segmentation

For the first model, we utilized a high-resolution MRI series 701 from [Koc+11] to segment two spheres: the torso and the heart, as shown in figure (3.12). Although there is automated segmentation software available for the brain field, no such software is available for the heart. Therefore, we performed manual segmentation by manually marking the borders of the torso and the heart on all MRI slices. We generated three-dimensional surface meshes that represent the torso and the heart using Seg3D, a free and open source software developed by the NIH Centre for Integrative Biomedical Computing, Scientific Computing and Imaging (SCI) Institute at the University of Utah [CIB16]. The segmentation result, which is a triangular surface mesh, is shown in figure (3.13). We assigned conductivities of 0.6 S/m for the heart and 0.2 S/m for the rest of the torso in this model.

For the second model, we used ITK-SNAP, a free and open-source semi-automatic segmentation software developed by a long-term collaboration between Penn Image Computing and Science Laboratory (PICSL), University of Pennsylvania and the Scientific Computing and Imaging Institute (SCI), University of Utah [Yus+06]. ITK-SNAP offers advanced segmentation tools such as active contour methods, thresholding, classification, clustering, and edge attraction, in addition to basic tools like brushing and polygon marking. We aimed to generate a more advanced model with nine regions of interest, segmented from an MRI measured at UKSH Kiel as mentioned in section (3.1.1).

The segmented regions included lungs, spleen, two kidneys, bones, heart, liver, stomach, esophagus, and the rest of the torso, and the conductivities were based on previous studies. Since we did not find any study on the conductivity of the esophagus, we assumed its conductivity to be 0.202 S/m, as for perpendicular muscles [Kel+10]. The values the we used for those organs are shown in table 3.1. The resulting model is shown in figure (3.14) with the segmented nine regions of interest in a two and three dimensional views.

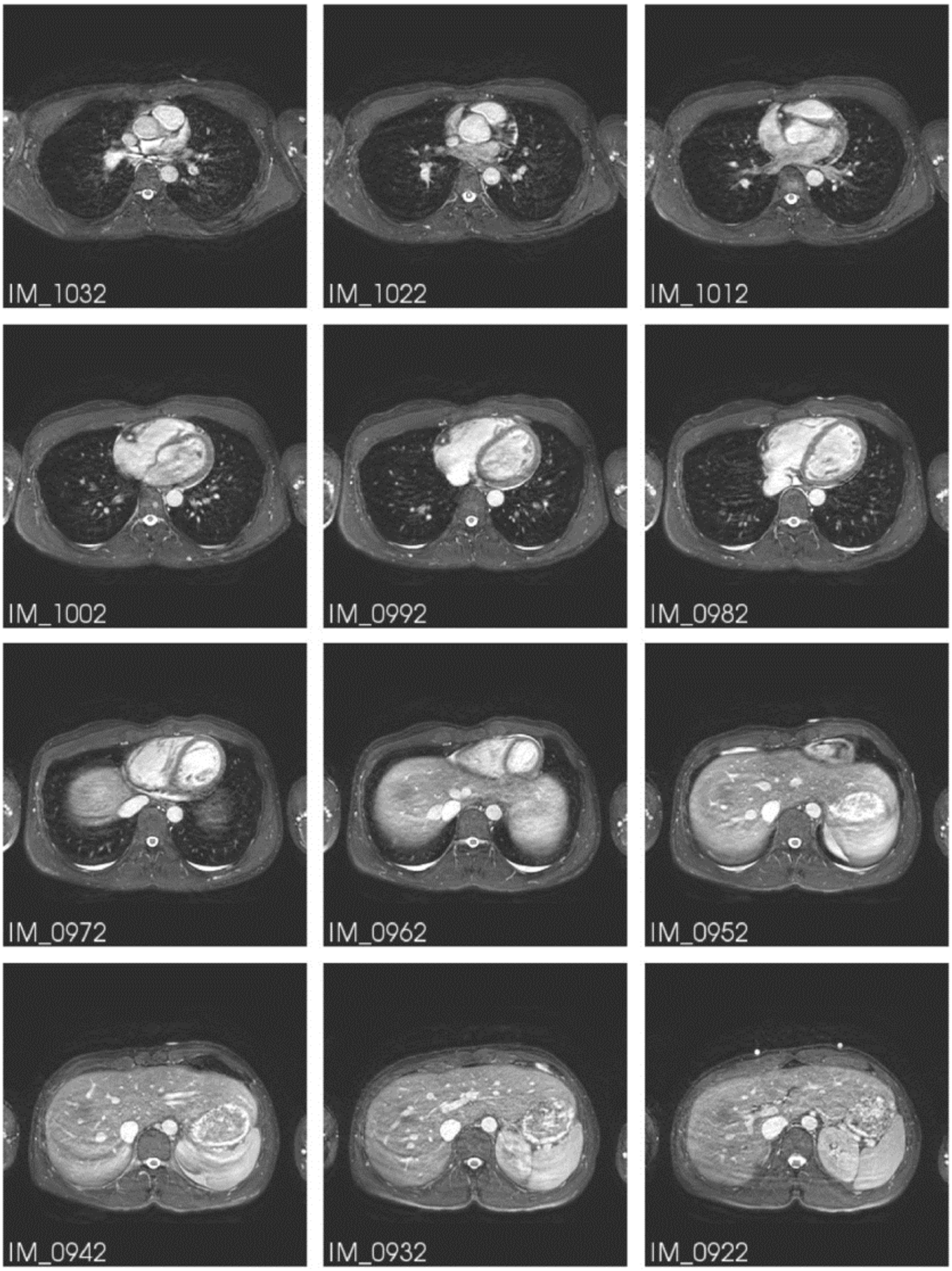

Figure 3.12: High resolution MRI series 701 of a torso with a heart at diastole, used for the first model. The MRI is from the publication by Prof. Hans Koch et al. [Koc+11].

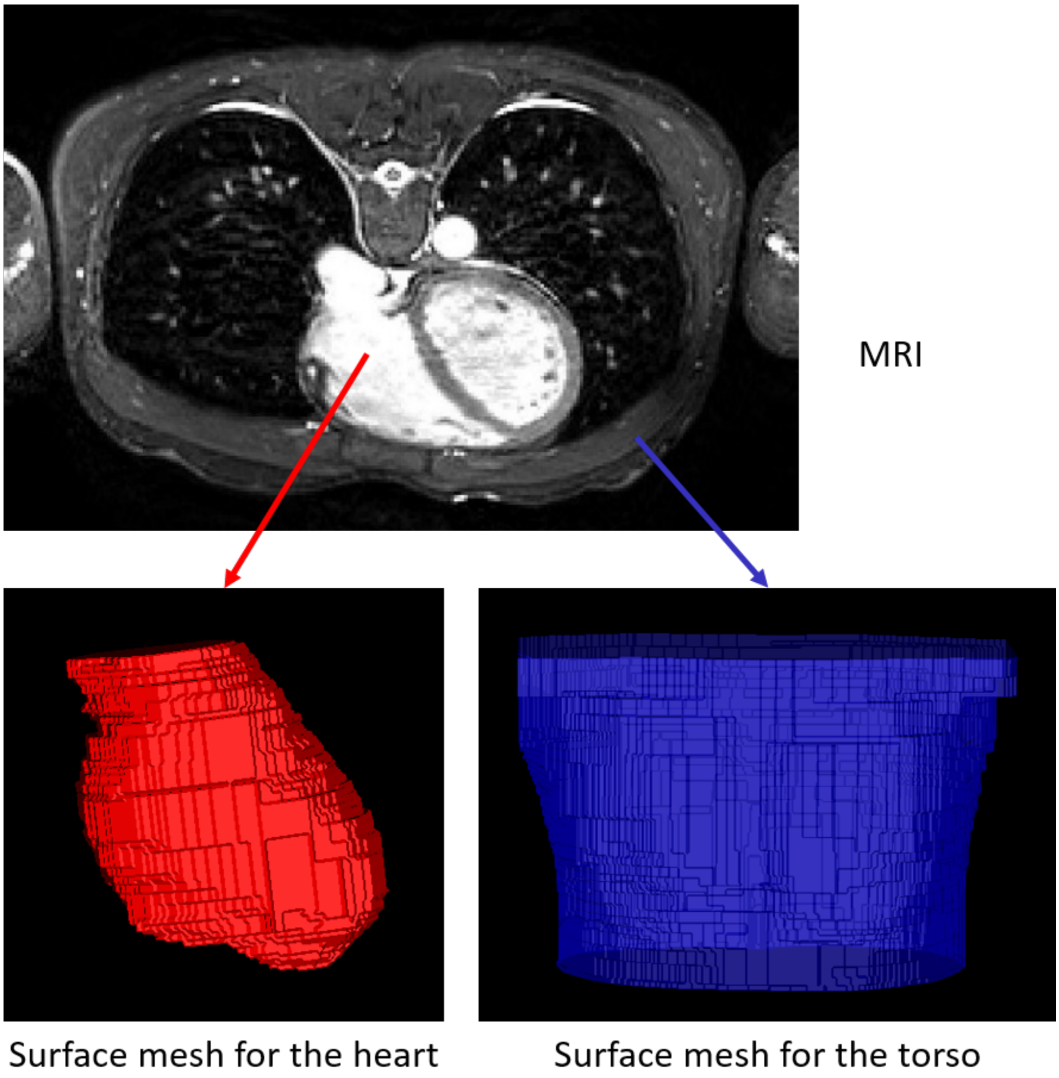

Figure 3.13: Segmented torso and heart meshes for the first model. The top image is an MRI slice used to segment layers or regions of interest. The left image in red is the heart mesh model, and the right image in blue is the torso mesh model.

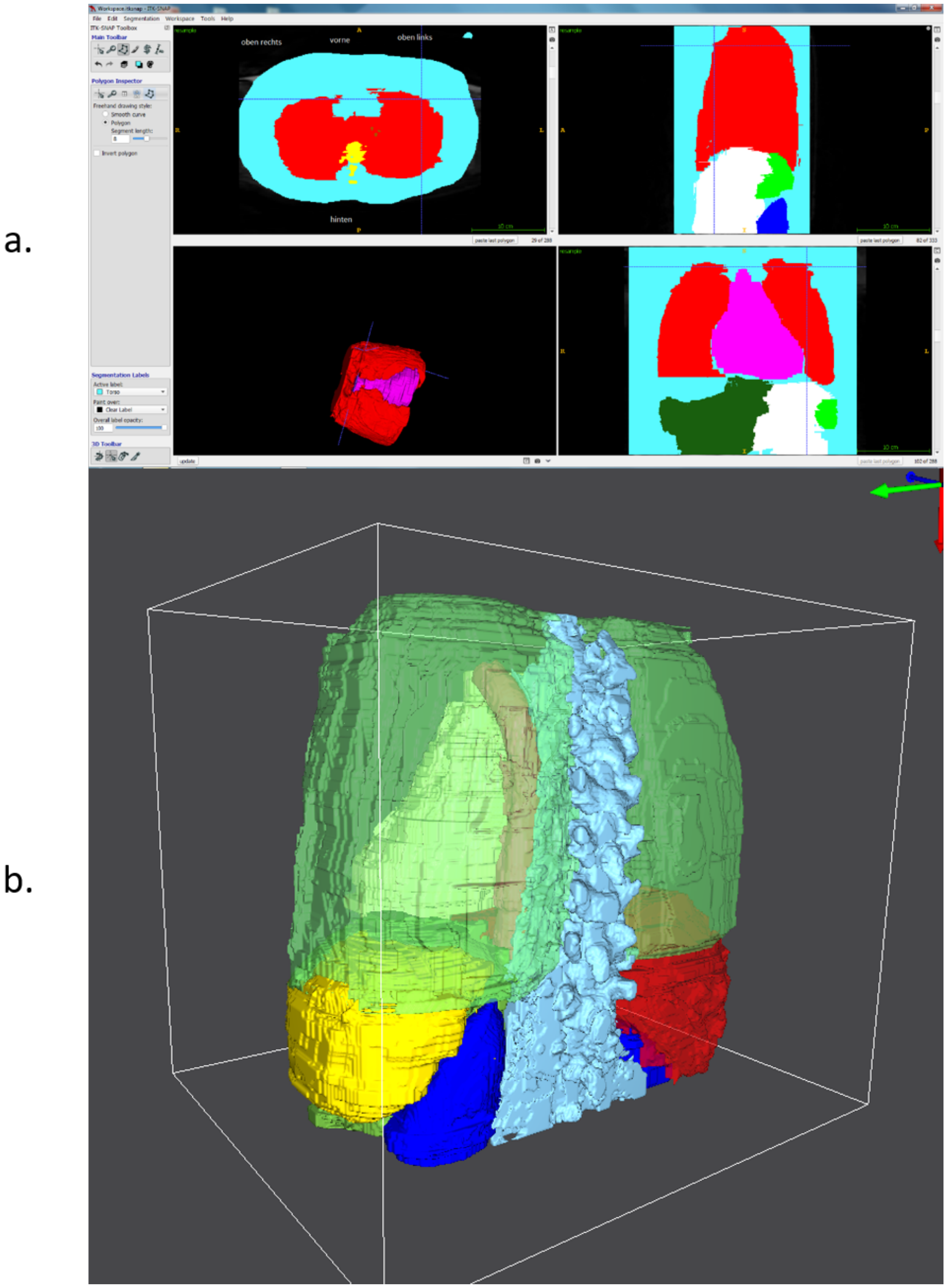

Figure 3.14: The segmented torso model with nine regions of interest. a. shows the second model during segmentation using the ITK-SNAP interface, and b. shows the model with transparency, revealing more layers.

.

Organ	**Conductivity (S/m)**	**Reference**
Lungs	0.05	[Sov+14]
Spleen	0.0396	[Kel+10]
Kidneys	0.0544	[Kel+10]
Bones	0.006	[Sov+14]
Heart	0.6	[Ahr15]
Liver	0.12	[Luo+18]
Stomach	0.523	[Luo+18]
Esophagus	0.202	[Kel+10]
Rest of the torso, including fat between the organs	0.2	[Sov+14]

Table 3.1: Conductivity values for different organs that we segmented and their relevant references

3.2.2 MRI Meshing

Multiple software and transformations were used to convert the MRI from its recorded Digital Imaging and Communications in Medicine (DICOM) format to a Finite Element Method (FEM) mesh with Vista format. After segmenting the MRI using Seg3D software, it was saved as a binary MRI in DICOM format, where each segmented layer has a fixed conductivity value for the whole layer. [CIB16]

In the second step, the MRI was transformed from the DICOM image-based format to Neuroimaging Informatics Technology Initiative (NIfTI) format. To achieve this, we used a converter called dcm2nii [Li+16] from the MRIcron software, which is a free NIfTI viewer.

As the third step, a MATLAB-based function, SimBio, was used to convert the MRI into the Vista format [Vor+18]. Finally, the SimBio-Vrgid mesh generator was used to generate a homogeneous cubical FEM mesh model, as shown in figure (3.15). The stages and transformations of the meshing process are illustrated in figure (3.16).

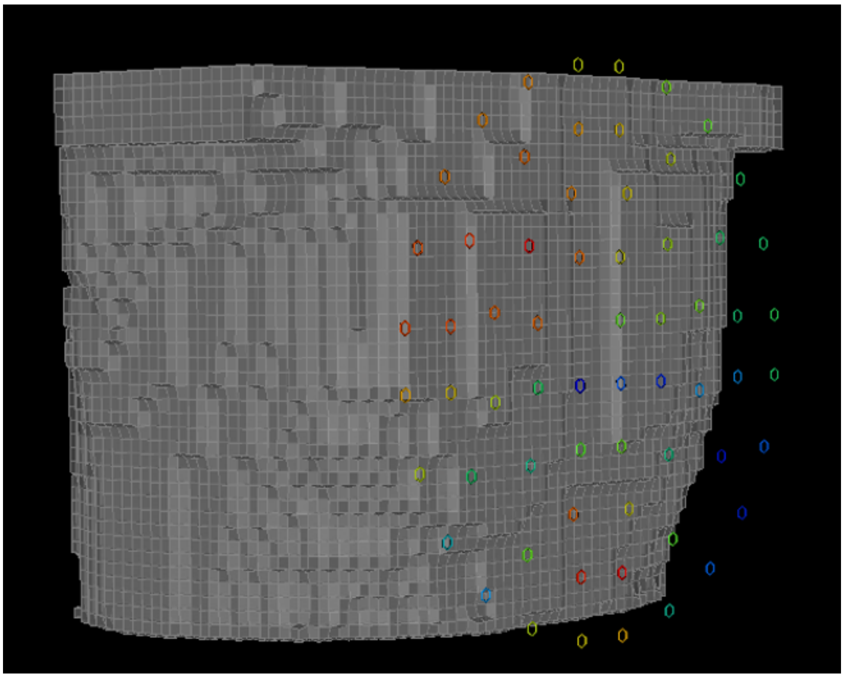

Figure 3.15: A homogeneous cubical FEM mesh for the first model.

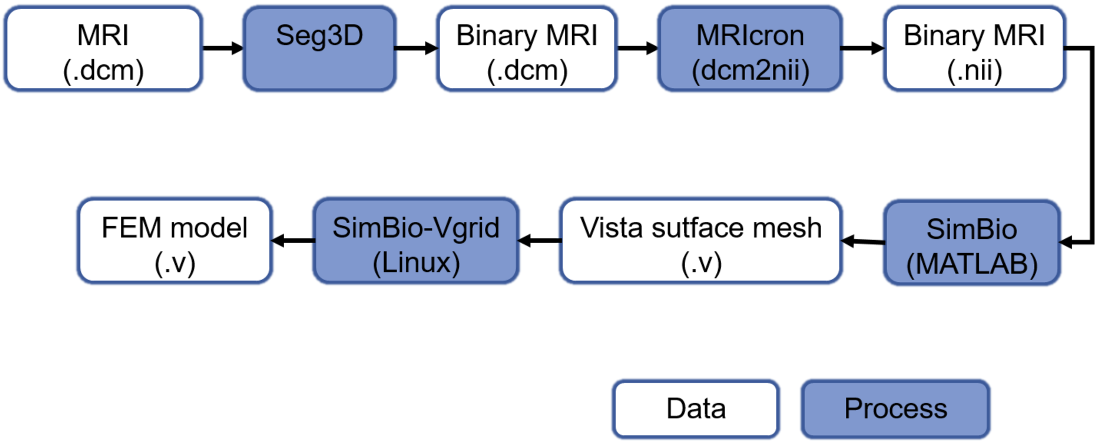

Figure 3.16: Block diagram illustrating the stages and transformations for meshing from MRI to a FEM model.

3.3 Forward Modelling

In this section, we discuss how we solved the forward problem using SimBio, a free and open-source software. SimBio's source code is written in C++/Fortran, and it is compiled to run on Linux operating systems. Although SimBio is a generic medical software, its primary purpose is to analyse EEG and MEG data for brain research. The uniqueness of SimBio lies in its ability to solve not only the forward problem for the electrical field, but also for the magnetic field, which is the focus of this thesis. [Sim21]

SimBio was developed by the Information Society Technologies (IST) Programme in 2000 as a generic environment for bionumerical simulation. Multiple groups, including the MPI for Mathematics in the Sciences in Leipzig, Biomagnetic Center in Jena, and MPI for Human Cognitive and Brain Sciences in Leipzig, tested and developed SimBio between 2006 and 2009. From 2011 to 2014, the Institute for Geometry and Physical Mathematics in RWTH Aachen, Institute of Biomedical Engineering and Informatics in TU Ilmenau, and the MPI for Human Cognitive and Brain Sciences in Leipzig further developed SimBio with funding from the German Research Foundation (DFG) - Deutsche Forschungsgemeinschaft. We thank Alexander Hunold from Ilmenau University of Technology for his support in using SimBio.

SimBio does not have a Graphical User Interface (GUI) and uses the Continuous Galerkin Finite Element Method (CG-FEM). One of the main problems with implementing a Finite Element Method (FEM) is how to deal with the singularity that occurs due to the model assumption of a mathematical dipole. There are four approaches to deal with this singularity: Venant, partial integration, subtraction approach, and Whitney approach. We used a SimBio file that is compiled for the Venant approach, as it was the recommended and provided approach from the developer group. [Vor16]

SimBio is poorly documented, and it runs through the Linux command-line interface. Although some SimBio functions for solving the electrical field forward problem were implemented for MATLAB within the FieldTrip toolbox [Fie], there are no functions to solve the magnetic field forward problem, which is the focus of this thesis. Therefore, we had to use the Linux version. We provide an example of one command line below:

```
./ipm_linux_opt_Venant -i sourcesimulation -p Parameter_File.par -fwd FEM
-h Torso_Model_File.v -sens MEG -s Sensors_Model_File.grd
-dip Source_Model_File.dip -o Results.msr &> Output.out &
```

The `ipm_linux_opt_Venant` in the command above is the name of the SimBio compiled file, and there are three flag inputs. The `-i` flag represents the type of input as a source simulation, and the `-fwd` flag represents the type of forward modeling by FEM. The third flag follows `-sens` and specifies the type of sensors we are working with, whether magnetic or electric.

In the command, there are also four input files and two output files. The first input file is led by `-s`, it describes the magnetic sensor models, whether magnetometers or gradiometers, their locations and orientations. It also describes how the sensor models calculate the magnetic field locally from the electric field. In this thesis, we used two sensor layouts, one of them is from the PTB as described in section (3.1.1), which has 304 SQUID magnetometers but we used only 57 sensors that are on the closest layer to the heart and directed to it. The second layout is described in (3.1.2), it has 63 sensors SQUID gradiometers.

The second input file is the `Torso_Model_File.v`, it follows `-h`. It represents the torso model and has information about locations of the grid points and their connections with each other. Every grid point has a label that corresponds to the torso organ that it represents. This file has a Vista format and its extension is `.v`.

The third input file is `Sensors_Model_File.grd`, it is led by the `-s` and represents the sensor models and their locations like the SQUID magnetometers that we used in PTB Berlin in section (3.1.1). It describes the magnetic sensors grid by having their locations and the sensors model. In order to model the magnetometer, each one is represented by 16 points distributed in a circular formation with a diameter of 7 mm, this represent the circular shape of the magnetometer.

Since the magnetic flux can be calculated as surface integral, unlike the electrical field that can be calculated at specific points, we need to define surfaces around the magnetometer to find the looping magnetic flux. We do that at each of the 16 points by connecting each one with its two neighbours to form a triangle as illustrated in figure (3.17 b. and c.). After calculating the magnetic flux at each of the 16 points from the value of the electrical field at the meant point and its two neighbouring points, we calculate the looping magnetic flux around the magnetometer from the values of the magnetic flux at the 16 surfaces.

The fourth input file is `Parameter_File.par`, it follows the `-p` in the command above. This the parameter file is where we can set the conductivities of the organs layers, solver method, BEM/FEM model type and input or output files formats.

After every input file is constructed separately, we align the locations of the data from the first three files visually using MATLAB to make sure that the locations of the source grid, the torso model and the sensors are approximately in the right location to each other, then we run the SimBio executable file, through the command line in Linux.

The final component of the command consists of the output files. The first output file, `Results.msr`, generates multiple files with the same name but different extensions. These files contain the torso model with the estimated electrical field at all mesh points. The second output file is the log file, `Output.out`. It provides a summary of the input files used, the model mesh type, the number of nodes, parameter selection, calculation progress, and logs of any errors that may have occurred.

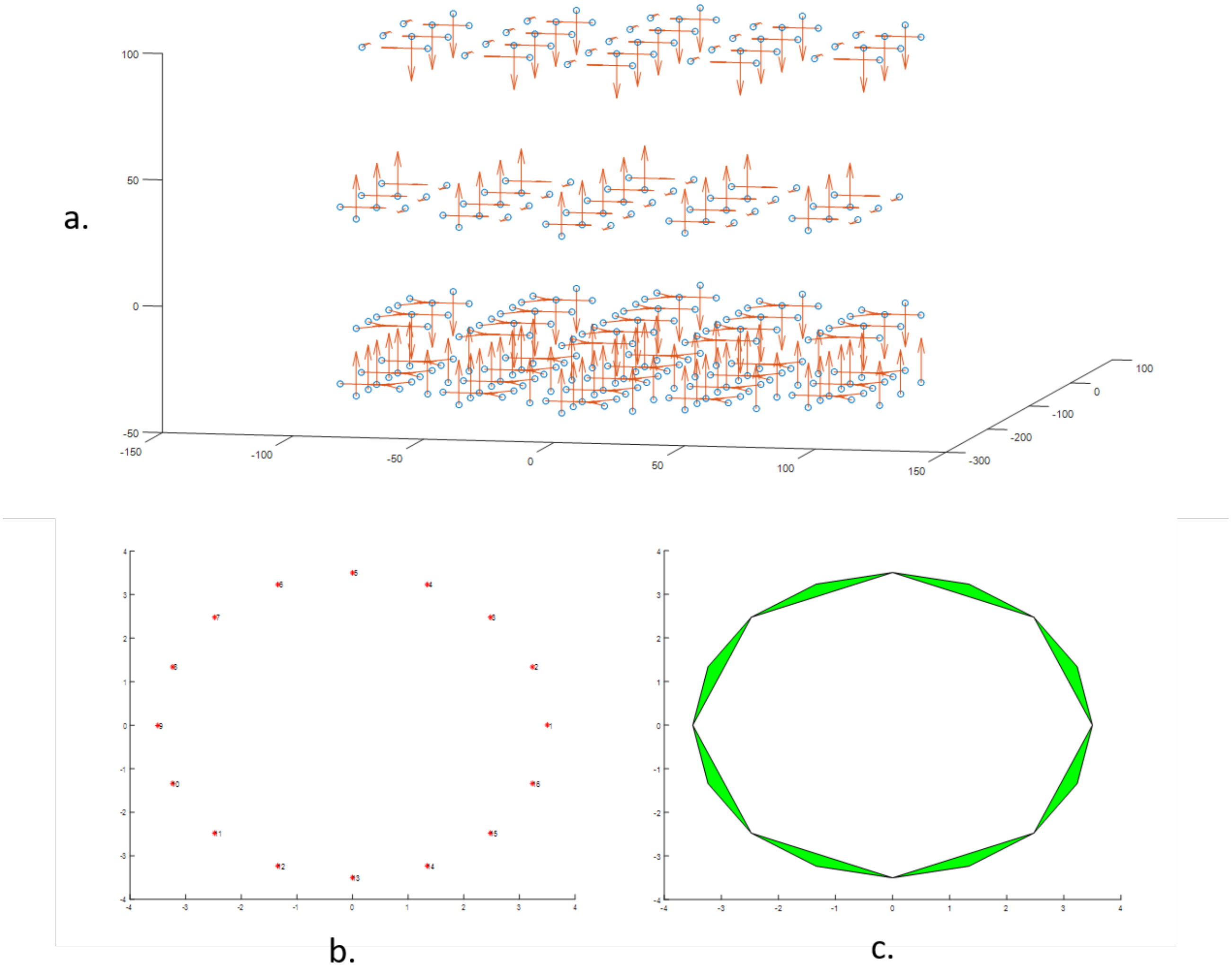

Figure 3.17: A sketch for the SQUID sensor model in MATLAB for the SimBio software. a. implementation of the PTB Berlin 304 SQUID system (see 3.1.1), every sensor here is represented with location and orientation, b. the model of each SQUID sensor, represented by 16 points on a circular formation. c. show how the SQUID points are connected in triangular formations to calculate the magnetic flux on the surface of the triangles from the electrical field values for the 3 edges of the triangle

.

3.4 Calculating the Lead-field Matrix

In order to solve the inverse problem, we need to calculate the lead-field matrix, which requires information about the source space, model, and sensors, as previously discussed in section (3.3). To obtain the lead-field matrix, we first modify the source space file (.dip) to include a unit vector activity in all grid locations and the three Cartesian orientations. Next, we use SimBio to calculate the lead-field matrix, which summarizes the torso model and establishes a direct relationship between all source points and sensors. This matrix is critical to the inverse problem solution.

Chapter 4

MCG Simulations and Analyses

In this chapter, we aim to test our pipeline using a simulated data set. We chose to use simulated data rather than real data for two main reasons: firstly, we know the exact location of the source and can compare it with the estimated location, and secondly, we have control over the noise level and dynamical activity of the source.

We created three simulation scenarios with the data set. In the first two scenarios, we simulated a source inside the heart - once as a static source and once as a dynamical source. We tested our pipeline using three inverse problem methods: MNE, LORETA, and STKF inverse methods. The work done in the first two scenarios has been published in [Hab+18].

In the third part of our study, we simulated datasets from different directions of the torso to study the effect of the number and direction of the SQUIDs array on the measurement of the MCG and the estimation of the source location. This analysis helped us understand how the SQUID array's placement affects the accuracy of the estimated source location.

4.1 Solving the Inverse Problem for Simulated MCG Dataset 1

4.1.1 Motivation

In this section, we present our analysis of the first simulated MCG dataset. We generated multiple MCG datasets with different dynamical noises by using a fixed location and changing amplitude source. Our aim was to analyse this dataset using three inverse problem methods, MNE, LORETA, and STKF, to compare the effect of noise level on the accuracy of the source estimation.

4.1.2 Generating the Magnetocardiographic Data

In this study, we simulated MCG data by generating multiple datasets with varying levels of dynamical noise. To create these datasets, we selected a single channel from a real

MCG signal, as shown in figure (4.1). We placed this time series on a voxel located at the centre of a 3D volumetric grid representing the heart. The activity was changing only in the vertical orientation (y-axis) from head to feet, with no activity on the two other Cartesian axes. This scenario was selected because it resembles the real scenario where the atrioventricular node in the heart is active, and the electrical potential propagates downwards to the common bundle and bundle branches, as shown in figure (4.2).

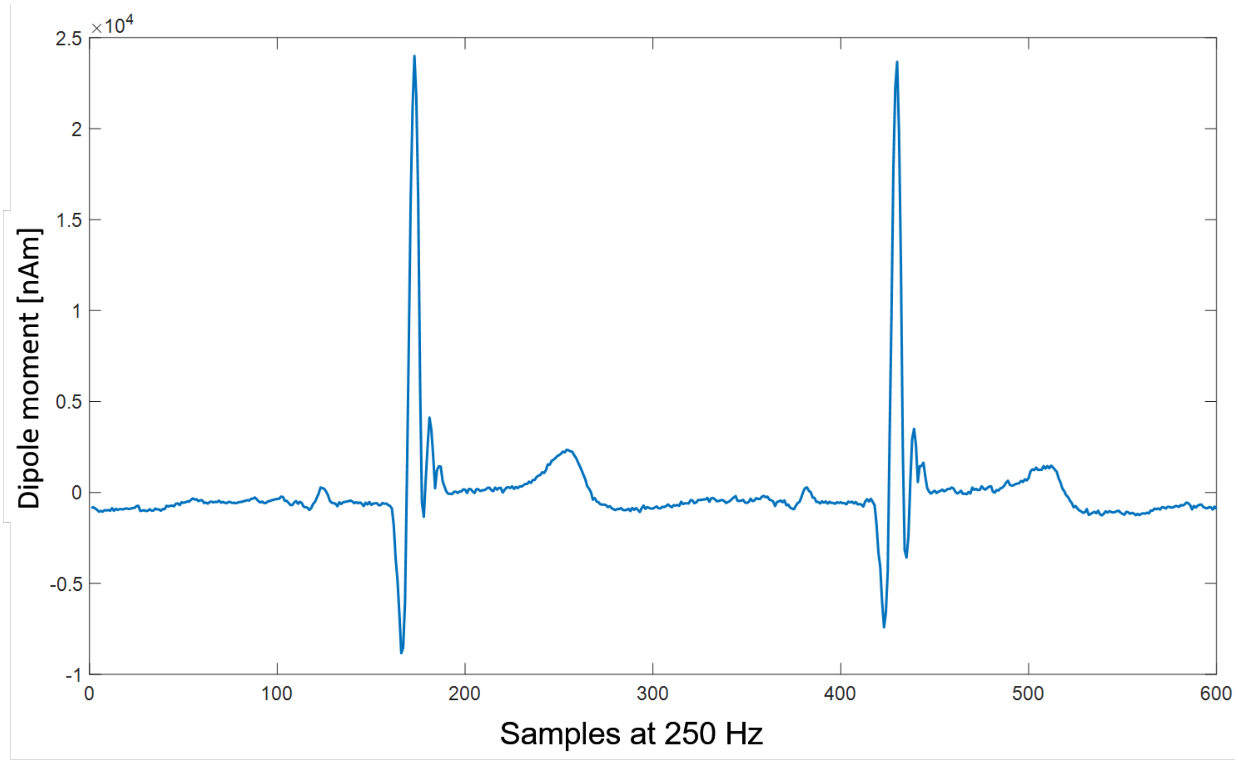

Figure 4.1: A representation of a single channel real MCG SQUID that we used as a source to simulate an MCG data set. The y-axis represent the amplitude of the time series and x-axis represent the time points, the signal has a sampling rate of 250 Hz

.

To generate the simulated MCG dataset with 63 sensors, we multiplied the simulated signal by the LFM obtained from the solution of the magnetic forward problem, as explained in sections (3.3) and (3.4). To calcualte the LFM, we used the layout of the 63 sensors shown in figure (4.6), which was based on a dataset measured in a previous PhD work [Ahr15] and we used the first torso model described in subsection (3.2.1) and shown in figure (3.13).

The resulting simulated MCG dataset, shown in figure (4.3), consists of 600 samples with a sampling rate of 250 Hz.

We added white Gaussian noise (AWGN) to the clean signal at different levels of SNR, ranging from -30 dB to 20 dB, with a step difference of 5 dB at each level. The noise added to each dataset had a random seed. In total, we generated 13 datasets: one was noise-free

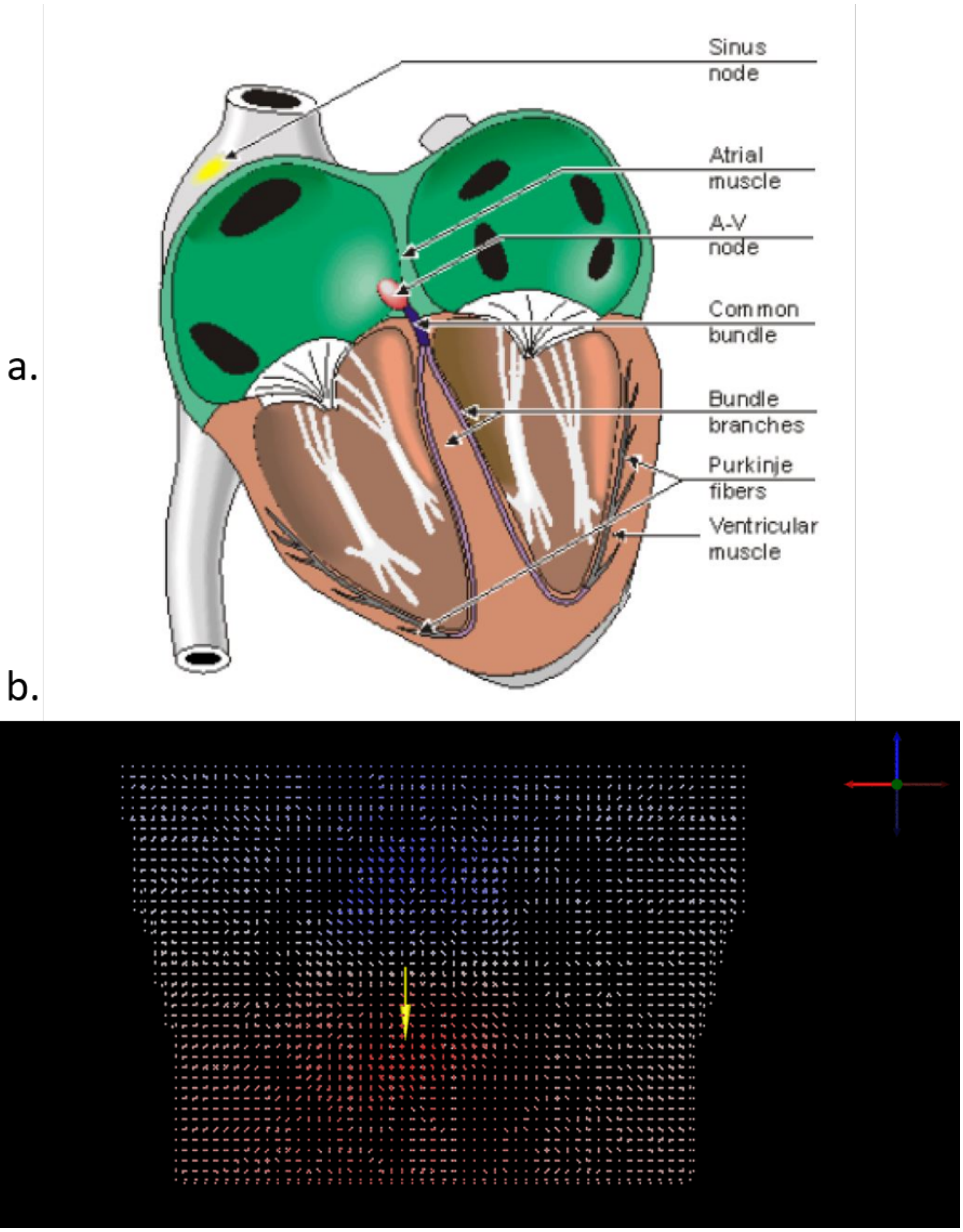

Figure 4.2: A simulation of one dipole heart activity and its relevant heart activity at the AV node downward to the common bundle a. represents a vertical section of the human heart showing the sinus and atrioventricular nodes of the heart and the relevant bundles, fibres and muscles that are relevant to the electrical cycle in the heart [MP95], b. represents grid point for the torso and heart models colour coded with electrical potentials. In the centre of the heart there is yellow dipole that represents the location and direction of the simulated source dipole.

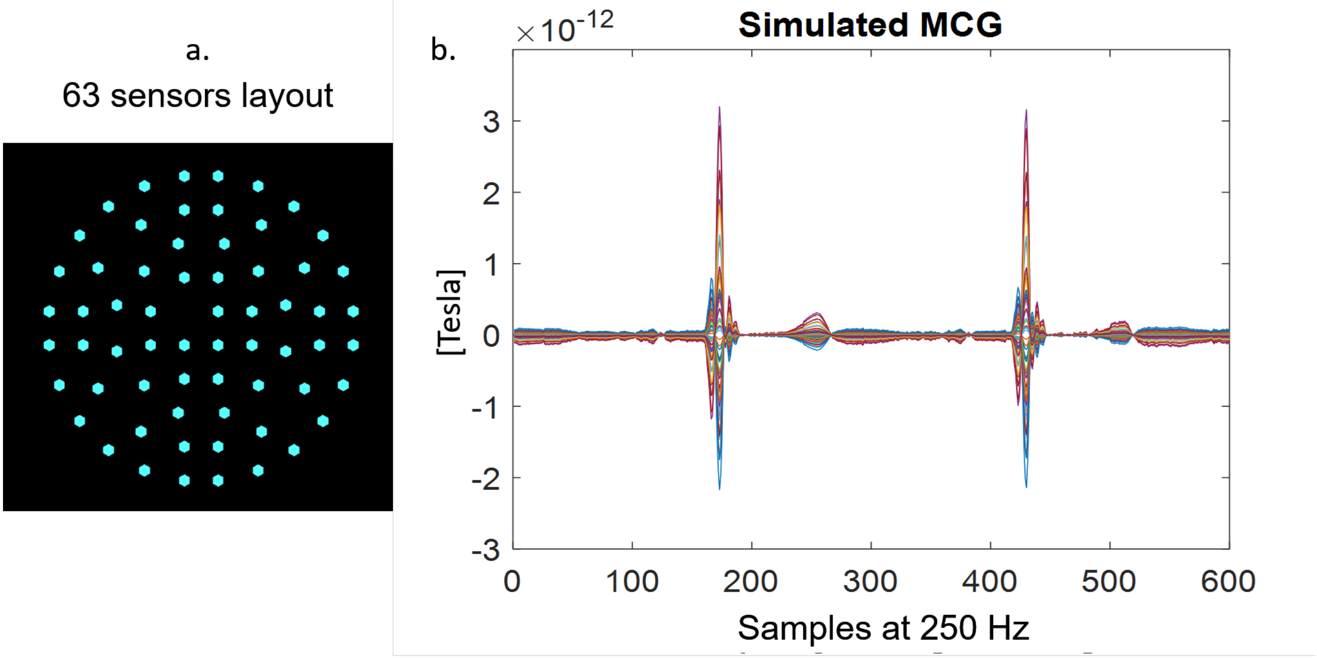

Figure 4.3: An MCG sensor array and the recorded MCG dataset a. shows the 63 MCG layout that we used to generate the dataset [Ahr15], b. The generated MCG, the left axis shows the MCG with butterfly plot of 63 channel, the sampling rate is 250 Hz and time series has 600 time points

.

(shown in figure (4.3 b)), and the other 12 were mixed with AWGN. The varying levels of noise allowed us to investigate the effect of noise on the accuracy of source estimation using MNE, LORETA, and STKF, as discussed in section (4.1). It is worth mentioning that the noise added to each dataset had a random seed.

4.1.3 Analyses

In this study, we aimed to localise the source of 13 simulated datasets using three inverse problem methods: MNE, LORETA, and STKF, and evaluated how close the estimated source was to the original simulated one. We used a source grid resolution of 10 mm due to the time consumption of the STKF method.

The MNE method is not ideal for estimating deep sources since its estimation is strongly biased to the surface, while the source we simulated was at the centre of the heart. On the other hand, the results from LORETA and STKF are comparable.

For the clean dataset that had no AWGN, both LORETA and STKF showed no difference between the location of the original and the estimated source. At an SNR level of 20 dB, both LORETA and STKF showed a distance of 10 mm between the simulated and the estimated locations. At SNR levels of 5 dB and 10 dB, the distance to the original source was 10 mm for STKF and increased to 14.1 mm for LORETA.

At an SNR level of 0 dB, the distance error of the STKF was 17.3 mm, but it stayed fixed at 14.1 mm for LORETA. For the dataset with an SNR level of -5 dB, the STKF localization error further increased to 30 mm, while it was stable at 14.1 mm for LORETA. At SNR levels from -10 dB to -20 dB, the localization error for STKF decreased to 14.1 mm and 10 mm for LORETA.

The location errors significantly increased for LORETA to 44.7 mm for the case of -25 dB and to 58.3 mm for -30 dB, while the distances for the STKF at the same SNR levels were relatively lower at 17.3 mm and 22.4 mm for -25 dB and -30 dB, respectively.

Figure (4.4) shows the distances between the original and estimated sources for LORETA and STKF plotted with respect to the SNR values. For comparison, we included the STKF and LORETA results for the simulated data without adding AWGN, which is shown on the plot as the last value with the highest SNR (at 25 dB).

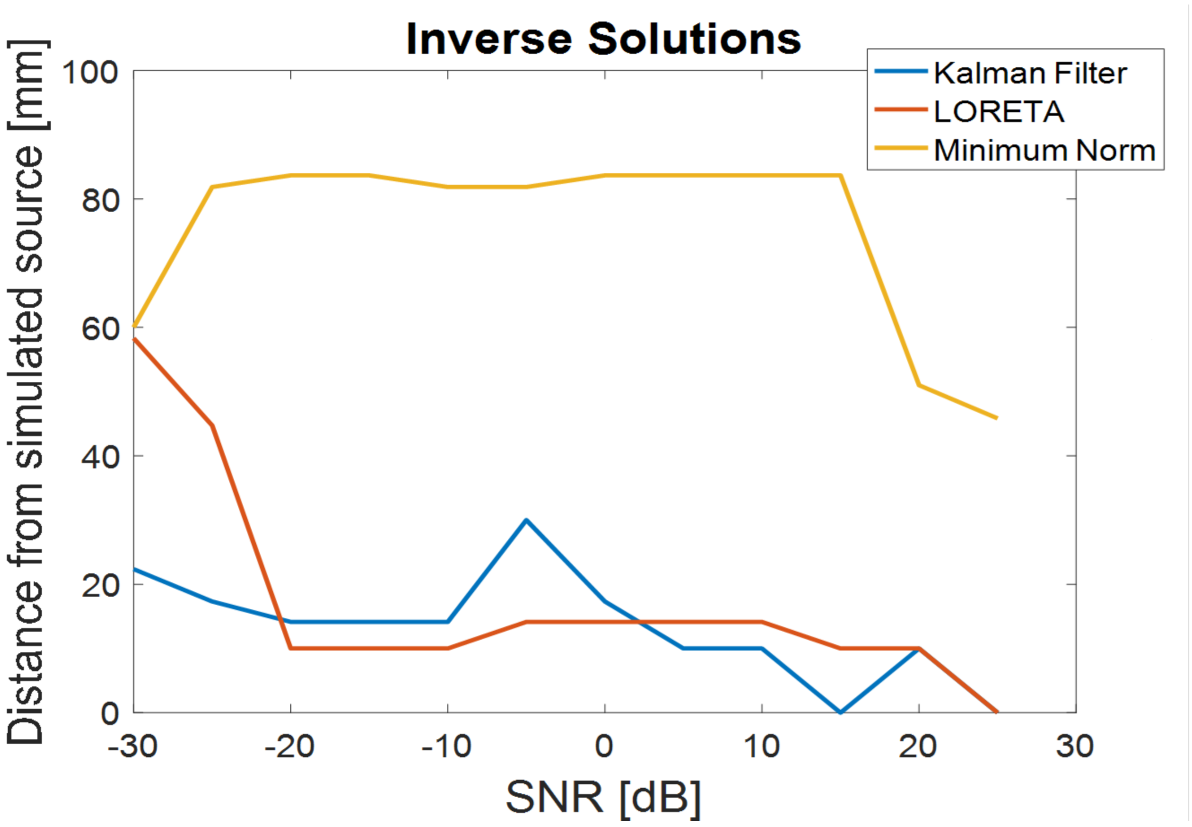

Figure 4.4: Results of analysing the simulated datasets with three inverse problem methods, namely MNE, LORETA, and STKF. The x-axis shows the SNR level added to the datasets in dB, the y-axis shows the distance difference between the originally simulated source and the estimated location in millimeters (mm). The total number of datasets is 13, with 12 of them distributed between -30 dB and 20 dB on the x-axis. The value at 25 dB is the result from the dataset without AWGN, added for comparison purposes.

4.1.4 Discussion

Our analyses show that both LORETA and STKF are effective methods for MCG source imaging. However, their performance varies depending on the SNR level. At high SNR levels (SNR = 20 dB) and without any added noise, the localisation results from both methods are similar and accurate. As the SNR level decreases, the performance of both methods also decreases. It would be desirable to have results for several simulated data sets, not just one, to see a distribution of results. Figure 4.4 indicates that there is considerable fluctuation. However, analysing several data sets with STKF may be very time-consuming.

Between SNR levels of 5 dB and 15 dB, the performance of STKF is slightly better than that of LORETA. On the other hand, for SNR levels between -5 dB and -20 dB, the performance of LORETA is better than that of STKF. Notably, the performance of LORETA dramatically worsens at SNR levels of –25 dB and lower, whereas the localization error for STKF remains relatively lower.

The choice of method may depend on the specific research question, as well as practical considerations such as computational resources and time consumption. In our analyses, we used a source grid resolution of 10 mm due to the time consumption of the STKF method, but higher resolutions may increase the time consumption significantly.

In summary, our results suggest that both LORETA and STKF are suitable methods for MCG source imaging, but their performance may differ depending on the SNR level. Researchers should carefully consider the specific requirements of their study when selecting a method for MCG source imaging.

4.2 Solving the Inverse Problem for Simulated MCG Dataset 2

4.2.1 Motivation

In order to further investigate the accuracy of source estimation in dynamic scenarios, we simulated a second dataset with a more complex dipole. In this dataset, the amplitude of the dipole changes in two directions while its location remains fixed. We used this source to generate multiple MCG datasets with varying levels of dynamical noise. We then analysed this dataset using MNE, LORETA, and STKF to compare the effect of noise levels on the accuracy of source estimation in a more dynamic scenario.

4.2.2 Generation of Magnetocardiographic Data

For this simulation, we used an artificial and highly dynamic signal instead of real MCG data as in (4.1.2). The signal was simulated at the centre of the heart, and the dipole was rotating around the x-axis (from shoulder to shoulder), causing the signal amplitude to change on the y- and z- axes while remaining fixed with a small value on the x-axis.

To generate the signal, we used an autoregressive model of order two (AR2) with white Gaussian driving noise. The model's parameters were as follows: a_1 = 1.97, a_2 = -0.98, and the driving noise variance $\sigma_\eta^2 = 0.7$. We used the scalar dynamics of a fixed-orientation current dipole located at a single mesh point:

$$\boldsymbol{j}_t = a_1\boldsymbol{j}_{t-1} + a_2\boldsymbol{j}_{t-2} + \boldsymbol{\eta}_t \tag{4.1}$$

We used the following equations to determine a_1 and a_2 in order to specify the frequency of the oscillation:

$$a_1 = 2\rho cos(\phi) \tag{4.2}$$

$$a_2 = -\rho^2 \tag{4.3}$$

For a detailed explanation of the derivation of equations (4.2) and (4.3), please refer to [AHEHS18].

The simulated signal was made to rotate by multiplying the y-component by a cosine wave and the z-component by a sine wave, while the value was fixed in the x-axis [Ste08; Hab14].

The resulting MCG data had 500 time points and a sampling rate of 250 Hz. The signal is shown in figure (4.5). We then multiplied the signal by the LFM to generate a noise-free dataset as shown in figure (4.6), we used the same LFM as explained in subsection (4.1.2).

Before adding AWGN noise with SNR to generate 7 datasets with different SNR levels distributed between -10 dB and 20 dB, with a step size of 5 dB between each dataset.

4.2.3 Analyses

The MNE results for this dataset are also biased towards the surface, the bias is around 40 mm for datasets with SNR levels between -5 dB and 20 dB, and it worsens significantly for the -10 dB dataset.

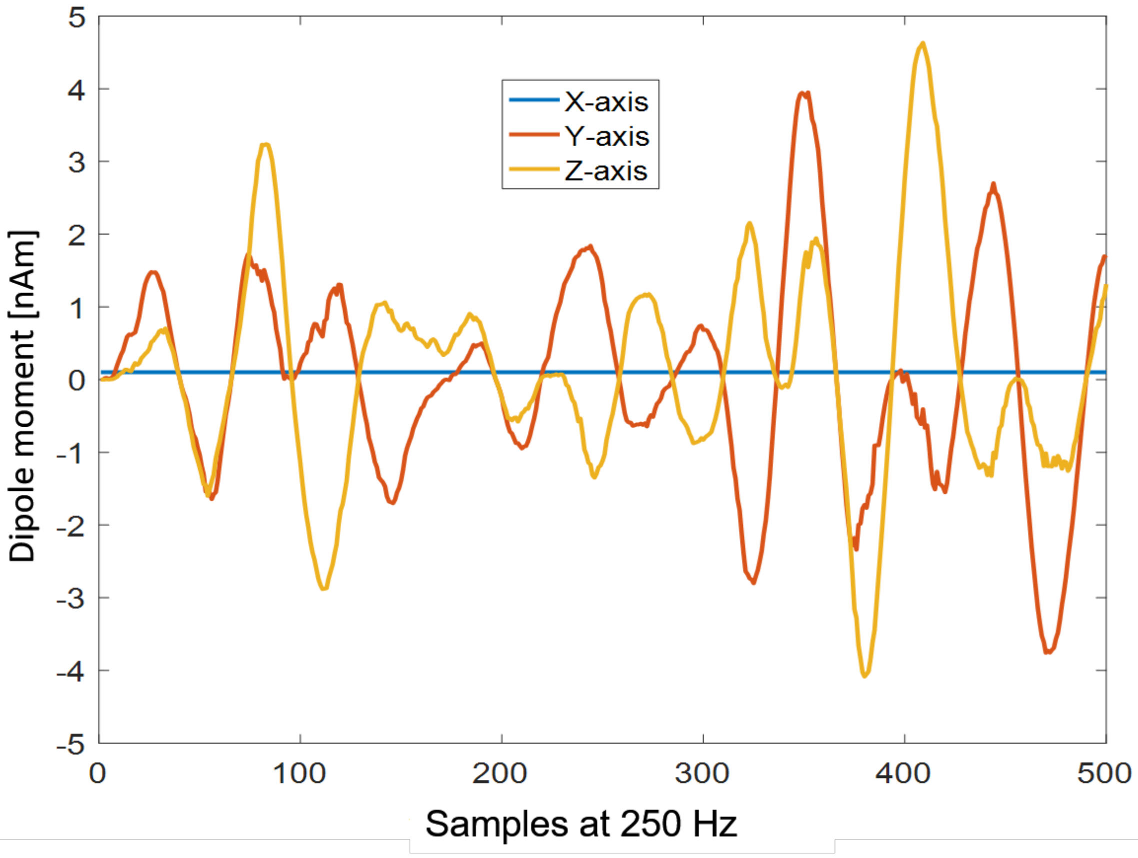

Figure 4.5: The amplitude variation of the artificial three-dimensional signal we generated in the three Cartesian axes, as shown in the legend for relevant colors. The signal has 500 time points with a sampling rate of 250 Hz.

The LORETA and STKF results are comparable. The distance between the simulated and estimated source locations is 10 mm for both LORETA and STKF for SNR levels between 20 dB and 10 dB, as well as for the case of no AWGN. For SNR levels of 5 dB and 0 dB, the STKF localised the source activity at a distance error of 10 mm, while LORETA localised it at a distance error of 22.4 mm.

The STKF estimated the location exactly as its original location for SNR levels of -5 dB and -10 dB. For LORETA, the distance at -5 dB SNR level is 28.3 mm, and at -10 dB SNR level, it is 51 mm, which is worse. The source grid resolution is 10 mm. Figure (4.7) summarizes the comparison between LORETA and STKF.

The STKF exhibits an improvement for lower SNR levels, which is counter-intuitive. However, since we added AWGN with different seeds for the datasets at each SNR level, the values of MNE, LORETA, and STKF are comparable at each SNR level. The behaviour of each method over the entire range of SNR levels shows a general trend but may not be logically consistent. In a typical scenario, we would run LORETA and STKF multiple times with different seeds of AWGN to have a distribution of results and eventually obtain a more comprehensive outcome. However, this would increase the time

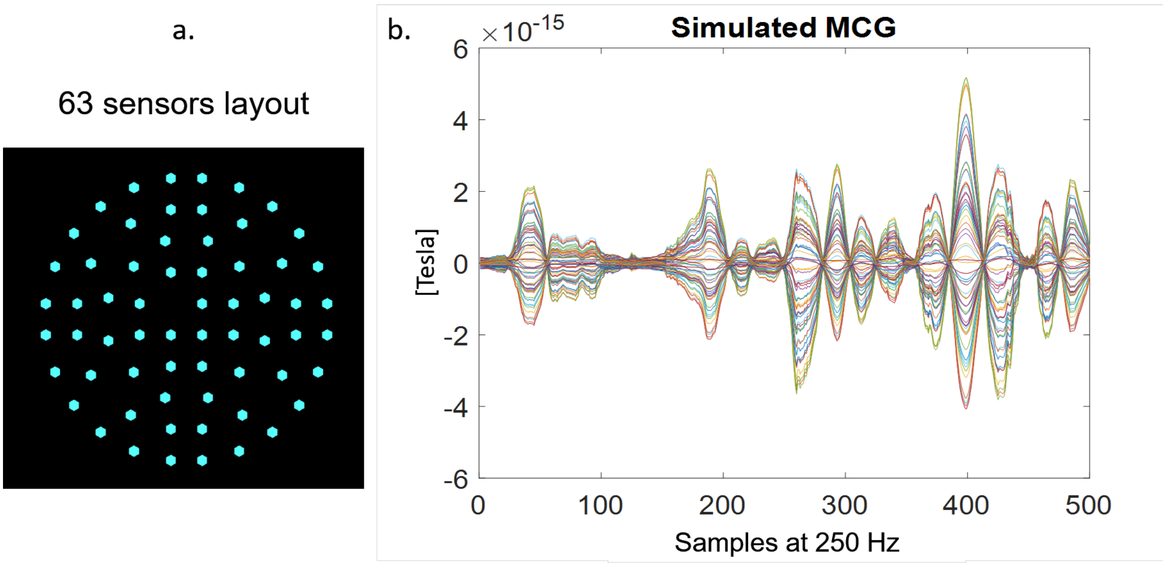

Figure 4.6: An MCG sensor array and the generated MCG dataset. a. shows the 63-channel MCG layout that we used to generate the dataset [Ahr15], and b. shows the generated MCG with a butterfly plot of the 63 channels. The sampling rate is 250 Hz, and the signal has 500 time points.

consumption significantly for the STKF.

4.2.4 Discussion

The estimation results of both LORETA and STKF are similar for SNR levels of 10 dB and higher. LORETA's performance began to drop in comparison to STKF at 5 dB and below, while STKF remained robust. The maximum difference was at an SNR level of -10 dB, where the distance between the estimated and original source for LORETA was over 50 mm.

In summary, LORETA and STKF both perform effectively in medium to high SNR scenarios (20 dB for the first dataset and 10 dB for the second dataset). However, STKF shows promising outcomes in low SNR scenarios, particularly in the second simulation.

We believe that STKF outperformed LORETA at higher noise levels because STKF considers not only the spatial smoothness in the source signal but also the temporal smoothness.

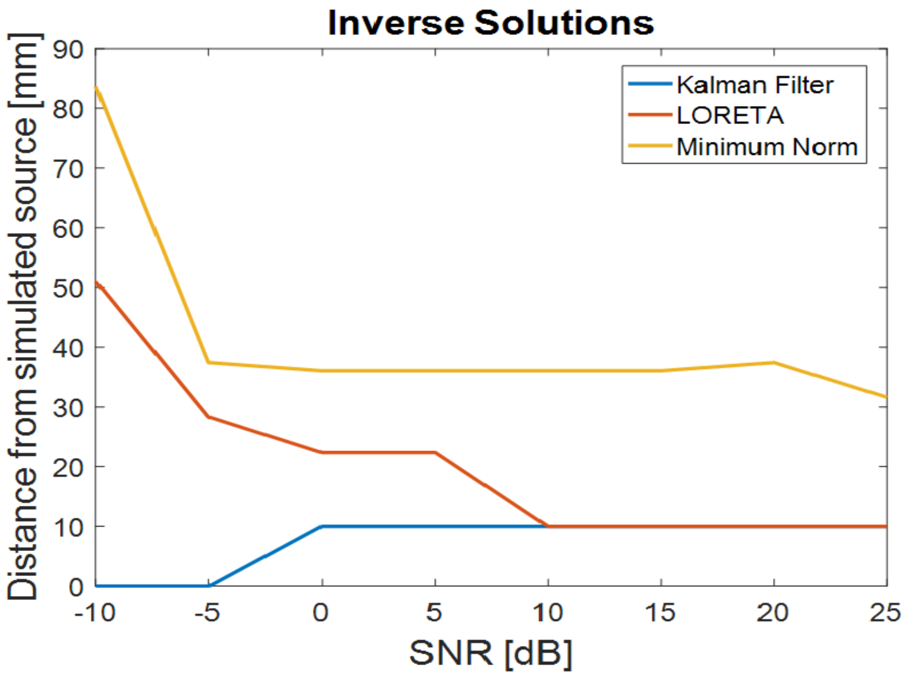

Figure 4.7: The plot shows the results of analysing the simulated datasets with three inverse problem methods, namely MNE, LORETA, and STKF. The x-axis shows the SNR level added to the datasets in dB, and the y-axis shows the distance between the originally simulated source and the estimated location in mm. The total number of data sets is eight, seven of which are distributed between -10 dB and 20 dB on the x-axis. The value at 25 dB is the result from the dataset without AWGN added for comparison purposes.

4.3 MCG SQUID Locations and Orientations

4.3.1 Motivation

In this section, we investigate the impact of the positioning and orientation of the sensor array around the torso on the MCG signal detection. The heart is located on the side-front part of the torso, slightly behind the sternum. Therefore, we anticipate that the detection will be stronger in the front and left side of the torso. As we do not have a female model or MRI, we only used a male human model, which may affect our results. We also anticipate that the distance between the sensors and the heart source locations, as well as the orientation and alignment of the sensors with the magnetic field, will play a role in our findings.

4.3.2 Generation of Magnetocardiographic Data

We used the simulated dataset generated in the previous section (4.2.2). We simulated the data in the middle of the heart as previously described, but instead of calculating the

LFM for only one frontal sensor array, we calculated nine LFMs for different sensor arrays and combinations of array setups. We used multiple sensor arrays in different positions and orientations to study the effect of positioning and orienting the sensor array around the torso. The model and sensor array setups are shown in figure (4.8). The source space and model resolutions were both set to 5 mm, and all sensor array planes were located at 20 mm away from the torso model boundaries.

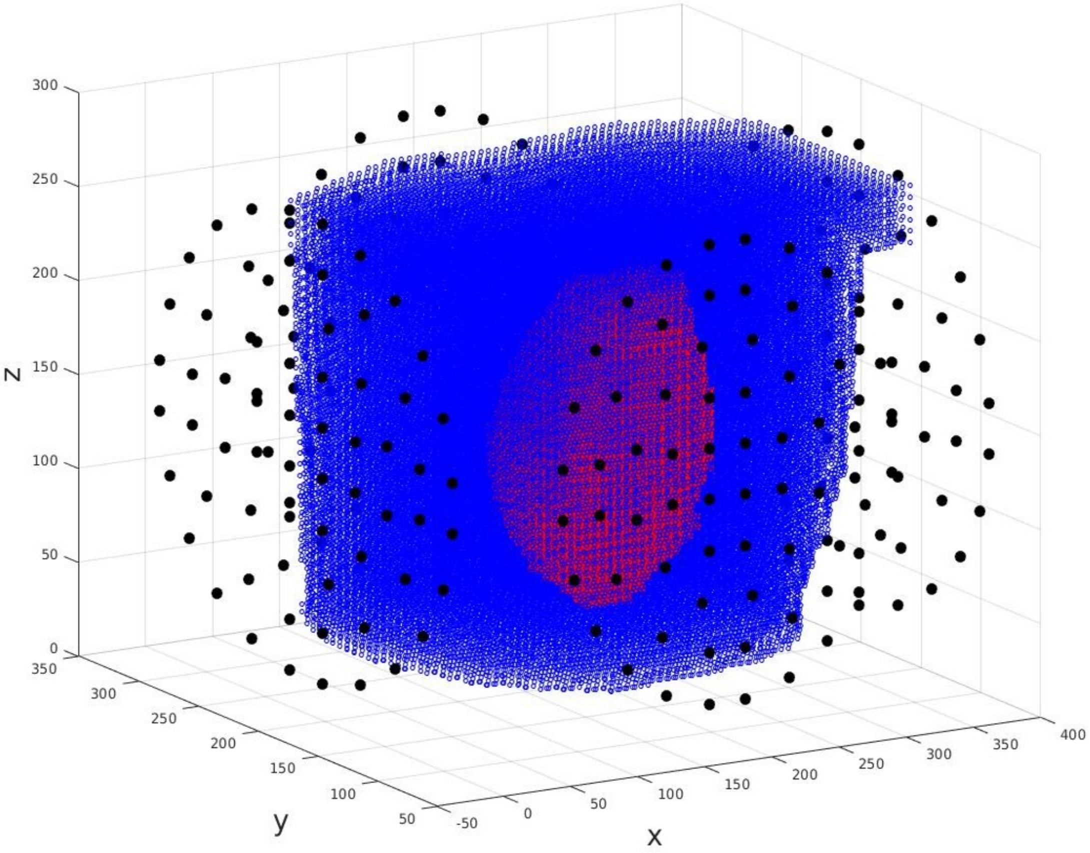

Figure 4.8: A model showing the torso-heart model with MCG SQUID sensor array from four directions: front, right, left, and back. Space unit is mm.

We have four main array setups, each with a different direction around the torso. From those four setups, we generated five more setups with combinations of arrays. From the total nine setups and the simulated source signal, we generated nine datasets. The sensors' orientations were also different, all directed towards the heart. For instance, the right-side sensors were oriented towards the left, and vice versa, while the front-side sensors were oriented towards the back side, and vice versa. The total nine combination setups with the number of arrays and sensors are explained in Table (4.1).

Sensors array setup	Number of arrays	Number of sensors
Four directions (Front, back, right and left)	4	252
Front, back and left	3	189
Right and left	2	126
Front and left	2	126
Front and back	2	126
Right	1	63
Left	1	63
Front (default setup)	1	63
Back	1	63

Table 4.1: Setup scenarios for simulating and analysing MCG datasets with different number of arrays, number of sensors and orientations

4.3.3 Analyses

After generating nine datasets with different scenarios, we used LORETA to localise the simulated source and compare it with the estimated/localised location. We calculated the Euclidean distance between the original simulation and the estimated location and presented the results in figure (4.9).

The scenario using the four-directional arrays with 252 sensors and the three directional arrays from the front, back, and left sides had the same Euclidean distance of 10.099 mm. The combination scenario of the right and left side arrays performed the best, with a Euclidean distance of 7.875 mm, while the combination scenarios of the front side with either the left or back sides had a Euclidean distance of 10.099 mm.

When using one side array at a time, the default setup with the front side array performed the best, with a Euclidean distance of 10.099 mm. The right side array had a slightly higher distance of 11.045 mm, and the left side array had an even higher distance of 12.124 mm. The back side array performed the worst, with a Euclidean distance of 37.775 mm.

We also show the inverse solutions for two scenarios in figure (4.10), where we had the highest and lowest Euclidean distance values. As mentioned in section (4.2.2), the simulated activity was placed in the centre of the heart.

We also show the inverse solutions for two scenarios in figure (4.10), where we had the highest and lowest Euclidean distance values. As mentioned in section (4.2.2), the simulated activity was placed in the centre of the heart.

Overall, our results demonstrate that using a combination of right and left side arrays provides the most accurate localization of the simulated source, while using the back side array alone results in the poorest performance. These findings have important implications for the design of future MCG studies involving cardiac source localisation.

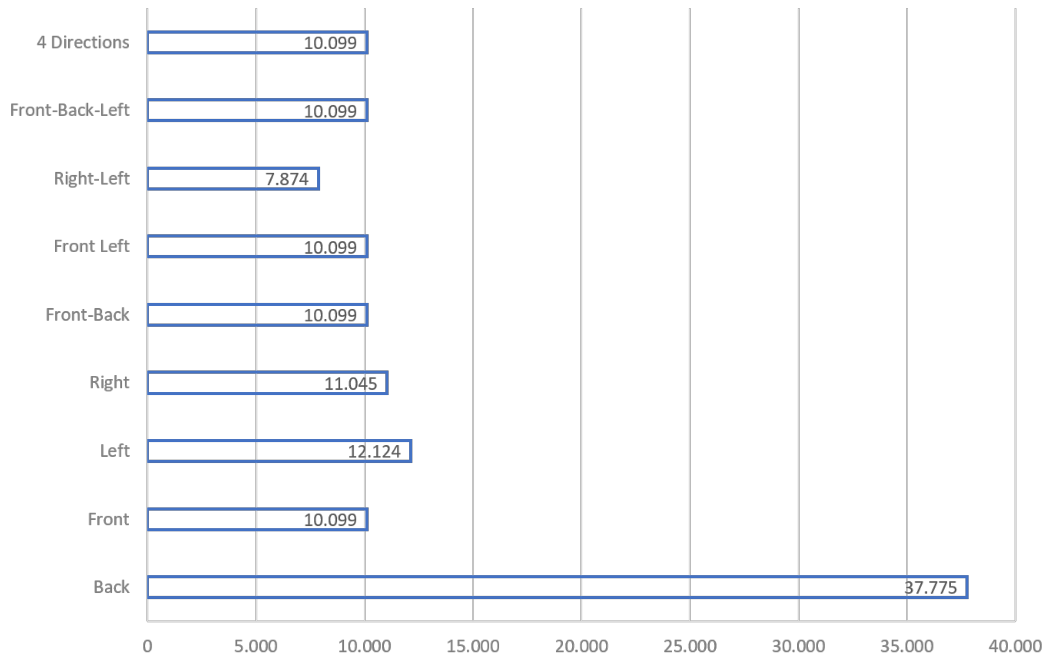

Figure 4.9: Euclidean distance between the original simulation and the estimated location (values in mm)

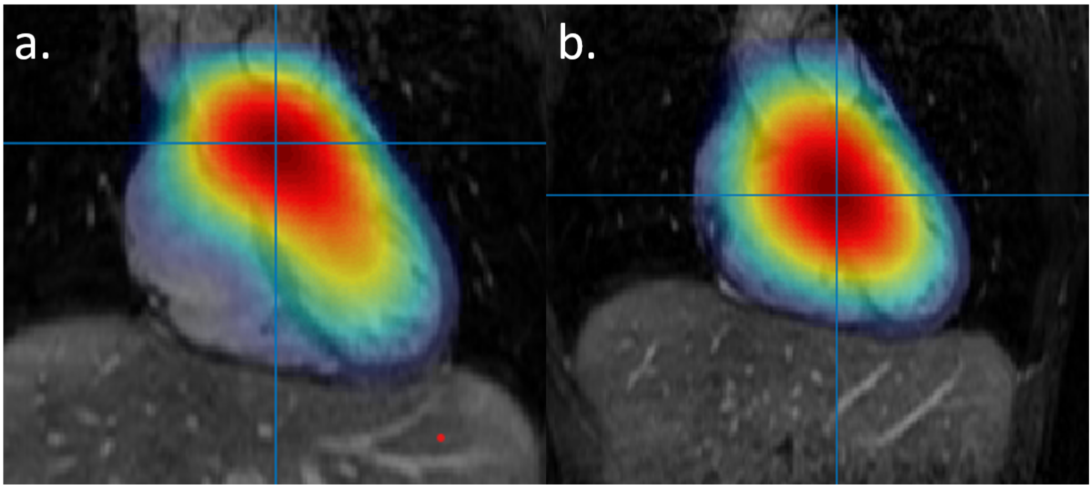

Figure 4.10: The heart activity results depicted over the relevant MRI layer a. represents the LORETA inverse localization for using the MCG array at the back side, with a Euclidean distance from the simulated source activity of 37.775 mm. b. represents the LORETA inverse localization for using two MCG arrays at the right and left sides, with a Euclidean distance from the simulated source activity of 7.874 mm.

4.3.4 Discussion

In this section, we discuss the factors that affect the MCG detection results and interpret the findings from the analyses. We identified three main factors that impact the accuracy of MCG localisation: the distance between the sensors and the source space, the orientation alignment between the sensors and the simulated signal, and the number of sensors.

Our results showed that the euclidean distance for using the back side array was the highest, indicating that the heart is closer to the front side of the torso than the back side. The distances using the four sides and three sides arrays were similar to the default setup with frontal array, suggesting that they can be viable alternatives. However, the use of many sensors with 189 and 252 did not improve the results. This is likely because they include the back side array, which did not provide good localisation results. Furthermore, we already have a sufficient number of sensors in one array (63 sensors), making the 189 and 252 setups excessive.

Interestingly, the right-left sides setup had the best results with an euclidean distance of 7.874 mm. We believe that this is because the MCG arrays were better aligned with the simulated signal. As we explained in the second section of this chapter (4.2.2), the simulated data had a low value at the x-axis orientation (right-left axis as shown in figure (4.8)), with most of the activity in the y and z axes. This means that the electrical field could be best detected using sensors in the front and back sides, and theoretically also the top and bottom. However, according to Maxwell's equations, the magnetic field is perpendicular to the electrical field, meaning that the detection of the magnetic field is better using sensors at the right and left sides. This explains why we obtained better results using the right-left array.

In real MCG data localisation, the orientation of the source activity could be uncertain, which would affect the accuracy of the localisation results. However, the findings from this study provide valuable insights into the factors that influence MCG localisation and can help researchers optimize their MCG data acquisition and processing strategies to improve the accuracy of localisation.

Chapter 5

MCG Data and Analyses

In chapter (4), we tested our pipeline with simulated data by evaluating it with various inverse problem methods, different source activity scenarios, and noise levels. In this chapter, we apply our pipeline to real MCG datasets to locate current densities in the heart.

We utilized two inverse problem methods: LORETA and STKF. We employed STKF with two models: AR1 and AR2, additionally we used the ssGARCH.

This chapter presents the application of our pipeline to real MCG data, demonstrating its effectiveness in localising current densities in the heart. Through our analysis with multiple inverse problem methods and models, we provide a comprehensive evaluation of our pipeline and its potential for use in clinical settings.

5.1 MCG Data

This chapter utilizes two datasets from previous studies or projects for our analysis.

5.1.1 Reference Dataset at BMSR-2

Our first dataset was obtained from a previous study and was intended as a reference dataset for further research involving forward modelling and inverse localization. The dataset has been published and shared online [Koc+11]. The measurement setup for this dataset is similar to the one we used in section (3.1.1) at BMSR-2, as shown in figure (3.2), with a 304-channel SQUID MCG system as depicted in figure (3.3). However, we used only 49 channels from the bottom layer of the SQUID device. We selected these channels because they are on the same layer level and have the same orientation towards the heart, which allows for better comparison with other sensor modalities, such as OPM and electrodes. Additionally, reducing the number of sensors to the nearest and most significant ones also reduces the time consumption for the STKF method.

The sampling rate for this dataset is 1 kHz, but we downsampled it to 250 Hz to reduce the computational power required for our STKF method. We also demeaned the data and chose a segment that shows two heartbeats, which has a window of 350 samples. This segment is depicted in figure (5.1) in butterfly plot form.

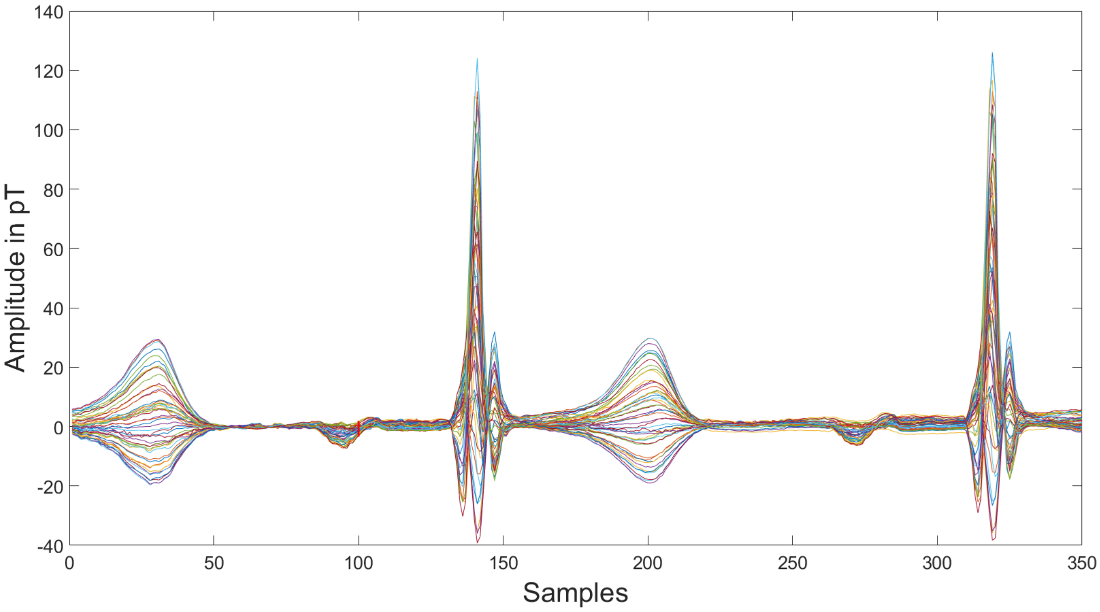

Figure 5.1: The butterfly plot of the segment of the first MCG dataset used in our inverse problem analysis. This dataset consists of 49 channels, with a sampling rate of 250 Hz, and contains two heartbeats plotted over 350 samples. The amplitude is in picotesla.

5.1.2 CS-MAG Dataset at the Hospital University of Charité

The second dataset used in this chapter was recorded during a previous project of Collaborative Research Centres (CRC) 855 [Ahr15]. The MCG SQUID system used for the measurement is CS-MAG from the company of Biomagnetik Park in Hamburg. The layout of the system has 64 channels, but only 63 channels were successfully recorded in this dataset. The sampling frequency is 500 Hz, and the dataset contains one heartbeat plotted over 400 samples, as shown in the butterfly plot in figure (5.2). The amplitude of the signal is measured in pico Tesla.

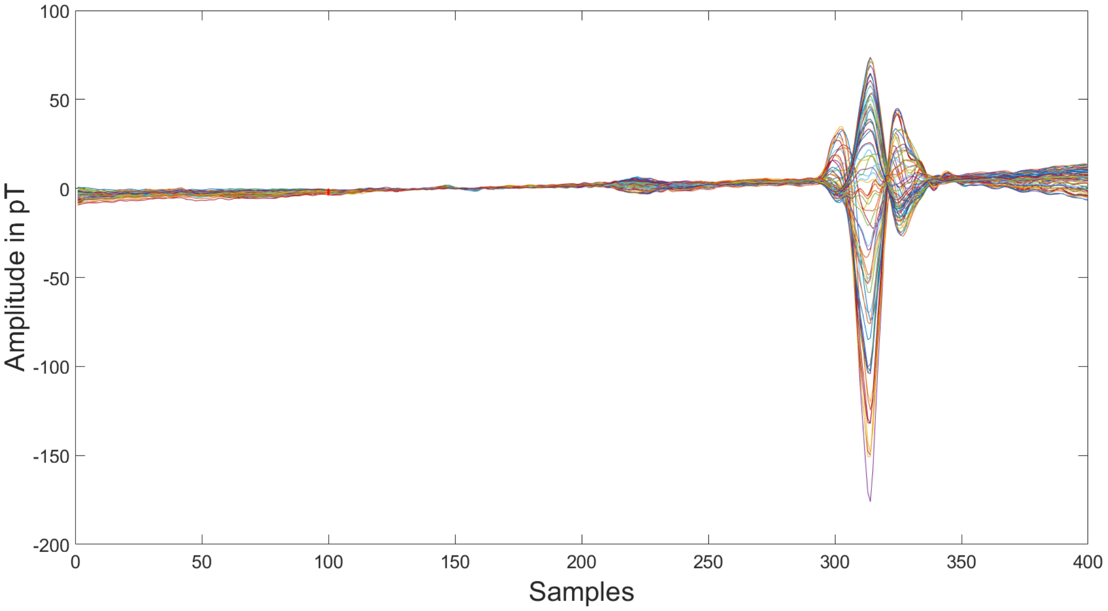

Figure 5.2: The second MCG data that we used to solve the inverse problem, the dataset 63 channels that were plotted in the butterfly form. The dataset contains one heartbeat plotted over 400 samples. The amplitude is in pico Tesla

.

5.2 Torso-heart Model

Both datasets used in this chapter required a torso-heart model for inverse localization of the current densities in the heart. For the first dataset, we had MRI recordings available for the same individual as the MCG and ECG measurements. However, the second dataset had no MRI recordings available. Therefore, we used the same torso-heart model for both datasets by aligning the sensor locations of the second dataset to the model and used it as a standard for both datasets.

As explained in (3.2.2), the torso-heart model has two layers. The first layer represents the heart, and the second layer represents the rest of the torso or the torso boundaries. The model used in this study is shown in figure (3.13) in chapter (3).

In order to show the source activity on the MRI, we show three planes of the torso. The first plane is the coronal, this plane divides the body into front (anterior) and back (posterior) sections. The second plane is the sagittal, this plane divides the body into left and right sections. The third plane is the axial, this plane divides the body into top (superior) and bottom (inferior) sections as shown in the figure (5.3). The result are always shown on the cross section slides where the maximum activity is localised. [Gin+11]

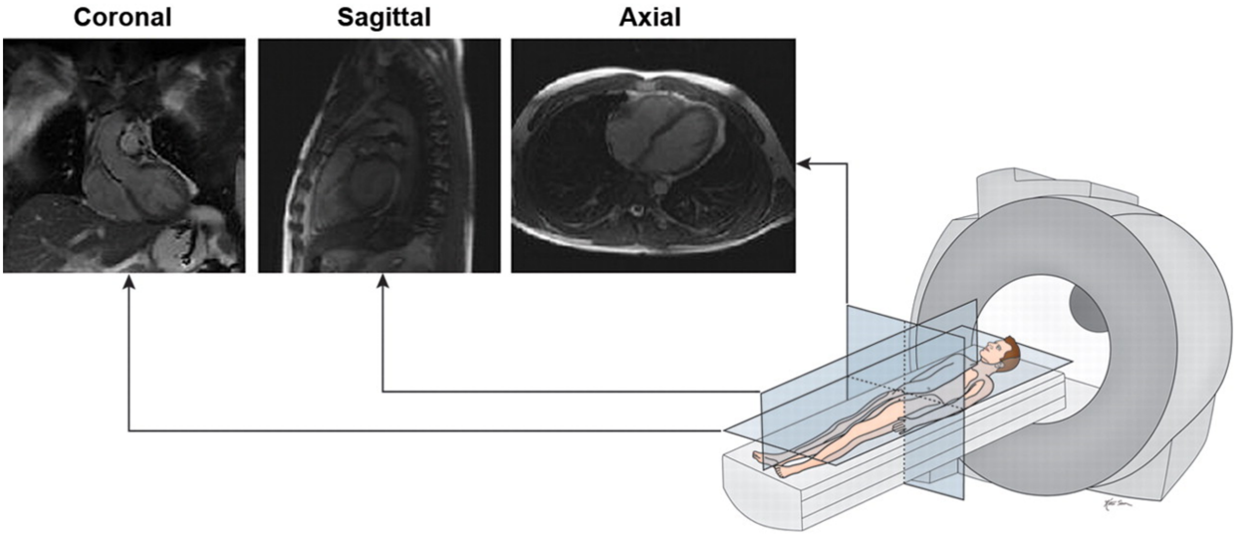

Figure 5.3: A diagram illustrates the position of the main anatomical planes in relation to the subject and how they appear in on MRI. [Gin+11]

5.3 Analysis

We employed two inverse problem methods, namely the Spatiotemporal Kalman Filter (STKF) and the Low-Resolution Electromagnetic Tomography (LORETA), to localise the sources. We used STKF because it is our implemented inverse problem method and we are continuously working towards developing and improving it further. We used LORETA because it is a well-established method that is similar to STKF in terms of spatial smoothness. The primary difference between LORETA and STKF is the inclusion of temporal smoothness in STKF. We aimed to investigate how the inclusion of temporal smoothness improved source localisation.

To compare the results from the two datasets and two different Laplacian implementations, we performed multiple analyses using both inverse problem methods. We visualized the source localisation results on the MRI recording at two different time points of the PQRST complex: the P-point and the R-point. We chose these two points because they generate source activities at different locations in the heart. Furthermore, the signal at the P- and R-point has different amplitudes, making it more challenging to detect the P wave since the R wave is relatively stronger. This approach allowed us to investigate which amplitudes each method can localise effectively.

The orientations of the MRI results are intuitive, given that the heart is consistently positioned on the left and anterior aspects of the torso. In both the coronal and sagittal views, the superior part of the image corresponds to the superior part of the body, and likewise for the inferior part. In the coronal view, the right side of the image corresponds to the left side of the body, and vice versa. In the sagittal view, the anterior part of the body is depicted on the left side of the image, while the posterior part is on the right. In axial views, the posterior aspect of the body is shown at the top of the image, while the anterior aspect is at the bottom.

As explained in section (2.2) and figure (2.3), the heartbeat cycle starts at the Sinoatrial (SA) node, which is at the top right part of the heart, then it moves downwards to the Atrioventricular (AV) node to activate the upper part of the heart. This activity in the upper part of the heart is related to the generation of the P-wave.

Then the activity moves downwards to the bottom of the heart to activate the Purkinje fibres and eventually contracting the right and left ventricles. This activity is stronger and related to the R-point as shown in figure (2.4).

In conclusion, we expect to find the correct source activity on the upper right side at the P-point and on the bottom of the heart at the R-point as shown in figure (2.4).

5.3.1 Demeaning

Unlike ECG data, raw MCG data does not have a common reference channel, and the baseline of each channel can trend differently over time at different levels. This means that the trend for MCG data is meaningless, and running inverse problems without proper demeaning results in unclear results. This is because the baseline level is more significant than the changes in the MCG data.

To address this issue, we must demean the MCG channels before running the inverse problem. We can achieve this by finding the mean of every MCG channel over a relatively silent time segment between the T-point and the P-point of the next heartbeat, where the heart activity is very low. It is safe to assume that there is no heart activity during this period, so the MCG channels can be demeaned back to the baseline. This approach is sufficient for our analyses, as we only use one or two heartbeats for each analysis.

5.3.2 Solving the Inverse Problem Using LORETA and STKF

In this section, we present the successful localisation results obtained using LORETA and STKF methods for the P- and R-points. We used both datasets for the analyses. As described in chapter (2), section (2.2), the source activities for the healthy heart should be in the middle-upper part of the heart at the P-point and in the bottom of the heart at the R-point. However, due to the complexity of the inverse problem and the lack of a common reference channel in MCG data, the localisation of the sources is challenging. To overcome this challenge, we used the laplacian matrix to define the spatial smoothness relation for the voxels in the source space. We also used the autoregressive model of the first order (AR1) to describe the dynamical model for the STKF.

The results for the first dataset are shown in figure (5.4). The LORETA method detected two sources at the P-point, with one of them located at the bottom part of the heart, which is irrelevant to the activity at the P-point. The second source, located at the upper side of the heart, is more relevant, as shown in figure (5.4 a.). However, the LORETA results at the R-point showed that there was one source at the left ventricle, but it was still not correct as it was more in the middle elevation in the heart than at the bottom, as shown in figure (5.4 b.)

The STKF results at the P-point showed multiple source activities, with the strongest source at the middle but shifted to the left side, closer to the mitral valve, as shown in figure (5.4 c.) The STKF results at the R-point also showed multiple sources, closer to the left ventricle as LORETA but still not correct, as shown in figure (5.4 d.)

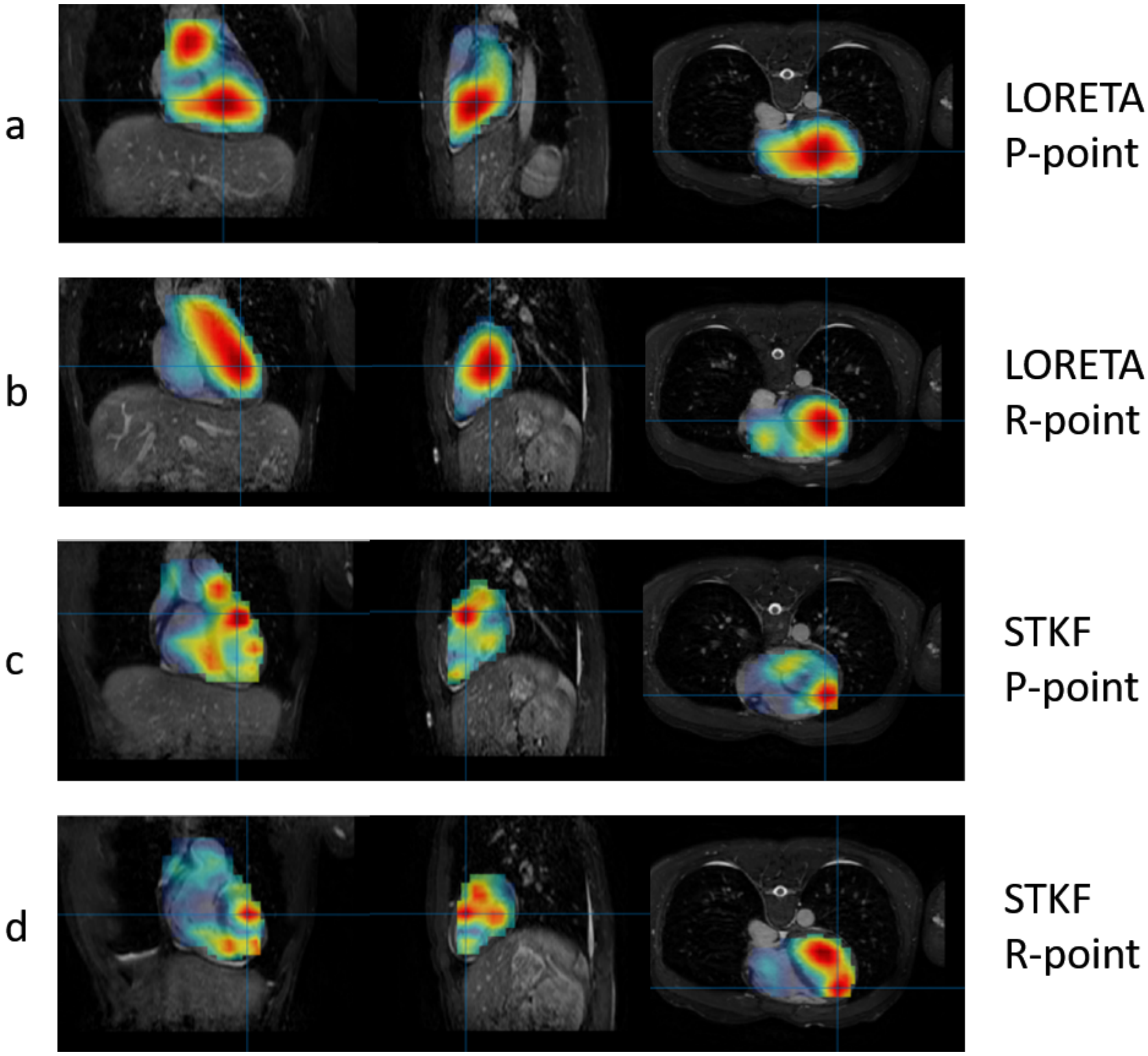

Figure 5.4: The source imaging results from the first dataset using LORETA and STKF at two times points of interest on the heartbeat cycle, namely the P-point and the R-point. The source activity results are superimposed on the MRI to show the heart activity in accordance with the heart anatomy.

The results for the second dataset are shown in figure (5.5). In general, the localisations for this MCG dataset were better. The localisation using LORETA was correct for both the P- and R-points, as shown in figures (5.5 a.) and (5.5 b.), respectively. The localisation using the STKF was correct for the R-point, as shown in figure (5.5 d.), but deviated toward the left ventricle for the P-point, as shown in figure (5.5 c.). The P-point is harder to detect because its signal is weaker, and this is where the STKF starts to struggle.

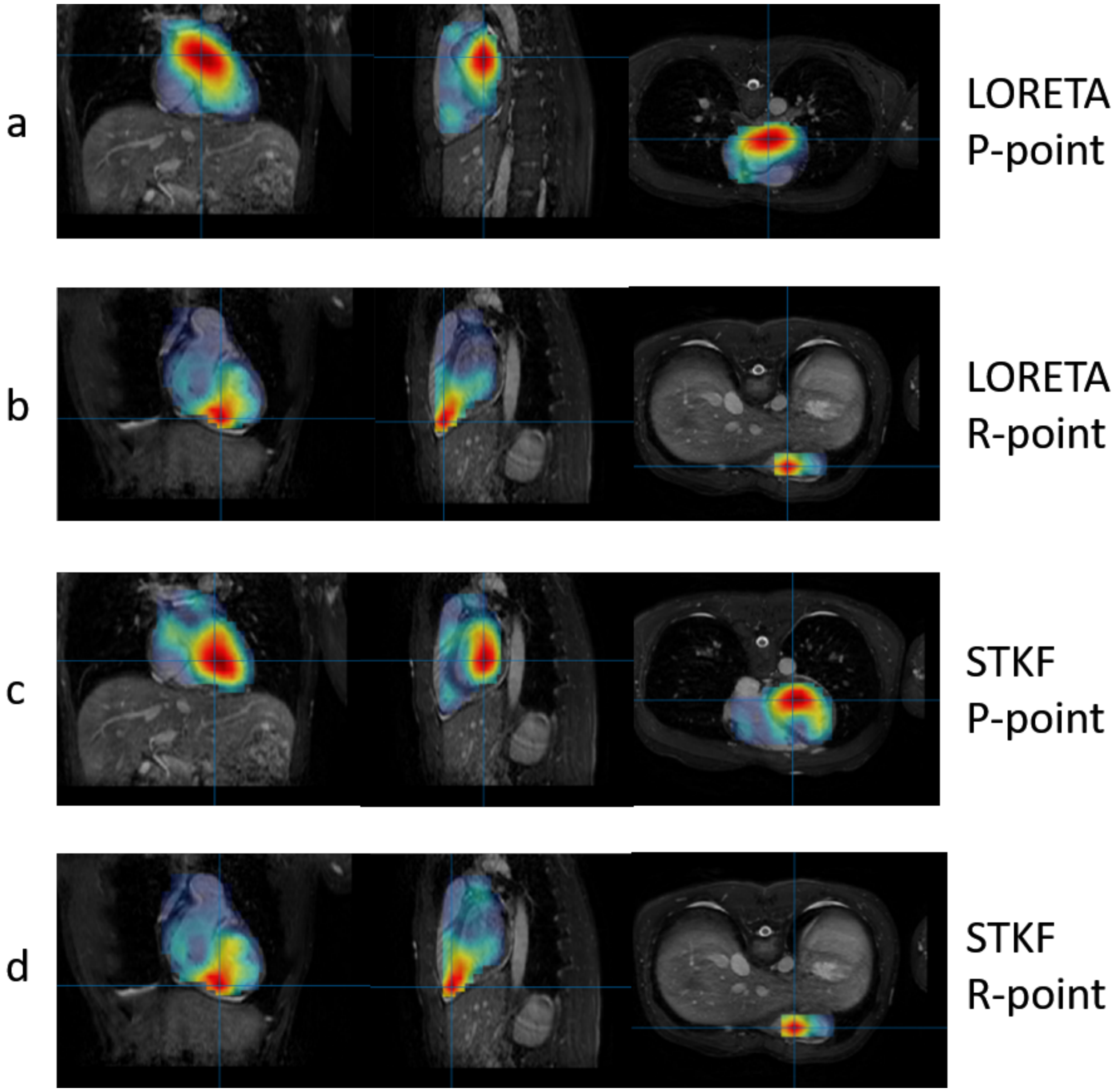

Figure 5.5: The source imaging results from the second dataset using LORETA and STKF at two time points of interest on the heartbeat cycle, namely the P-point and the R-point. The source activity results are superimposed on the MRI to show the heart activity in accordance with the heart anatomy.

5.3.3 New Laplacian Matrix

Both LORETA and STKF methods rely on spatial smoothness, and the Laplacian matrix determines how the source activities of voxels are related to each other and averaged. In the previous definition, voxel activities were averaged with their six neighbour voxels - two neighbours on each coordinate axis. However, in the new definition, we considered the actual number of neighbours, so voxels on the surface or edge of the heart, for example, have fewer than six neighbours.

We repeated the calculation of LORETA and STKF with the new definition for the second MCG dataset and show the results in figure (5.6). The source imaging results from LORETA look almost the same as the results from the old Laplacian definition shown in figure (5.5). However, for the STKF method, the localization shows a significant improvement at the P-point. The source activity appears at two points, one of them close to the sinoatrial node and the second one close to the atrioventricular node, as shown in figure (5.6 c.) This description actually reflects the activity of those two points in the first half of the heart cycle and shows the transition of activity from the sinoatrial node to the atrioventricular node.

Figure (5.6) shows the source imaging results from the second dataset using LORETA and STKF with the new Laplacian matrix definition at two time points of interest on the heartbeat cycle, namely the P-point and the R-point. The source activity results are superimposed on the MRI to show the heart activity in accordance with the heart anatomy.

5.3.4 State-space Generalized Autoregressive Conditional Heteroskedasticity Spatiotemporal Kalman Filter (ssGARCH-STKF)

In the STKF method, the dynamical noise variance parameter has a significant influence on the results. To further improve the model, we introduce a state-space GARCH model denoted as ssGARCH. The focus of this development is on the dynamical noise variance parameter, which has a single value across different source locations and time points in the STKF method. However, with the ssGARCH model, the dynamical noise variance parameter changes with source locations and time points. This marks the first time a ssGARCH model with the STKF has been used to solve the inverse problem for heart MCG dataset.

For our experiment, we used the dataset measured by the Collaborative Research Centres (CRC) 855, as described in section (5.1.2) [Ahr15]. We used a 400 time point data segment for the whole 63 MCG channels, which includes one heartbeat. The data was demeaned as described in section (5.3.1). We used the torso model that we built from the MRI provided by the first dataset, explained in section (5.1.1) [Koc+11], and aligned the MCG sensors on it.

To compare the performance of LORETA, STKF, and ssGARCH-STKF, we analysed a data segment using the AR1 model with initial values of $a = 0.915$, a dynamical noise covariance of -7, and an observation noise initial value of -10. The initial parameters of the ssGARCH model are set to -0.0002 for β and 0.5 for γ.

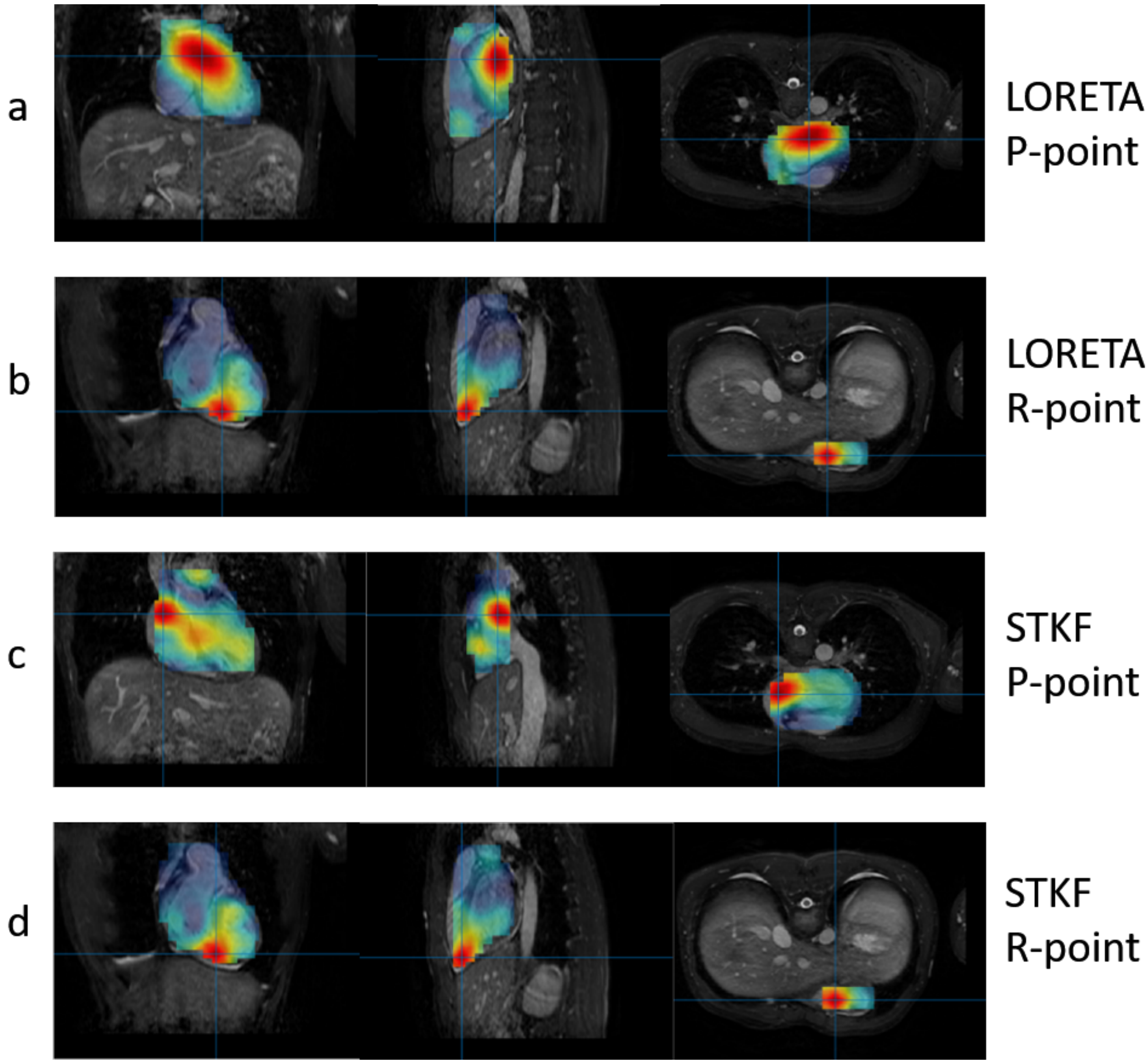

Figure 5.6: The source imaging results from the second dataset using LORETA and STKF and new definition for the laplacian matrix at two time points of interest on the heartbeat cycle, namely the P-point and the R-point. The source activity results are superimposed on the MRI to show the heart activity in accordance with the heart anatomy.

We then optimised these values using three optimisation methods: the Broyden-Fletcher-Goldfarb-Shanno (BFGS) method, the simplex algorithm, and a simplistic stochastic optimisation method. We used these three methods to avoid getting stuck in a local minimum, as described in section (2.9.5).

The optimized parameters, in comparison with their initial values, are presented in Table 5.1. As previously mentioned, the Akaike Information Criterion (AIC) serves as a measure of how well the model fits the data. A lower AIC value indicates a better fit of the model to the data.

Both the STKF and ssGARCH-STKF utilized the same number of optimisation processes, and the total time taken to complete these processes was roughly equivalent. However, STKF achieved its final AIC value significantly faster. In contrast, ssGARCH-STKF required five times as much time to reach its final AIC value.

Parameters	**Initials**	**Optimised STKF**	**Optimised ssGARCH-STKF**
AIC	N/A	-32066	-34347
a	0.915	0.9693	0.9694
Dynamical noise covariance	-7	-4.9179	-5.6853
GARCH β parameter	-0.0002	N/A	0.4555
GARCH γ parameter	0.5	N/A	2.6335
Observation noise variance	-10	-6.3239	-6.4428

Table 5.1: Initial parameters in comparison with the optimised parameters using STKF and ssGARCH-STKF methods.

The results are depicted in Figures (5.7) for the P-point of the PQRST-complex and (5.8) for the R-point. For the P-point, the STKF and ssGARCH-STKF results are notably similar, both exhibiting increased activity movement. However, LORETA demonstrates a more precise detection of the activity's location. In the case of the R-point, all three methods successfully detect the correct location. Yet, the results from ssGARCH-STKF are more focal.

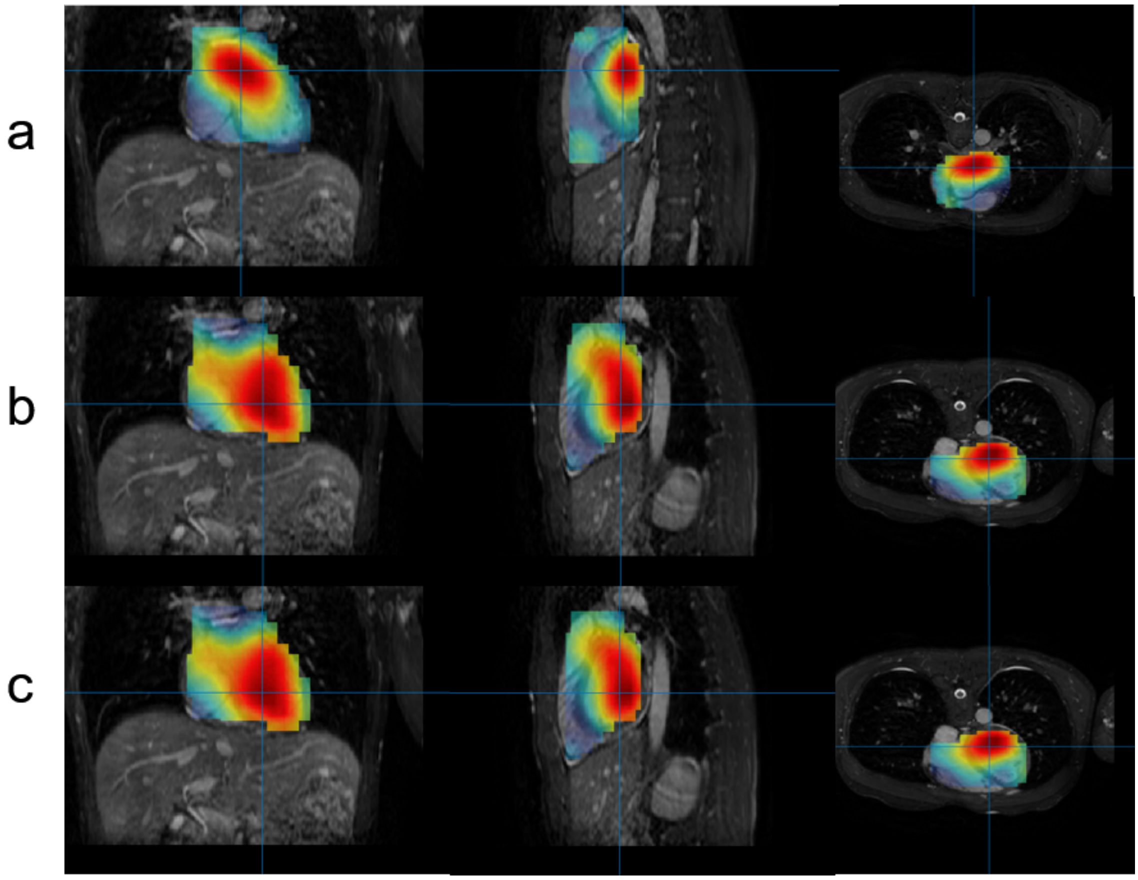

Figure 5.7: The source imaging results from the second dataset using LORETA, STKF, and ssGARCH-STKF. a. LORETA, b. STKF, and c. ssGARCH-STKF. The source activity results are superimposed on the MRI to show the heart activity at he P-point in accordance with the heart anatomy.

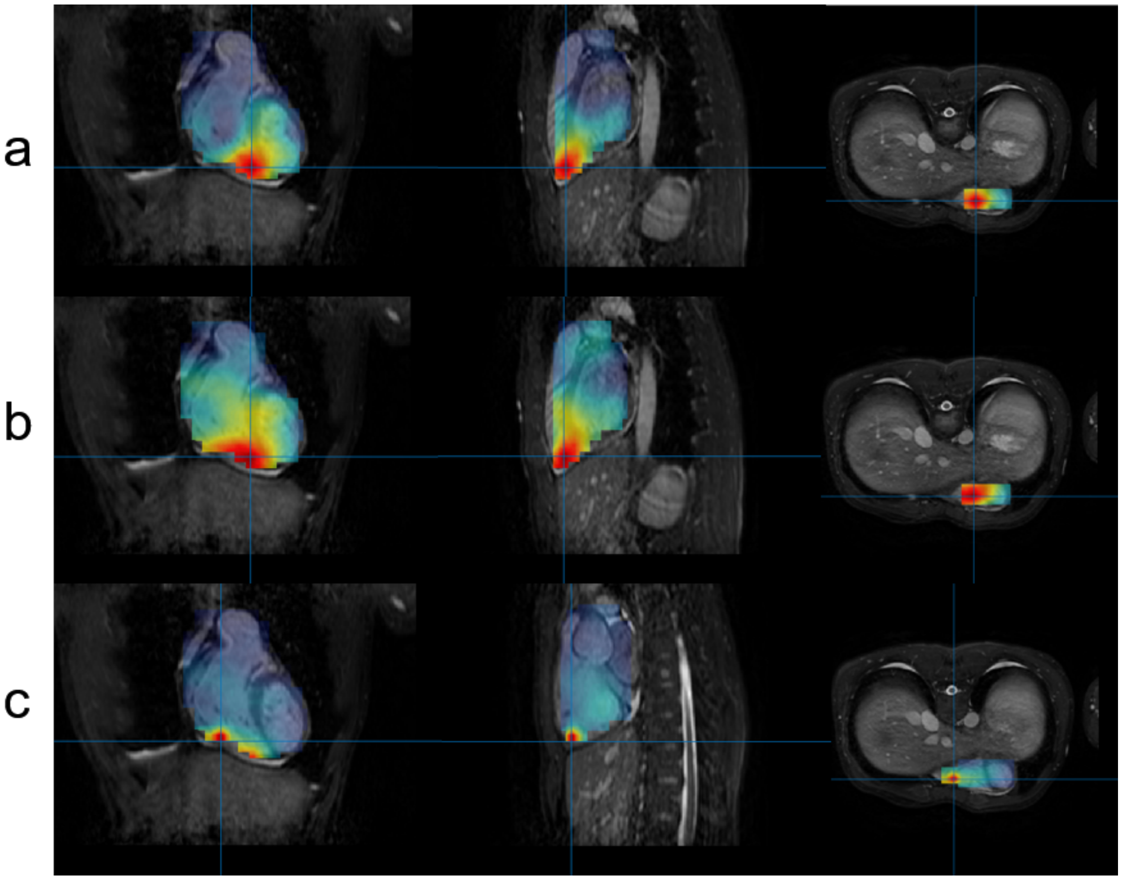

Figure 5.8: The source imaging results from the second dataset using LORETA, STKF, and ssGARCH-STKF. a. LORETA, b. STKF, and c. ssGARCH-STKF. The source activity results are superimposed on the MRI to show the heart activity at he R-point in accordance with the heart anatomy.

5.4 Discussion

In this chapter, we applied our pipeline using individual MCG datasets. Compared to other sensor modalities such as Magnetoencephalography (MEG) for the brain, MCG datasets require less preprocessing since the heart's magnetic field is much stronger than the interference from muscles and eye movement. However, since it does not have a common channel called reference like the ECG, it needs to be demeaned to have all channels on the same baseline.

The source imaging results for the first MCG dataset showed that the sources are deviated from the expected locations, but for the second dataset, the results were closer to the truth, especially for LORETA at P- and R-points. However, for STKF, only the analysis at the R-point was correct. Nevertheless, the results showed an improvement for the STKF as we redefined the Laplacian matrix.

While the LORETA results were similar to the old Laplacian definition, the STKF method showed improved localization at the P-point. The source activity was observed at two points, one near the sinoatrial point and the other near the atrioventricular node, and the transition of activity between these two points in the first half of the heart cycle was seen as an improvement to the results.

The ssGARCH-STKF algorithm yields slightly superior results compared to the STKF method. However, it requires significantly more time for optimisation. As suggested by the results, this increase in time is partially due to the additional calculations mentioned in Subsection 2.9.7. Interestingly, one optimisation process takes approximately the same amount of time as when using STKF. The increased time consumption is primarily attributed to the heightened model complexity, which necessitates more optimisation processes for parameter optimisation.

In conclusion, our pipeline, which employs both STKF and ssGARCH-STKF methods for source imaging of MCG datasets, demonstrates encouraging outcomes. However, a comprehensive assessment of the differences between these two methods needs further investigation. This includes evaluating their performance on a more extensive dataset and comparing them with other existing methods. Future research should also explore potential enhancements, such as the integration of anatomical information and the application of deep learning techniques.

Chapter 6

Conclusion and Outlook

In this thesis, we propose a novel pipeline for source imaging of the heart's magnetic field. The pipeline combines various preprocessing techniques and different inverse methods to achieve accurate localisation of the heart's electrical activity. To validate the pipeline's effectiveness, we conducted three studies using simulated datasets and two real MCG datasets, comparing the results obtained from different inverse methods, including MNE, LORETA, STKF, and ssGARCH-STKF.

The objective of this work is not only to provide initial results but also to construct a pipeline that transforms the neurological and engineering knowledge and expertise that we obtain through the years from the brain research into the heart research to open the door for future heart data analysis.

In chapter (3), we discuss the pipeline's basic processes and setup, including data collection, preprocessing, segmentation, heart-torso modelling, and solving the forward problem. We also explain the limitations of the pipeline in terms of segmentation and obtaining high-quality MRI suitable for 3D segmentation for multiple regions of the torso. For future MRI recordings, we need experts to set up the scanner parameters optimally to achieve satisfying results within the shortest possible time for the volunteers inside the MRI tube.

Chapter (4) investigates the performance of three methods for MCG source imaging: MNE, LORETA, and STKF. The results show that both MNE and LORETA are effective in medium to high SNR scenarios, but STKF outperforms LORETA in low SNR scenarios. This finding is likely due to the STKF method's consideration of both temporal and spatial smoothness. We also identify three factors that impact MCG localisation accuracy: distance between sensors and source space, orientation alignment between sensors and simulated signal, and number of sensors. Our results suggest that the right-left sides setup is the most effective due to the alignment of the MCG arrays with the simulated signal.

In chapter (5), we showcase the pipeline's application to real MCG data, effectively localising current densities in the heart. Our evaluation, utilising multiple inverse problem methods and models, highlights the pipeline's potential suitability for clinical use. The STKF method outperforms the other methods in terms of localisation accuracy, particularly at the P-point. The LORETA method still shows promising results, but the STKF method is more accurate and precise in localising the sources. The ssGARCH-STKF method did not significantly outperform the STKF method, but it offers the advantage of allowing the dynamical noise variance parameter to vary with source locations and time points, which could be useful for analysing larger datasets.

Overall, these findings have implications for researchers designing MCG studies. They highlight the importance of carefully considering the specific requirements of their study when selecting a method for MCG source imaging and optimising MCG data acquisition and processing strategies to improve the accuracy of localisation. The limitations of the study, including the MRI segmentation, should also be taken into account when interpreting the results.

Future work includes improving the pipeline by incorporating more advanced preprocessing techniques, such as denoising and artifact removal, and optimising the parameters for each method to improve their performance. The ssGARCH-STKF method could also be tested on a larger number of datasets to fully assess its potential benefits. Additionally, our pipeline could be extended to analyse other types of cardiac data, such as electrocardiography (ECG) and a combination of simultaneously recorded MCG and ECG dataset. We have already implemented a fusion inverse problem method for different sensors modalities in previous studies. [Ham+13; Hab14].

In conclusion, this thesis presents a promising pipeline for source imaging of the heart's magnetic field using different inverse methods, and our results demonstrate the potential for accurately localising sources using the Kalman filter method. This pipeline could be further improved and extended to analyse other types of cardiac data, contributing to a better understanding of cardiac activity and underlying mechanisms. As future work, we suggest improving the MRI recording quality and developing an automated segmentation software for the heart using machine learning algorithms to make the segmentation process less manual and tedious.

Bibliography

References

[AHEHS18] Laurent Ros Ali Houssam El Husseini and Eric Pierre Simon. “Expression for the radius r of an AR (2) process used to model a wireless communication channel”. In: (2018) (cit. on p. 67).

[Ahr15] Henning Ahrens. “Activation time imaging with the Extended Kalman Filter and the Unscented Kalman Filter”. PhD thesis. 2015 (cit. on pp. 43, 45, 54, 62, 64, 69, 76, 82).

[BF+12] F. Buendía-Fuentes, M. A. Arnau-Vives, A. Arnau-Vives, Y. Jiménez-Jiménez, J. Rueda-Soriano, E. Zorio-Grima, A. Osa-Sáez, L. V. Martínez-Dolz, L. Almenar-Bonet, and M. A. Palencia-Pérez. “High-Bandpass Filters in Electrocardiography: Source of Error in the Interpretation of the ST Segment”. In: *ISRN Cardiology* 2012 (June 2012), pp. 1–10 (cit. on p. 19).

[BG97] S. Baillet and L. Garnero. “A Bayesian approach to introducing anatomo-functional priors in the EEG/MEG inverse problem”. In: *IEEE Transactions on Biomedical Engineering* 44.5 (May 1997), pp. 374–385 (cit. on p. 22).

[Bio] *Biomagnetik Park GmbH.* `https://biomagnetik.com/` (cit. on pp. 43, 45).

[CIB16] CIBC. Seg3D: Volumetric Image Segmentation and Visualization. Scientific Computing and Imaging Institute (SCI), Download from: http://www.seg3d.org. 2016 (cit. on pp. 50, 54).

[Ecg] *ECGSIM.* https://www.ecgsim.org/downloads/other13/downloadgeo.php. 2014 (cit. on p. 45).

[Eng82] Robert F. Engle. “Autoregressive Conditional Heteroscedasticity with Estimates of the Variance of United Kingdom Inflation”. In: *Econometrica* 50.4 (July 1982), p. 987 (cit. on p. 35).

[Fie] *FieldTrip/SimBio toolbox.* www.fieldtriptoolbox.org/development/project/simbio_plan. 2021 (cit. on p. 56).

[Gal+04] Andreas Galka, Okito Yamashita, Tohru Ozaki, Rolando Biscay, and Pedro Valdés-Sosa. “A solution to the dynamical inverse problem of EEG generation using spatiotemporal Kalman filtering”. In: *NeuroImage* 23.2 (Oct. 2004), pp. 435–453 (cit. on pp. 5, 23–26, 28, 32, 33).

[Gal+08] Andreas Galka, Tohru Ozaki, Hiltrud Muhle, Ulrich Stephani, and Michael Siniatchkin. “A data-driven model of the generation of human EEG based on a spatially distributed stochastic wave equation”. In: *Cognitive Neurodynamics* 2.2 (Apr. 2008), pp. 101–113 (cit. on pp. 33, 34).

[Gan+16] Prasanth Ganesan, Mark Sterling, Steven Ladavich, and Behnaz Ghoraani. "Computer-Aided Clinical Decision Support Systems for Atrial Fibrillation". In: *Computer-aided Technologies - Applications in Engineering and Medicine*. InTech, Dec. 2016 (cit. on p. 14).

[Gin+11] Daniel T. Ginat, Michael W. Fong, David J. Tuttle, Susan K. Hobbs, and Rajashree C. Vyas. "Cardiac Imaging: Part 1, MR Pulse Sequences, Imaging Planes, and Basic Anatomy". In: *American Journal of Roentgenology* 197.4 (Oct. 2011), pp. 808–815 (cit. on pp. 77, 78).

[Gre+08] Roberta Grech, Tracey Cassar, Joseph Muscat, Kenneth P Camilleri, Simon G Fabri, Michalis Zervakis, Petros Xanthopoulos, Vangelis Sakkalis, and Bart Vanrumste. "Review on solving the inverse problem in EEG source analysis". In: *Journal of NeuroEngineering and Rehabilitation* 5.1 (2008), p. 25 (cit. on p. 5).

[Gri99] D.J. Griffiths. *Introduction to Electrodynamics*. Prentice Hall, 1999 (cit. on p. 20).

[GYO04] Andreas Galka, Okito Yamashita, and Tohru Ozaki. "GARCH modelling of covariance in dynamical estimation of inverse solutions". In: *Physics Letters A* 333.3-4 (Dec. 2004), pp. 261–268 (cit. on pp. 5, 22, 25, 35, 36).

[Hab14] Nawar Habboush. "MEG-EEG Fusion Using Spatiotemporal Kalman Filtering with an Emphasis on the Correct Localization of Deep Brain Sources." MA thesis. Department of Digital Signal Processing and System Theory, Christian-Albrechts-University of Kiel, 2014 (cit. on pp. 23, 28, 67, 90).

[Hab+18] Nawar Habboush, Laith Hamid, Michael Siniatchkin, Ulrich Stephani, and Andreas Galka. "Pipeline for Forward Modeling and Source Imaging of Magnetocardiographic Recordings via Spatiotemporal Kalman Filtering". In: *2018 40th Annual International Conference of the IEEE Engineering in Medicine and Biology Society (EMBC)*. IEEE, July 2018 (cit. on p. 61).

[Ham+13] Laith Hamid, Umit Aydin, Carsten Wolters, Ulrich Stephani, Michael Siniatchkin, and Andreas Galka. "MEG-EEG fusion by Kalman filtering within a source analysis framework". In: *2013 35th Annual International Conference of the IEEE Engineering in Medicine and Biology Society (EMBC)*. IEEE, July 2013 (cit. on p. 90).

[Ham18] Laith Hamid. "M/EEG Source Imaging via the Spatiotemporal Kalman Filter and its Applications in Epileptology". PhD thesis. Department of Digital Signal Processing and System Theory, Christian-Albrechts-University of Kiel, 2018 (cit. on pp. 23, 28).

[HI94] M. S. Hämäläinen and R. J. Ilmoniemi. "Interpreting magnetic fields of the brain: minimum norm estimates". In: *Medical & Biological Engineering & Computing* 32.1 (Jan. 1994), pp. 35–42 (cit. on p. 24).

[HKS10] Peter Hansen, Morten Kringelbach, and Riitta Salmelin, eds. *MEG: An Introduction to Methods*. Oxford University Press, June 2010 (cit. on p. 24).

[IMZ12] Ziad F. Issa, John M. Miller, and Douglas P. Zipes. “Ablation Energy Sources”. In: *Clinical Arrhythmology and Electrophysiology: A Companion to Braunwald's Heart Disease*. Elsevier, 2012, pp. 144–163 (cit. on p. 3).

[Kel+10] David U J Keller, Frank M Weber, Gunnar Seemann, and Olaf Dössel. “Ranking the Influence of Tissue Conductivities on Forward-Calculated ECGs”. In: *IEEE Transactions on Biomedical Engineering* 57.7 (July 2010), pp. 1568–1576 (cit. on pp. 50, 54).

[Koc+11] Hans Koch, Ralf-Dieter Bousseljot, Olaf Kosch, Cosima Jahnke, Ingo Paetsch, Eckart Fleck, and Bernhard Schnackenburg. “A reference dataset for verifying numerical electrophysiological heart models”. In: *BioMedical Engineering OnLine* 10.1 (2011), p. 11 (cit. on pp. 43, 50, 51, 75, 82).

[Li+16] Xiangrui Li, Paul S. Morgan, John Ashburner, Jolinda Smith, and Christopher Rorden. “The first step for neuroimaging data analysis: DICOM to NIfTI conversion”. In: *Journal of Neuroscience Methods* 264 (May 2016), pp. 47–56 (cit. on p. 54).

[Luo+18] Yuan Luo, Parinaz Abiri, Shell Zhang, Chih-Chiang Chang, Amir H. Kaboodrangi, Rongsong Li, Alex Bui, Rajesh Kumar, Mary Woo, Zhaoping Li, René R. Sevag Packard, Yu-Chong Tai, and Tzung K. Hsiai. “Non-Invasive Electrical Impedance Tomography for Multi-Scale Detection of Liver Fat Content”. In: *Theranostics* 8.6 (2018), pp. 1636–1647 (cit. on p. 54).

[MMH12] Claire A Martin, Gareth D K Matthews, and Christopher L-H Huang. “Sudden cardiac death and inherited channelopathy: the basic electrophysiology of the myocyte and myocardium in ion channel disease”. In: *Heart* 98.7 (Mar. 2012), pp. 536–543 (cit. on p. 3).

[MP95] Jaakko Malmivuo and Robert Plonsey. *Bioelectromagnetism: Principles and Applications of Bioelectric and Biomagnetic Fields*. Oxford University Press, Oct. 1995 (cit. on pp. 12, 13, 15, 63).

[PM95] R. Pascual-Marqui. “Reply to comments by Hämäläinen, Ilmoniemi and Nunez”. In: *ISBET Newsletter* 6 (1995), 22–24 (cit. on pp. 24, 34, 35).

[PM99] Roberto D. Pascual-Marqui. “Review of methods for solving the EEG inverse problem”. In: *International journal of bioelectromagnetism, vol. 1, no. 1, pp. 75–86* (1999) (cit. on pp. 24, 34).

[PMML94] R.D. Pascual-Marqui, C.M. Michel, and D. Lehmann. “Low resolution electromagnetic tomography: a new method for localizing electrical activity in the brain”. In: *International Journal of Psychophysiology* 18.1 (Oct. 1994), pp. 49–65 (cit. on pp. 24, 34).

[Sch+02] U Schmitt, A K Louis, C Wolters, and M Vauhkonen. “Efficient algorithms for the regularization of dynamic inverse problems: II. Applications”. In: *Inverse Problems* 18.3 (2002), pp. 659–676 (cit. on p. 22).

[Sim21] SimBio Development Group. *SimBio: A generic environment for bio-numerical simulations*. online, https://www.mrt.uni-jena.de/simbio. 2021 (cit. on p. 56).

[Sov+14] Siniša Sovilj, Ratko Magjarević, Amr Al Abed, Nigel H. Lovell, and Socrates Dokos. “Simplified 2D Bidomain Model of Whole Heart Electrical Activity and ECG Generation”. In: *Measurement Science Review* 14.3 (June 2014), pp. 136–143 (cit. on p. 54).

[Ste08] Philipp Stern. “Improved detection of deep neural activity from EEG measurements by the Kalman filter approach for inverse solutions”. diploma thesis. Institute of Theoretical Physics and Astrophysics, Christian-Albrechts-University of Kiel, 2008 (cit. on pp. 23, 28, 33, 67).

[VHA11a] K.L. Venkatachalam, Joel E. Herbrandson, and Samuel J. Asirvatham. “Signals and Signal Processing for the Electrophysiologist: Part I: Electrogram Acquisition”. In: *Circulation: Arrhythmia and Electrophysiology* 4.6 (Dec. 2011), pp. 965–973 (cit. on p. 19).

[VHA11b] K.L. Venkatachalam, Joel E. Herbrandson, and Samuel J. Asirvatham. “Signals and signal processing for the electrophysiologist: part II: signal processing and artifact”. In: *Circulation: Arrhythmia and Electrophysiology* 4.6 (Dec. 2011), pp. 974–981 (cit. on p. 19).

[Vor16] Johannes Vorwerk. “New Finite Element Methods to Solve the EEG/MEG Forward Problem”. PhD thesis. Mathematisch-Naturwissenschaftlichen Fakultät, Westfälischen Wilhelms-Universität Münster, 2016 (cit. on p. 56).

[Vor+18] Johannes Vorwerk, Robert Oostenveld, Maria Carla Piastra, Lilla Magyari, and Carsten H. Wolters. “The FieldTrip-SimBio pipeline for EEG forward solutions”. In: *BioMedical Engineering OnLine* 17.1 (Mar. 2018) (cit. on p. 54).

[Wik20] Wikipedia. *User:Wapcaplet — Wikipedia, The Free Encyclopedia.* `http://en.wikipedia.org/w/index.php?title=User%3AWapcaplet&oldid=535872862`. [Online; accessed 27-November-2020]. 2020 (cit. on p. 11).

[Won+06] Kin Foon Kevin Wong, Andreas Galka, Okito Yamashita, and Tohru Ozaki. “Modelling non-stationary variance in EEG time series by state space GARCH model”. In: *Computers in Biology and Medicine* 36.12 (Dec. 2006), pp. 1327–1335 (cit. on p. 5).

[Yam+04] Okito Yamashita, Andreas Galka, Tohru Ozaki, Rolando Biscay, and Pedro Valdes-Sosa. “Recursive penalized least squares solution for dynamical inverse problems of EEG generation”. In: *Human Brain Mapping* 21.4 (2004), pp. 221–235 (cit. on pp. 22, 24, 25).

[Yus+06] Paul A. Yushkevich, Joseph Piven, Heather Cody Hazlett, Rachel Gimpel Smith, Sean Ho, James C. Gee, and Guido Gerig. “User-Guided 3D Active Contour Segmentation of Anatomical Structures: Significantly Improved Efficiency and Reliability”. In: *Neuroimage* 31.3 (2006), pp. 1116–1128 (cit. on p. 50).

Erklärung

Hiermit erkläre ich, dass die vorliegende Dissertation nach Inhalt und Form meine eigene Arbeit ist und von mir selbst verfasst worden ist, wobei mir mein Doktorvater Herr Prof. Dr.-Ing. Gerhard Schmidt beratend zur Seite stand. Die Arbeit war weder in Teilen noch im Ganzen Bestandteil eines früheren Prüfungsverfahrens und ist an keiner anderen Stelle zur Prüfung eingereicht. Der Inhalt der Arbeit wurde in Teilen in meinen wissenschaftlichen Publikationen veröffentlicht. Dies ist in der Arbeit entsprechend vermerkt. Mir wurde kein akademischer Grad entzogen. Die Arbeit ist nach bestem Wissen und Gewissen konform mit den Regeln guter wissenschaftlicher Praxis, welche durch die Deutsche Forschungsgemeinschaft festgelegt sind.

Ort Datum Nawar Habboush